Department of Mechanical Engineering

Interactions of a Flexible Insert in Ideal Open and Channel Flows

Meagan Alison Burke

This thesis is presented for the degree of
Doctor of Philosophy
of
Curtin University

July 2015

Declaration

To the best of my knowledge and belief this thesis contains no material previously published by any other person except where due acknowledgement has been made. This thesis contains no material which has been accepted for the award of any other degree or diploma in any university.

All investigations presented in this thesis are my own except where specific reference has been made to the work of others. Some of the work presented in this thesis has been published in the following:

M. A. Burke, A. D. Lucey, N. S. J. Elliott, and R. M. Howell. Stability of a flexible wall separating two inviscid channel flows. *American Society of Mechanical Engineers. Pressure Vessels and Piping Conference, Paris, France.*, PVP2013-97373, 2013

M. A. Burke, A. D. Lucey, R. M. Howell, and N. S. J. Elliott. Stability of a flexible insert in one wall of an inviscid channel flow. *Journal of Fluids and Structures*, 48:435–450, 2014a

M. A. Burke, A. D. Lucey, R. M. Howell, and N. S. J. Elliott. *Fluid-Structure-Sound Interactions and Control. Proceedings of the 2nd Symposium on Fluid-Structure-Sound Interactions and Control.*, chapter Eigen-Analysis of an Inviscid Channel Flow with a Finite Flexible Plate in One Wall, pages 331–335. Lecture Notes in Mechanical Engineering. Springer, 2014b

M. A. Burke and A. D. Lucey. The nonlinear oscillations of a flexible surface comprising one wall of an inviscid channel flow. *3rd Symposium on Fluid-Structure-Sound Interactions and Control. Perth, Western Australia.*, 2015

Date: 07/07/2015

Acknowledgements

I would like to thank anyone who has had to listen to me talk about my research and who has supported me throughout the last few years, in particular:

Professor Tony Lucey for his ideas, support, patience, and for being a wonderful supervisor without whom this research would never have begun. Dr Christopher Davies for sparking my interest in fluid mechanics, and encouraging me to apply for this PhD. Dr Novak Elliott for his support and valuable help. Sucy Leong, for her caring nature and for never failing to be a friendly face.

My parents for... everything really. I cannot list all the things I am grateful to you for, but thank you. My sister for being there for me and for going to extraordinary lengths to do everything you can to help me through my undergrad and PhD. Her husband John for his eternal patience and for being the rock for my rock and to them both for putting up with me. My grandparents for being wonderful role models. For being proud of me and for being people that I want to make proud. A special thanks to my Granddad Bill.

Alicia, Caitriona and Sinead who have always been at my side as I journey through life for their never ending encouragement. Claire Day, for being a fantastic and selfless friend. Lee Walker for giving me a home away from home, helping me put things into perspective and teaching me the value of learning to relax.

All of my friends in Perth who have made living here incredible. In particular Alexandra who has been there for me without fail, supporting me through the bad times and for making the good times better. Finally I would like to thank Reilly, who has shared this experience with me. From the beginning when we had no idea what we were supposed to be doing, to the end when we were still guessing but would only admit it to each other, for sharing ideas, break-throughs, frustration, excitement and confusion with me.

Abstract

Methods to study the behaviour of a flexible insert comprising one wall of inviscid open and channel flows are developed. Improving the understanding of aero- and hydro-elastic systems such as those studied here, has applications in engineering and biomechanical systems. The aim here is to predict the conditions under which surface instabilities will occur, and assess the flow-induced plate behaviour of the flexible insert in both stable and unstable regimes.

The structural mechanics are modelled using a finite-difference method while the fluid mechanics are modelled using a boundary-element method. To study small deflections of the flexible insert, the structural and fluid mechanics are coupled using a state-space method whereby the eigenvalues and eigenvectors of the system are directly extracted. This allows the behaviour of a finite flexible insert with small deflections to be characterised, and an onset flow speed for surface instabilities to be predicted for given system parameters. An analytical equation to predict instability onset is also derived for an infinitely long channel with one rigid and one flexible wall.

An energy growth function is defined to consider the non-normality and transient growth of the system. Finally, full numerical simulations are performed to consider large deflections of a flexible insert. Attention is paid to the limit-cycle flutter type behaviour that occurs after instability onset. Results are compared with a theoretical equation.

The main findings are that; (i) reduction in channel width will cause flow-induced surface instabilities to occur at lower flow velocities, (ii) large-amplitude deflections may grow from small initial disturbances after linear-instability onset and before onset via transient growth, and (iii) the amplitude of instability induced surface oscillations increases as channel height decreases.

Contents

List of Figures

Chapter 1

Introduction

Fluid-structure Interaction (FSI) is present in a wide variety of systems including examples from nature, engineering and biomechanics. The complexity of the fluid mechanics combined with a rigid or flexible body, means many FSI problems are still not fully understood. Engineers have become increasingly interested in FSI in recent years because of its diverse range of applications. The work presented in this thesis concentrates on the interactions between a potential flow and a flexible insert comprising either a single-sided open flow, one or both sides of an otherwise rigid channel, or separating two channel flows, with the aim of understanding the flow-induced structural instabilities and flexible insert behaviour. This may help to aid design and improve the understanding of the structural limitations in a variety of systems.

1.1 Motivation

1.1.1 Open Flows

Many of the investigations into the stability of a flexible surface stem from the Kramer experiments (Kramer, 1957, 1960, 1962), but interest in the transition delaying properties of flexible surfaces dates back much further. An analysis into the swimming capabilities of bottle-nosed dolphins resulted in what is now called *Gray's Paradox* (Gray, 1936) where Gray estimated the maximum power output that a dolphin could exert, and the drag forces on a dolphin (modelled as a flat plate) in a turbulent flow. His results led him to believe that the only

way a dolphin could reach the speeds they are known to swim at, is to delay the transition from laminar to turbulent flow with increasing swimming speed, and hence reduce the drag forces experienced. Although many of Gray's assumptions have since been proven inaccurate and Gray's paradox solved (Fish, 2006, Fish and Hui, 1991), there is still much evidence that compliant surfaces can delay transition to turbulent flow.

Kramer created a range of compliant coatings to resemble dolphin skin and found drag reductions of up to 60%. He believed that this significant drag reduction was due to the suppression of Tollmien-Schlichting waves, which are a means by which a boundary-layer flow transitions from laminar flow to turbulence. With the compliant coating, transition was thought to occur at much higher Reynolds numbers. This theory was later confirmed by Gaster (1988). A comprehensive overview into the transition delaying properties of dolphin skin and compliant walls has been provided by Carpenter et al. (2000).

The Kramer experiments initiated much research into the transition delaying properties of compliant coatings and flexible surfaces, in particular into optimising drag reduction. If a compliant coating is too flexible however, surfaces can themselves become unstable and predicting the onset of surface instabilities has been considered using a variety of methods which will be discussed in Chapter 2.

The applications of understanding this fundamental FSI problem are limited to high (infinite) Reynolds number systems. For the open flow geometry considered in this work these applications might include engineering systems such as the unstable vibrations of steel (flexible) plates of spillways in hydro-power plants and hull panels of modern high-speed ships. This work also has academic significance to further the understanding of fundamental FSI systems.

1.1.2 Channel Flows

The related problem of fluids interacting with flexible channels has a rich history of literature including both experimental and theoretical investigations. A detailed review of the history of studies involving fluid-conveying pipes is provided by Païdoussis and Issid (1974). One of the first notable investigations was that of Bourrières (1939) where the equations of motion for a fluid-conveying cantilever

pipe were derived and their solution compared with experiments. More recently, cantilever flexible plates with applications to modelling the snoring phenomenon have been studied by Huang (1995) and Howell et al. (2009).

More relevant to the present work are flexible pipes fixed at both ends, where early studies of the oscillation frequencies and pipe buckling include those of Weaver and Unny (1973), Weaver and Myklatun (1973) and Weaver and Païdoussis (1977). Understanding these systems has applications for a variety of engineering systems that involve pipelines and flexible pipes, including underwater drilling and the nuclear industry (Johansson, 1960, Miller, 1960) and also biomechanical applications such as airways and blood vessels (Heil and Hazel, 2011).

1.2 Objectives

The aim of this work is to develop methods to model a flexible insert which comprises a two-dimensional open or channel ideal flow with the goal of characterising the plate behaviour. This can be split up into a number of 'sub-objectives' which are as follows:

1. Develop a potential flow model for small-amplitude deflections of a flexible insert in an open flow.

2. Develop a potential flow model for small-amplitude deflections of a flexible insert in a channel flow.

3. Develop a potential flow model for small-amplitude deflections of a flexible insert separating two channel flows.

4. Develop a potential flow model to consider the transient growth and system non-normality of a flexible plate in an open flow.

5. Develop a potential flow model for large-amplitude deflections of a flexible insert in an open flow.

6. Develop a potential flow model for large-amplitude deflections of a flexible insert in a channel flow.

The schematics of some of the systems considered are shown in Figures 1.1 and 1.2. Figures 1.1 (a) and (b) show the open flow cases of Objectives 1, 4 and 5 where a simple elastic plate and a spring-backed flexible plate has been depicted respectively. The channel flow case of Objectives 2 and 6 are illustrated in Figure 1.2 (a) and (b) for the finite and infinite cases respectively. The double sided channel flow of Objective 3 is shown in Figure 1.2 (c).

1.3 Methodology

In order to achieve the objectives outlined, three computational methods are developed, validated and a range of results presented. In all three methods the structural and fluid mechanics are modelled by a finite-difference method and boundary-element method respectively.

Objectives 1, 2 and 3 are achieved by applying a state-space method to calculate the eigenvalues and eigenvectors of the system. These are then analysed, with particular attention paid to predicting the onset and recovery of flow-induced structural instabilities. This methodology is applied to a variety of geometries with particular attention paid to the effect of the proximity of the rigid channel walls (when present). This modelling is applicable to small-amplitude plate deflections.

A theoretical method is also developed for the channel flow whereby the channel is assumed to be infinitely long and the system equations are solved analytically to predict the onset of instability.

The eigenvalues and eigenvectors from the state-space method are then used in a non-modal analysis to establish whether transient growth can cause large plate deflections before the onset of plate instability from the linear predictions.

Finally, the finite-difference method and boundary-element method are coupled to perform time-stepping numerical simulations where a flexible insert comprising both an open and channel flow is modelled, for both small and large deflections.

While it is noted that in practice, many of the applications listed at the end of Sections 1.1.1 and 1.1.2 can feature turbulent flow, the use of potential flow

throughout the present work is justified, as flow separation is not a strong feature of non-lifting surfaces, as considered here. If a thin boundary layer were to be included in this research it would not have a large impact on any numerical results for this reason and the results would stay qualitatively the same. In contrast, the inclusion of a thin boundary layer has a much more significant impact in the case of lifting aerofoils as flow separation is present and so inclusion of wake effects is essential. This justification for not including a boundary layer in the case of a non-lifting surface does not hold for very narrow channels as the boundary layer thickness relative to the channel height may be non-negligible.

1.4 Thesis Layout

The remainder of the thesis consists of a further 5 chapters throughout which each objective is addressed using the range of methods outlined:

Chapter 2

A literature review is provided which gives a history of previous investigations into the FSI of flexible surfaces. The types of surface instabilities will be characterised and stability classifications discussed. Investigations of similar or relevant geometries will be considered along with comparisons between the methods used and alternative modelling techniques.

Chapter 3

The linear potential flow model is presented in Chapter 3. Initially, the system equations are given along with the application of the finite-difference and boundary-element methods. The state-space method and analytical solution are then detailed. Validation of the state-space method for the open-flow case is presented. Validation of the channel flow geometry and theoretical solution are presented alongside a range of results where different types of flexible insert are considered for the channel flow including simple plates, damped plates, flexible membranes and spring-backed plates.

Chapter 4

The transient-growth methods used are outlined and results are presented

for a simple and damped plate in the open flow with comparison to other investigations. Different mass ratios are considered and the effect of the proximity of an upper channel wall is considered for the channel flow case.

Chapter 5

The numerical time stepping routine is described with validation given for large deflections in the open flow and small deflections within a channel. A theoretical investigation and an iterative method to solve the time independent system is also outlined. A range of results are presented with comparisons between the methods and large amplitude deflections in an open and channel flow are characterised.

Chapter 6

A summary of the overall conclusions drawn with key findings is outlined. Comment is made on limitations and future work.

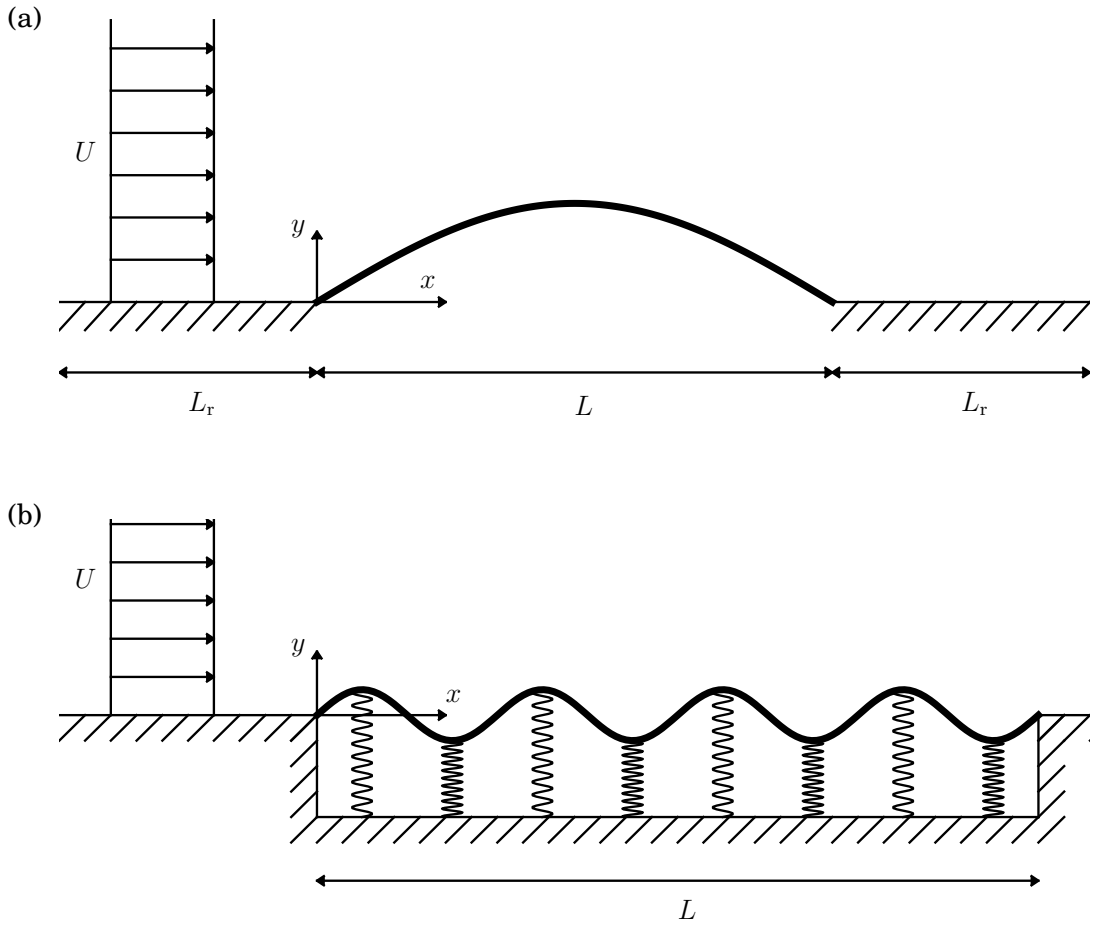

Figure 1.1: Schematics of the open fluid-structure interaction systems studied; (a) Finite simple elastic plate, (b) Finite spring-backed flexible plate.

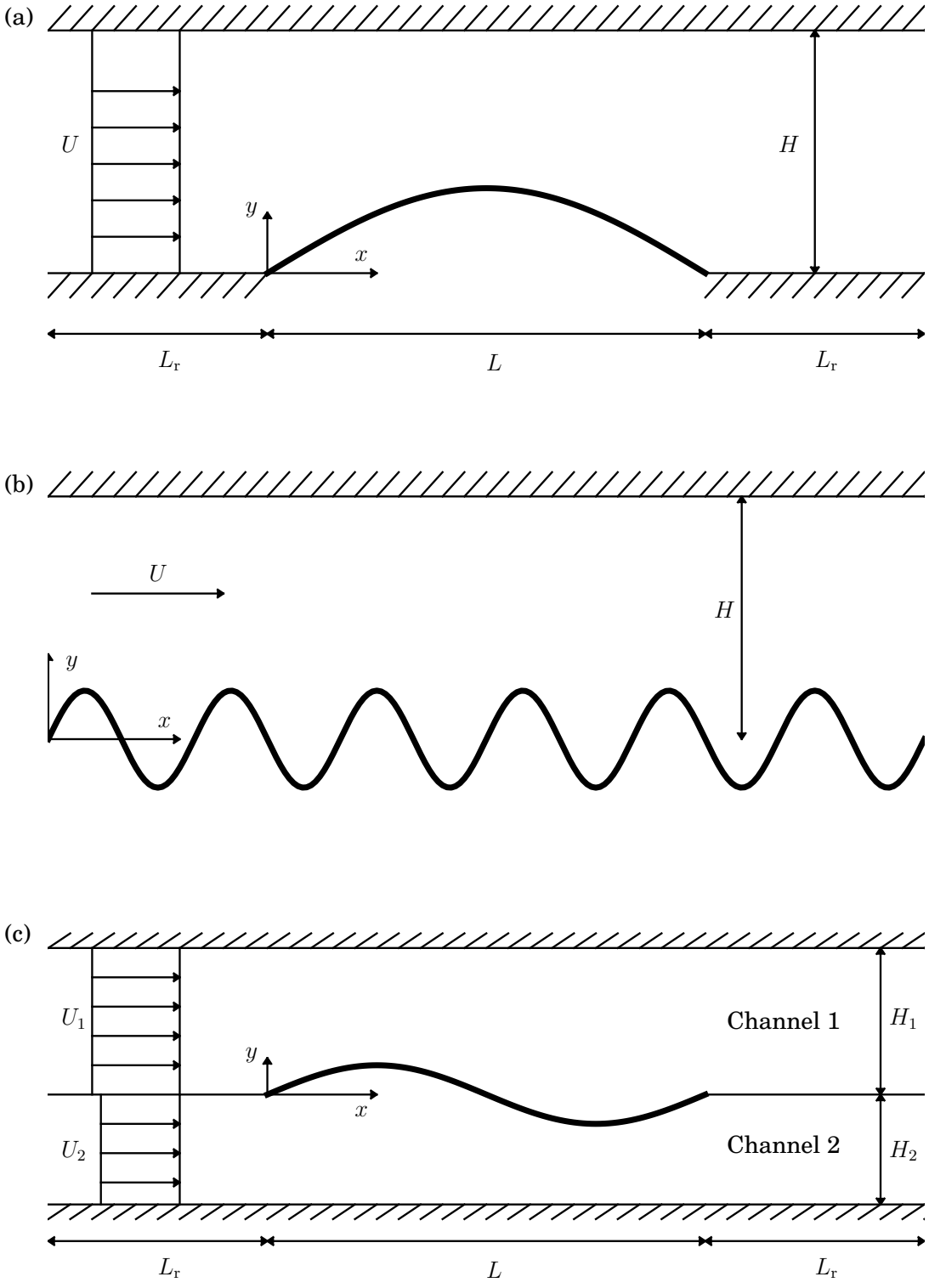

Figure 1.2: Schematics of the channel fluid-structure interaction systems studied; (a) Finite simple elastic plate, (b) Infinitely long channel with one wall flexible, (c) Finite flexible plate separating two channel flows.

Chapter 2

Literature Review

This chapter contains details of a variety of previous studies that are relevant to the work presented here; flexible surfaces and compliant coatings. There is an emphasis to the surface instabilities that occur. The types of instabilities will first be considered with their different classifications. Investigations into the linear and nonlinear deflections of open and channel flows for both inviscid and viscous flows are described and relevant experiments considered.

2.1 Instability Types

Inspired by the experiments of Kramer (1960) that showed a significant drag reduction is possible by the use of compliant coatings, an analytical investigation by Benjamin (1960) revealed three distinct instability types present in the case of a two-dimensional flow past a flexible boundary. This investigation used linear theory, and so assumed that the deflections of the surface were small. Benjamin introduced a class system for the instability types:

Class A - Tollmien-Schlichting waves present in the fluid which are stabilised by a compliant boundary when compared with a rigid boundary, but that are destabilised by internal damping in the flexible surface.

Class B - Surface waves which are stabilised by damping in the flexible surface such as travelling wave flutter.

Class C - Instabilities caused by an interaction between the class A fluid waves and the class B surface waves, similar to a Kelvin-Helmholtz instability.

The properties of the compliant wall such as stiffness and surface damping, may stabilise one type of instability at the expense of destabilising another and there are different approaches that can be taken to optimising the overall drag reduction of a compliant coating. This system of instability classification is the first of three notable systems (Gad-el-Hak, 2002).

The class A instabilities, Tollmien-Schlichting waves, were first observed by Prandtl (1921) and explained by Tollmien (1929) and Schlichting (1933) as a means of transition from laminar to turbulent flow. These initially linear low-amplitude waves are initiated by an external disturbance, and then either decay or grow as they move downstream in the boundary layer. While they are low-amplitude and linear they can be considered to be two dimensional and these linear waves are found in approximately 80% of the transition region (Houghton and Carpenter, 1993). Towards the end of the transition region, the waves grow rapidly and become three-dimensional, making the boundary layer nonlinear and complex.

The class B instability, renamed by Carpenter and Garrad (1986) as travelling wave flutter, is similar in speed to the free-stream speed. It was investigated by Benjamin (1960) and Landahl (1962) and requires a shear layer to grow but is otherwise largely unaffected by viscosity.

The class C instabilities, occur when the surface instability interacts with a fluid instability. These instabilities are similar to a Kelvin-Helmholz instability which can be seen at the boundary between fluids of different velocities, such as wind over water.

By modelling a two-dimensional, infinitely long flexible surface in an incompressible potential flow, Landahl (1962) refined Benjamin's class system. He showed that there is an irreversible energy exchange between the fluid and solid for class A and B instabilities. Class A instabilities are stabilised by an energy transfer from the fluid to the surface and the opposite holds true for class B waves.

Another classification system was devised by Carpenter and Garrad (1985, 1986). They split the instabilities into two categories: fluid-based instabilities such as Tollmien-Schlichting waves and flow-induced surface instabilities such as

divergence.

Divergence is either a static instability or a slowly downstream-travelling instability that occurs when the hydrodynamic forces on the surface are greater than the restoring forces causing the disturbance to grow. Lucey and Carpenter (1992) showed that under the Landahl (1962) classification scheme, divergence is class C instability as damping does not alter its onset.

The final, notable classification is that of Huerre and Monkewitz (1990) where the instabilities are either convective and grow spatially (Tollmien-Schlichting waves and travelling wave flutter) or absolute where instabilities grow in time (static divergence and the inviscid Kelvin-Helmholtz instability).

The viscous instabilities such as Tollmien-Schlichting waves and travelling wave flutter are not considered here as a potential flow model is used throughout this thesis. The structural instabilities of divergence and modal-coalescence flutter will be considered, in particular, the instability onset speeds and how they vary under different conditions.

2.2 Open Flow

The system depicted in Figure 1.1 (a), which is consider in Chapters 4.2.1 and 5.3.1, was first studied for aeronautical applications (Bisplinghoff et al., 1955, Dugundji et al., 1963) both experimentally and theoretically. Experimental studies will be discussed in greater detail in Chapter 2.4. Many investigations concentrate on the fluid instabilities and Tollmien-Schlichting waves (Carpenter and Garrad, 1985, Davies and Carpenter, 1997a), but more relevant to this work are the studies that concentrate on the flow-induced surface instabilities.

The early study of Weaver and Unny (1970) for a finite flat plate in a potential flow used a Galerkin approach to predict instabilities based upon a normal-mode decomposition of system disturbances. This method constructs a system solution as the sum of a set of discrete orthogonal functions usually chosen as the in vacuo structural modes because they each automatically satisfy the boundary conditions of the structural side of the system. They predicted that at low flow velocities the plate is neutrally stable, first losing its stability to single mode divergence,

and with increasing flow speed, divergence recovery occurs. At sufficiently high flow speeds a modal-coalescence type of flutter dominates the system response. This is also found true in the results presented in this thesis. This method is only applicable for the linear system and has the limitations of a solution that is dependent upon a chosen number and form of modes. The eigenvalue analysis used in Chapter 3, while still only applicable to a linear system, has the advantage over a Galerkin approach by not being dependent on the chosen modes. A similar method to the Galerkin approach was adopted by Kornecki et al. (1976) who confirmed that a plate fixed at both ends will lose its stability to divergence but that a cantilevered plate will lose its stability to a flutter type instability.

By using a travelling-wave assumption, Carpenter and Garrad (1986) considered the stability of an infinitely long compliant surface where an analytical solution method invokes a continuous spectrum of locally defined normal modes to characterise system disturbances. The ensuing solutions then predict instability in the limit of infinite time; i.e. as a boundary-value problem, in the form of the most unstable system eigenmode. They also predicted the flow speed and wavenumber at which divergence and modal-coalescence flutter occur in a potential flow and compare the solutions with a model to incorporate the viscous effects and a more complex model where the compliant surface is of finite length. A similar method to that used by Carpenter and Garrad (1986) is extended in Chapter 3.1.4 to be applicable for an infinitely long flexible channel and serves as a useful comparison between the finite channel results of the eigen-analysis.

Since the 1990's advances in computing capabilities have made numerical simulations more viable than in previous years. The hydroelastic behaviour of a compliant wall within a potential flow was demonstrated in the linear investigations of Lucey (1989) and Lucey and Carpenter (1992) and the nonlinear investigations of Lucey et al. (1997). The same methodology has been used in this work to act as a validation of the linear analysis of Chapter 3, and also extended to include features which make it applicable to the channel flow in Chapter 5. The linear simulations show that divergence onset is unaffected by the presence of structural damping and takes the form of a wave travelling slowly downstream. They also demonstrated that the role of damping is to reduce the growth rate of the in-

stability. Numerical simulations of compliant walls interacting with a boundary layer were presented by Alekseyev (2002), Wiplier and Ehrenstein (2000, 2001) and Visbal and Gordinier (2004) to consider the loss of stability to the convective Tollmien-Schlichting waves.

More recently, Pitman and Lucey (2009) presented a versatile method by which system eigenvalues can be directly extracted from the discretised system and this method is valid even for structurally inhomogeneous systems. Although this approach is more computationally expensive when compared to the traditional Galerkin methods, it has the advantages of not making assumptions about the number of modes and mode shapes to construct a solution. This method was extended by Tan et al. (2013) to model a flexible panel with a localised stiffness as a means to delaying the onset of divergence and has been extended for this work to be applicable for the channel flow.

All of these linear studies for incompressible inviscid flow are in agreement about the non-dimensional flow velocity in that a flexible panel or compliant wall will lose its stability to divergence, and that at higher flow speeds, flutter will occur. However, recent work shows that divergence is not necessarily the route to large-amplitude deformations.

Schmid and de Langre (2003) and Coppola and de Luca (2010) demonstrated theoretically that very significant transient growth of perturbations can occur through the non-normality of the system equations. The theoretical framework established in these non-modal analyses maximises the time-evolution of an energy norm for the fluid-structure system as an envelope over all potential initial states. This captures the growth of disturbances that can bypass conventional linear-instability mechanisms to reach finite amplitudes which may occur for system control parameters (e.g. the flow speed) below the critical values based on a modal analysis. Tsigklifis and Lucey (2013) have recently extended the modelling of Pitman and Lucey (2009) to analyse non-modal transient growth in boundary-layer flow over a compliant panel in a three-dimensional system. The non-modal methodology has also been applied here in Chapter 4 for both the open and channel flow finite geometries depicted in Figures 1.1 (a) and 1.2 (a).

Theoretical predictions of this type of phenomenon were confirmed in the ex-

perimental studies of Hémon et al. (2006) and Schwartz et al. (2009). The papers give the real world example that transient growth might explain the premature structural fatigue that has been observed in structures subjected to wind. Both papers demonstrate transient growth of energy, of an aerofoil below the critical flutter velocity. Schwartz et al. (2009) shows that for a nonlinearly flexible aerofoil, transient growth can cause a by-pass transition to flutter below the critical flow velocity.

Two- and three-dimensional instabilities in a two-dimensional boundary layer were studied by Carpenter and Gajjar (1990) who investigated how different wall properties affect travelling wave flutter. In particular, they looked at the differences between isotropic and anisotropic compliant surfaces. Their results agreed with those of Benjamin (1960) in that for an isotropic wall, travelling wave flutter is caused by an irreversible energy transfer to the wall. Both two- and three-dimensional numerical simulations were performed by Lucey (1998) for a finite flexible panel. They drew comparisons with previous studies where an infinitely long panel was assumed and found that the long-time response gives differing results but at early times, the infinite assumption is accurate, such as the prediction of instability onset in an infinity long system as demonstrated in Chapter 3.1.4.

Investigations into the large amplitude (nonlinear) deflections of flexible walls include the numerical simulations of Lucey et al. (1997). They showed small amplitude disturbances growing to nonlinear amplitudes within the divergence range of flow speeds that are dominated by the fundamental mode. The inclusion of damping caused a static buckled state with time whereas in the absence of damping nonlinear oscillations occurred. These findings agree with those of Reynolds and Dowell (1993) who used numerical integration of the full nonlinear equations of motion. Using a CFD package, simulations were performed by Knight et al. (2010) alongside a theoretical treatment of the two-dimensional steady-state. Other nonlinear studies include the potential flow model of Peake (2001), the two- and three-dimensional model of Geveci and Walker (2001) and the computational method incorporating a boundary layer of Wiplier and Ehrenstein (2000). A more detailed account of some of the recent methods and results

into nonlinear aeroelasticity is provided by Dowell et al. (2003).

The nonlinear numerical simulation methods of Lucey et al. (1997) is extended in Chapter 5 to make it applicable to the channel flow. In addition, the theoretical steady-state analysis of Knight et al. (2010) is adapted to include further features of the flexible insert such as flexural rigidity and divergence onset. This allows a useful comparison between the maximum and mean-state amplitudes of an unstable nonlinear insert.

2.3 Channel Flows

Provided here is an overview of some relevant channel-flow studies where the channel, or part thereof, is compliant. A more detailed review of some of the physiologically inspired research is provided by Heil and Hazel (2011). With a flexible insert comprising the wall of a channel, the present work bears similarity with studies of fluid conveying flexible pipes.

There is a large body of theoretical and computational modelling on viscous flow in channels and pipes. These effectively address the low-Reynolds-number range - unsteady laminar-flow - of fluid-structure interactions within the canonical system. The system is shown to support a range of instabilities that include divergence, travelling-wave flutter, Tollmien-Schlichting waves and nonlinear self-excited oscillations.

Tollmien-Schlichting waves and flow-induced surface waves were studied in a compliant channel by Davies and Carpenter (1997b). Considering linear deformations for an infinitely long flexible channel they showed, inter alia, that different instabilities, for example Tollmien-Schlichting waves and travelling-wave flutter, can interact with each other. They found that channel walls which are effective at destabilising Tollmien-Schlichting waves are also likely to suppress divergence when the flow is laminar.

Huang (2001) modelled small-amplitude deformations of a finite tensioned membrane, found the eigenmodes of divergence and flutter and considered the effect of the membrane properties and up- and down-stream channel length on the system. Huang discovered that flutter and divergence occur at similar flow

velocities, both can occur simultaneously and that increased viscosity has a destabilising effect on flutter. This differs to the inviscid results presented here where, for a finite plate, modal-coalescence flutter occurs at a higher flow speed then that of divergence.

Jensen and Heil (2003) developed predictions for the frequency and growth rate of instabilities. Models for large-amplitude deformations of a finite membrane in a channel have been developed by Luo and Pedley (1996, 2000) to simulate sustained self-excited oscillations of the membrane. Spatio-temporal waves were found by Pitman and Lucey (2010) and a boundary-layer model where the channel has an inviscid core was developed by Pihler-Puzović and Pedley (2013). Other high-Reynolds number flow studies include those of Guneratne and Pedley (2006), Kudenatti et al. (2012) and Jensen and Heil (2003).

Pipe-buckling (divergence) and flutter have been predicted at sufficiently high flow speeds, for example, by de Langre and Ouvrard (1999) and Doaré and de Langre (2002), in an infinitely long pipe comprising parallel flexible surfaces in the undeformed state. In these studies, a one-dimensional (or plug) flow is assumed in which the flow follows the curve of the deformed channel (or pipe) via the Païdoussis equation (Païdoussis, 1998, 2003). Of closer similarity to the present work are studies modelling an inviscid fluid.

All of the aforementioned channel flow studies include at least some viscous effects which are not included in the current methods, however it can been seen that the instabilities of divergence and flutter occur in both the viscous studies and the potential flow models considered here.

In contrast to studies using the Païdoussis equation, the study of Weaver and Païdoussis (1977) features flow curvature varying across the channel (the y-direction in Figure 1.2 (a)). They model a two-dimensional potential flow in an infinitely long flexible channel using the travelling-wave assumption of disturbances in the streamwise direction and a Galerkin approach for a finite section of the channel. They found that: (i) when the walls display sinuous behaviour, divergence-onset flow speed increases as the channel height decreases; and (ii) when the walls display varicose behaviour, divergence-onset flow speed decreases as the channel height decreases. The first can be explained by the decrease in

destabilising centrifugal force for a reduced mass of fluid traversing the curved path of a channel deformation. The second can be understood as arising from an increase in the gradient of flow curvature across the channel forced by a reduction in channel height. The varicose case is similar to the channel flow system considered here as there is a variation to the streamline curvature present across the channel width and the results shown here also show that divergence-onset flow speed decreases as the channel height decreases.

The eigenvalues are analysed for an infinitely long channel with one rigid and one flexible wall for an inviscid fluid by Bach et al. (2010, 2011a,b) and for a viscous flow by Bach et al. (2012). These studies consider, amongst other characteristics, the energy transfer and the effect of changing the mass ratio of the system and the onset of instability is found.

Guo and Paidoussis (2000) considered the stability of a flexible plate with various boundary conditions, inside a rigid channel. In this study the flexible plate has flow on both sides resembling the double sided channel flow of this work (Figure 1.2 (c)), but with the key difference that the flow is not separated. Using a Galerkin approach it was found that a pinned-pinned plate loses its stability to divergence, and later, single mode and coupled mode flutter. Other notable studies of inviscid channel flows are those of Epstein et al. (1995) who determine the effect of Mach number and mass ratio on flutter onset velocity, Huang (1998) who consider self-excited oscillations and Mandre and Mahadevan (2010) who compare the critical flow speeds found using a viscous and inviscid flow.

2.4 Experimental Studies

Since the significant drag reduction that was reported by Kramer (1960), many experiments have attempted to recreate, or refine this success. Babanko (1973) and Babanko et al. (1969) attempted to develop a compliant coating that better resembled dolphin skin and Gaster (1988) performed a series of experiments which provided evidence that Tollmien-Schlichting waves are suppressed by wall compliance. Their results agreed well with existing theoretical data. Kornecki

et al. (1976) conducted a series of experimental and theoretical investigations of fluids interacting with compliant panels for a variety of boundary conditions at the leading and trailing edges of the panel. A panel with pinned boundary conditions at both ends was shown to lose stability first to divergence agreeing with the existing theoretical predictions. Aeroelastic stability was investigated by Dugundji et al. (1963) who observed travelling wave flutter in a wind tunnel. Their results compared well with their theoretical findings for flutter speed and wavelength but considerable differences were seen for wave speed and flutter frequency.

Hémon et al. (2006) and Schwartz et al. (2009) have performed experiments into transient growth, such as that demonstrated in Chapter 4. Hémon et al. (2006) demonstrated the existence of transient growth by measuring the transient evolution of energy where the system considered is an aerofoil subject to air flow. Schwartz et al. (2009) showed that nonlinear flutter of a flexible aerofoil in a wind tunnel is possible at flows speeds before the linear critical flutter velocity.

Experimental work that complements the pipe- and channel-flow modelling includes that of Dodds and Runyan (1965) who found a critical flow velocity for static divergence for a high-velocity fluid through a simply supported pipe and Weaver and Païdoussis (1977) who observed a flapping instability in a flattened tube and found that the critical flow speed at which flapping occurred was reduced with the gap between tube surfaces. The experiential results of Weaver and Païdoussis (1977) are compared to the results in Chapter 3.3.1. However, most experimental studies - for examples see Conrad (1969), Gavriely et al. (1989), Bertram et al. (1990), Bertram and Castles (1999) and Bertram and Elliott (2003) - have tended to focus on large-amplitude deformations and the collapse of flexible channels in the context of biomechanical applications such as blood-flow in the smaller vessels. Recent reviews of the rich body of work in this field have been presented by Grotberg and Jensen (2004) and Heil and Hazel (2011).

2.5 Summary

It is known that compliant coatings can be used to suppress the growth of Tollmien-Schlichting waves and hence offer significant drag reduction by means of delayed transition to turbulence. Flexible surfaces however, can themselves become unstable. A variety of linear-investigations have shown that flow-induced surface instabilities exist in the forms of divergence and modal-coalescence flutter and that with increasing flow speed, the surface will first lose its stability to divergence for surfaces held at both ends. This holds true for both the open flow and channel flows depicted in Figures 1.1 and 1.2 respectively. Experimental and theoretical investigations indicate that nonlinear surface deformations are possible before the linear prediction of surface instability by means of transient growth. Studies into nonlinear deflections show that large amplitude oscillations occur.

Although there is already rich and diverse literature covering the FSI of flexible surfaces including, but not limited to, the studies discussed in this literature review, there are many elements that remain to be understood fully. Those considered in this thesis include the effect of the proximity of the upper channel wall on the stability bounds of a flexible channel flow, transient growth effects of a potential flow, and the nonlinear behaviour of a flexible surface within a channel. The remainder of this thesis will attempt to address these and is split into three main investigations: linear disturbances, transient growth and nonlinear disturbances. All the work here will be using the potential flow assumption and so the results are applicable only to high (infinite) Reynolds number systems.

Chapter 3

Linear Stability of a Fluid-Loaded Flexible Insert

This chapter investigates the stability of a finite flexible plate in each of an open flow, comprising one wall of an inviscid channel flow and separating two channel flows. The method used is detailed whereby a finite-difference method to model the structural mechanics is coupled with a boundary-element method to model the fluid mechanics. Using a state-space formulation the eigen solution is analysed to predict the flow speeds at which divergence instability, divergence recovery and modal-coalescence flutter occur for given system parameters.

An open flow is considered to compare with previous investigations as a means of validation that the structural and fluid mechanics are implemented correctly.

The new aspect of this work is to consider the stability of a flexible insert comprising one wall of an inviscid channel flow and results are presented for a variety of different insert types which are then compared with other studies and experiments. A separate analytical method is developed for an infinitely long channel where either one or both walls are flexible and this is compared to the state-space solution for plates with a high order mode shape. Finally, eigen-analysis is performed on a double sided channel and a range of results are presented.

The linear assumptions made are only valid for small plate deflections and although the results give accurate predictions for instability onset, to consider large amplitude deformations, alternative modelling techniques should be considered;

these are addressed in Chapter 5.

3.1 Method

3.1.1 Governing Equations

Structural Mechanics

The motion of a thin flexible plate is described by the extended and linearised one-dimensional beam equation,

$$\rho_{\mathrm{m}} h \frac{\partial^2 \eta}{\partial t^2} + d\frac{\partial \eta}{\partial t} + B\frac{\partial^4 \eta}{\partial x^4} + K\eta - T\frac{\partial^2 \eta}{\partial x^2} = -\Delta p(x, 0, t), \tag{3.1}$$

where $\eta\,(x, t)$, ρ_{m}, h, d and B are respectively the plate's vertical displacement, density, thickness, damping and flexural rigidity, K is the stiffness of the uniformly distributed spring foundation, T is a uniform tension and Δp is the unsteady pressure perturbation. The flexural rigidity is defined by,

$$B = \frac{Eh^3}{12(1-\nu^2)}, \tag{3.2}$$

where E is the elastic modulus and ν is Poisson's ratio. This model is valid for small deflections of the surface. The damping, spring and tensioned terms can be neglected from this equation if not required for the type of flexible insert being modelled.

To model the structural mechanics a finite-difference method, developed by Lucey and Carpenter (1992), is used whereby the surface of the plate is discretised into N_{f} mass points, located at each panel end. Each panel then has a control point at its centre. This allows for convenient coupling with the flow mechanics. This method was also successfully adopted by Howell (2006) and Evetts et al. (2014) for a cantilever beam, and Pitman and Lucey (2009) and Tan et al. (2010) for a plate with fixed end points. Hinged boundary conditions are applied to the ends of the flexible insert of the form,

$$\eta = \frac{\partial^2 \eta}{\partial x^2} = 0. \tag{3.3}$$

The discretised insert for the case of a simple elastic plate in an open flow can be seen in Figure 3.1 (a), along with details of the finite-difference and boundary element methods in Figure 3.1 (b).

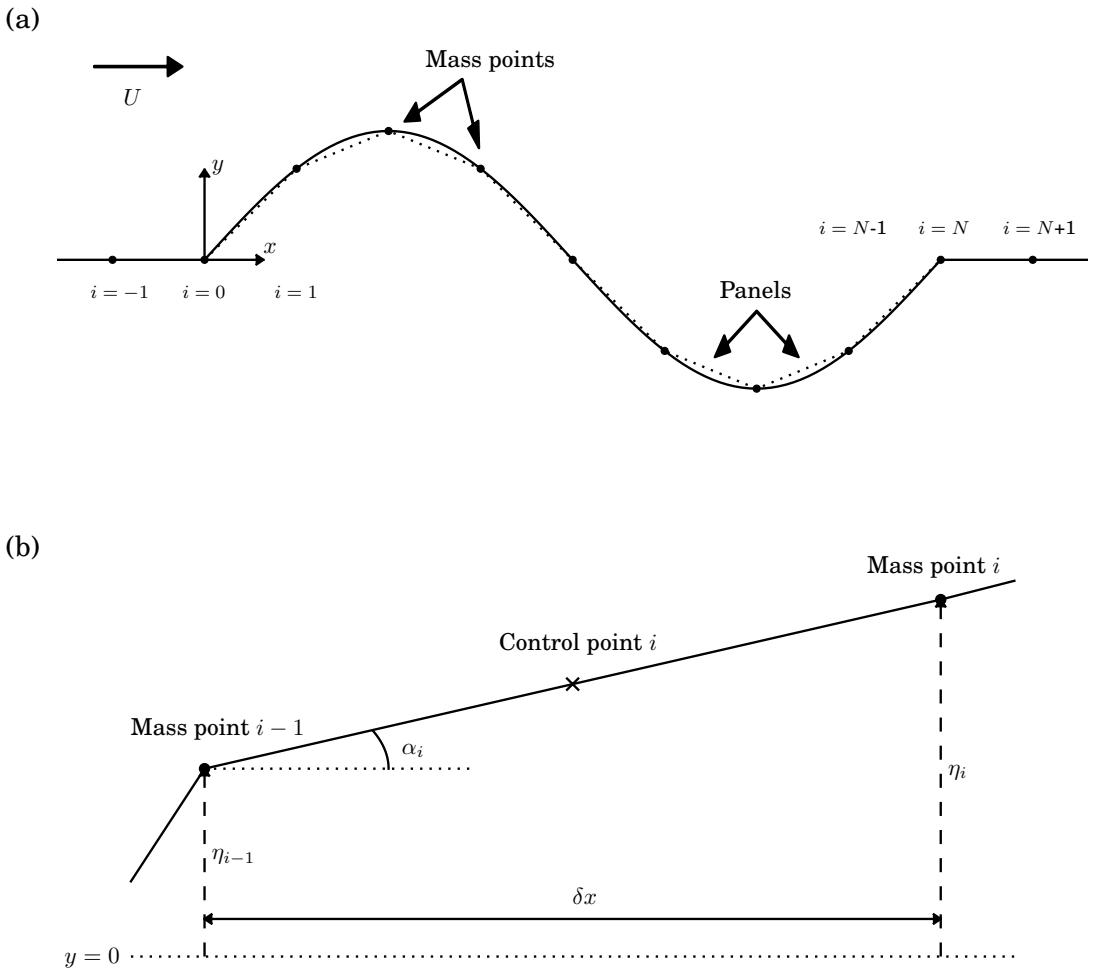

Figure 3.1: (a) Schematic of the discretised open flow for a simple elastic plate and (b) details of the boundary-element method. Adapted from Lucey et al. (1997).

Flow Solution

Assuming an irrotational and incompressible flow allows the introduction of a velocity perturbation $\phi(x, y, t)$ which satisfies Laplace's equation,

$$\nabla^2 \phi = 0, \tag{3.4}$$

for modelling an ideal fluid. The fluid pressure is found from the unsteady Bernoulli equation,

$$\Delta p = -\rho_{\mathrm{f}} U \frac{\partial \phi}{\partial x} - \rho_{\mathrm{f}} \frac{\partial \phi}{\partial t}, \tag{3.5}$$

where ρ_f and U are respectively the fluid density and flow speed. The linearised (for small interfacial displacement) fluid-solid boundary conditions are,

$$\frac{\partial \phi}{\partial y} = \frac{\partial \eta}{\partial t} + U\frac{\partial \eta}{\partial x} \qquad \text{at} \qquad y = 0,\ 0 \leq x \leq L, \tag{3.6}$$

for the flexible surface and,

$$\frac{\partial \phi}{\partial y} = 0 \qquad \text{at} \qquad y = H, \text{ and } y = 0,\ x < 0 \text{ and } x > L, \tag{3.7}$$

for the rigid surfaces up- and down-stream of the flexible insert (where used) and for the rigid channel walls where H is the channel height and L is the length of the flexible surface as demonstrated in Figure 1.2 (a). These boundary conditions enforce the no-flux condition.

When considering a channel geometry the formulation described above assumes that the pressure of the mean flow within the channel exactly balances that outside of the channel so that in its undisturbed state the flexible insert rests along $y = 0$.

When using the boundary-element method, stability is not affected by up- and down-stream boundary conditions. Channel flows usually require prescription of the up- and down-stream boundary conditions which, for a viscous flow, are either velocity or pressure conditions at entry and exit. This is needed as the viscous effects cause a pressure drop along the channel. The effect of the boundary conditions for a finite membrane in Poiseulle Flow was considered by Huang (2001) where it is showed that changing the boundary conditions to have an open up- or down-stream end, changes the eigenvalues of the system.

3.1.2 Linear Pressure and State-Space Method

To solve the governing equations the method developed by Pitman and Lucey (2009) is extended in which a finite-difference representation of the structural dynamics is fully coupled with a boundary-element flow solution to derive a single matrix equation from which the eigenvalues and eigenvectors are then directly extracted. The main advantage of this method, over the traditional Galerkin method, is that it avoids a presumption that the eigenmodes of the coupled fluid-structure system can be readily assembled from a finite set of orthogonal

functions that are usually the in vacuo eigenmodes of just the structure. This advantage can be especially useful for structurally inhomogeneous flexible walls for which analytical orthogonal functions are unwieldy or simply unavailable. A more complete discussion of its advantages is provided in the Pitman and Lucey (2009) paper.

The flexible and rigid surfaces are each discretised into panels (giving the system a total of N panels) and singularities, satisfying the Laplace equation, are distributed over each panel. The singularities chosen are sources and sinks as a non-lifting surface is being modelled. The linearised theory developed by Lucey and Carpenter (1992) is used wherein the singularities on the deformed insert do not move with the displaced surface but stay fixed on the undisturbed plane similar to the approach of thin-aerofoil theory. For details of panel methods with aerofoils see Houghton and Carpenter (1993).

The perturbation potential given by applying the boundary-element method is,

$$\phi(r) = \frac{1}{2\pi} \int_0^L \sigma(r_s) \ln|r - r_s| \mathrm{d}s, \tag{3.8}$$

where σ is the source strength distribution, r is any point in the fluid domain considered and r_s is the locus vector of the surface-fluid interface. The strengths of the singularities are determined by the enforcement of the kinematic boundary conditions of Equations (3.6) and (3.7) at the control point of each panel, where the singularity in Equation (3.8) is properly treated. The disturbance normal velocity, tangential velocity and velocity potential are then given by,

$$\{u_N\} = \left[I^N\right] \{\sigma\}, \tag{3.9a}$$

$$\{u_T\} = \left[I^T\right] \{\sigma\}, \tag{3.9b}$$

$$\{\phi\} = \left[I^\Phi\right] \{\sigma\}, \tag{3.9c}$$

where $\left[I^N\right]$, $\left[I^T\right]$ and $\left[I^\Phi\right]$ are respectively the normal, tangential and potential influence coefficient matrices and σ is the source strength vector. The linear approximation removes the time dependence of the influence-coefficient matrices so they need only be calculated once and also removes the time dependence on the normal velocity influence calculated of Equation (3.9)a. The linearised normal

influence coefficients are then,

$$\left[I^N\right] = \frac{1}{2}\left[I\right], \tag{3.10}$$

where $[I]$ is the identity matrix. This results in each singularity strength being independent of all other singularity strengths. The boundary condition Equation (3.6) can be applied at $y = 0$ when using this linear approximation. The details of calculating the linear and nonlinear influence coefficients are included in Chapter 3.1.3.

The pressure perturbation at the mass points of the flexible insert is found using Equation (3.5) in the form,

$$\begin{aligned} -\{\Delta p\} = 2\rho_{\mathrm{f}} U^2 \left[I^T\right]\left[D_1\right]\{\eta\} + 2\rho_{\mathrm{f}} U \left[I^T\right]\left[D^+\right]\{\dot{\eta}\} \\ +2\rho_{\mathrm{f}} U \left[I^\Phi\right]\left[D_1\right]\{\dot{\eta}\} + 2\rho_{\mathrm{f}} \left[I^\Phi\right]\left[D^+\right]\{\ddot{\eta}\}, \end{aligned} \tag{3.11}$$

for the discretised system where $[D^+]$ is a spatially averaging matrix to evaluate the pressure at the mass points of each panel, rather than the panel ends, and $[D_n]$ is an n^{th} order differentiation matrix. The four terms on the right-hand side of Equation (3.11) are the hydrodynamic stiffness, hydrodynamic damping (middle two terms) and the hydrodynamic inertia respectively. Alternatively, Kornecki et al. (1976) respectively describes these as the forces arising from the centrifugal, Coriolis and linear (vertical) accelerations of fluid elements in the flow past the deforming wall. The latter description as a Coriolis force better indicates that the hydrodynamic-damping component of the fluid loading does not cause energy-dissipation; its principal effect is to couple the system modes.

Equation (3.1) written in finite-difference form is,

$$\rho_{\mathrm{m}} h\{\ddot{\eta}\} + d\{\dot{\eta}\} + B\left[D_4\right]\{\eta\} + K\{\eta\} - T\left[D_2\right]\{\eta\} = -\Delta p(x, y, t), \tag{3.12}$$

and by matching the pressure at the fluid-solid boundary using Equations (3.11) and (3.12), a single matrix equation is derived of the form,

$$\{\ddot{\eta}\} = [E]\{\dot{\eta}\} + [F]\{\eta\}, \tag{3.13}$$

where,

$$[E] = \left[-\rho_{\mathrm{m}} h\left[I\right] + 2\rho_{\mathrm{f}}\left[I^\Phi\right]\left[D^+\right]\right]^{-1}\left[d\left[I\right] - 2\rho_{\mathrm{f}} U\left[I^\Phi\right]\left[D_1\right] - 2\rho_{\mathrm{f}} U\left[I^T\right]\left[D^+\right]\right] \tag{3.14}$$

and

$$[F] = \left[-\rho_{\mathrm{m}} h\,[I] + 2\rho_{\mathrm{f}}\left[I^{\Phi}\right]\left[D^{+}\right]\right]^{-1}\left[B\,[D_4] + K\,[I] - T\,[D_2] - 2\rho_{\mathrm{f}} U^2\left[I^{T}\right][D_1]\right]. \tag{3.15}$$

Using standard state-space formulation, Equation (3.13) can be re-written as,

$$\{\dot{x}\} = [H]\,\{x\}, \tag{3.16}$$

where,

$$\{x\} = \left\{ \begin{array}{c} \{\eta\} \\ \{\dot{\eta}\} \end{array} \right\} \tag{3.17}$$

and

$$[H] = \left[\begin{array}{c} [0]\,[I] \\ [F]\,[E] \end{array} \right]. \tag{3.18}$$

The eigenvalues S and eigenvectors W of this system are then extracted from $[H]$, where $S = S_{\mathrm{R}} + \mathrm{i}S_{\mathrm{I}}$ is the complex frequency of the plate, and the eigenvectors can be used to assemble the eigenmode of the flexible insert $\eta\,(x,t)$.

In order to solve this system of equations and extract the eigenvalues and eigenvectors from Equation (3.16), the linear algebra toolbox 'linalg', which is part of the SciPy library for the Python programming language, is used with Python 2.7.

Variation for Double Sided Channel

When a double sided channel is being modelled, the pressure perturbation from Equation (3.1) becomes,

$$\Delta p(x,0,t) = \Delta p_1(x,0,t) - \Delta p_2(x,0,t), \tag{3.19}$$

where $\Delta p_1(x,0,t)$ and $\Delta p_2(x,0,t)$ are the pressure perturbations from Channel 1 and Channel 2 respectively as depicted in Figure 1.2 (c). There is now a velocity perturbation from each of the channels, $\phi_n\,(x,y,t)$, for $n = 1,2$ denoting the upper and lower channels respectively.

The Bernoulli equation then becomes,

$$\Delta p_n = -\rho_n U_n \frac{\partial \phi_n}{\partial x} - \rho_n \frac{\partial \phi_n}{\partial t} \tag{3.20}$$

and the boundary conditions,

$$\frac{\partial \phi_1}{\partial y} = 0 \qquad \text{at} \qquad y = H_1, \tag{3.21a}$$

$$\frac{\partial \phi_n}{\partial y} = \frac{\partial \eta}{\partial t} + U_n \frac{\partial \eta}{\partial x} \qquad \text{at} \qquad y = 0, \tag{3.21b}$$

$$\frac{\partial \phi_2}{\partial y} = 0 \qquad \text{at} \qquad y = -H_2, \tag{3.21c}$$

for $n = 1, 2$.

In Equation (3.13), the matrices $[E]$ and $[F]$ are now defined,

$$[E] = \sum_{n=1}^{2} (-1)^{n+1} [A_n] \left[-2\rho_n U_n \left[I_n^{\Phi} \right] [D_1] - 2\rho_n U_n \left[I_n^{N} \right] \left[D^{+} \right] \right], \tag{3.22a}$$

$$[F] = \sum_{n=1}^{2} (-1)^{n+1} [A_n] \left[B [D_4] - 2\rho_n U_n^2 \left[I_n^{T} \right] [D_1] \right] \tag{3.22b}$$

where,

$$[A_n] = \left[-\rho_{\mathrm{m}} h [I] + 2\rho_n \left[I_n^{\Phi} \right] \left[D^{+} \right] \right]^{-1}. \tag{3.23}$$

for $n = 1, 2$.

This modelling allows each channel to have its own fluid density, flow velocity and channel height. It is noted that this model does not include the effects of gravity and thus fixing the dimensions of Channel 1 and varying the dimensions of Channel 2 yields the same results as fixing Channel 2 and varying Channel 1.

3.1.3 Influence Coefficents

The influence coefficient matrices are $N \times N$ matrices outlined in boundary-element analysis of Chapter 3.1.2. The influence coefficients stated below are based on those of Lucey et al. (1997). For a full derivation see Lucey (1989). The sources are distributed at the centre of each panel with length, c, and angle between the panel and the horizontal, α.

The normal, tangential and perturbation influence coefficients are,

$$I_{im}^{N} = \frac{a_s}{4\pi} \ln \left(\frac{c_m^2 - 4ec_m + 4f}{c_m^2 + 4ec_m + 4f} \right) + \frac{a_c}{2\pi} \left(\tan^{-1} \left(\frac{2e + c_m}{2b} \right) - \tan^{-1} \left(\frac{2e - c_m}{2b} \right) \right), \tag{3.24}$$

$$I_{im}^{T} = \frac{a_s}{2\pi}\left(\tan^{-1}\left(\frac{2e+c_m}{2b}\right) - \tan^{-1}\left(\frac{2e-c_m}{2b}\right)\right) - \frac{a_c}{4\pi}\ln\left(\frac{c_m^2 - 4ec_, + 4f}{c_m^2 + 4ec_, + 4f}\right), \tag{3.25}$$

$$I_{im}^{\Phi} = -\frac{e}{4\pi}\ln\left(\frac{c_m^2 - 4ec_m + 4f}{c_m^2 + 4ec_m + 4f}\right) + \frac{c_m}{8\pi}\ln\left(\frac{\left(c_m^2 - 4ec_m + 4f\right)\left(c_m^2 + 4ec_m + 4f\right)}{16L^4}\right) - \frac{c_m}{2\pi} + \frac{b}{2\pi}\left(\tan^{-1}\left(\frac{2e+c_m}{2b}\right) - \tan^{-1}\left(\frac{2e-c_m}{2b}\right)\right), \tag{3.26}$$

respectively for $i \neq m$ where,

$$a_s = \sin\left(\alpha_i - \alpha_m\right), \tag{3.27a}$$

$$a_c = \cos\left(\alpha_i - \alpha_m\right), \tag{3.27b}$$

$$b = -\left(X_i - X_m\right)\sin\alpha_m + \left(Y_i - Y_m\right)\cos\alpha_m, \tag{3.27c}$$

$$e = \left(X_i - X_m\right)\cos\alpha_m + \left(Y_i - Y_m\right)\sin\alpha_m, \tag{3.27d}$$

$$f = \left(X_i - X_m\right)^2 + \left(Y_i - Y_m\right)^2, \tag{3.27e}$$

for panels with mass points (panel centres) given by coordinates (X, Y).

The influence of each panel on itself ($i = m$) is given by,

$$I_{ii}^{N} = \frac{1}{2}, \tag{3.28}$$

$$I_{ii}^{T} = 0, \tag{3.29}$$

$$I_{ii}^{\Phi} = \frac{c_m}{2\pi}\left(\ln\left(\frac{c_m}{2L}\right) - 1\right). \tag{3.30}$$

These influence coefficients are used in the fully nonlinear calculations of Chapter 5.1. By making the linear approximations that the sources lie on the undisturbed surface ($y = 0$) and that $\alpha = 0$, the linearised influence coefficients can be shown to reduce to,

$$\left[I^{N}\right] = \frac{1}{2}\left[I\right], \tag{3.31}$$

$$I_{im}^{T} = -\frac{1}{4\pi}\ln\left(\frac{\left(\delta x - 2\left(X_i - X_m\right)\right)^2}{\left(\delta x + 2\left(X_i - X_m\right)\right)^2}\right), \tag{3.32}$$

$$I_{im}^{\Phi} = \frac{1}{4\pi}\left\{(\delta x - 2(X_i - X_m))\ln\left|\frac{\delta x - 2(X_i - X_m)}{2L}\right| + (\delta x + 2(X_i - X_m))\ln\left|\frac{\delta x + 2(X_i - X_m)}{2L}\right| - 2\delta x\right\}, \tag{3.33}$$

where $[I]$ is the identity matrix and $\delta x = L/N_{\mathrm{f}}$. These linearised influence coefficients are used in the current chapter for linear analysis and in Chapter 4 for the non-modal analysis.

3.1.4 Theoretical Analysis

In order to complement and validate the foregoing numerical approach an extension of the open-flow analysis of Carpenter and Garrad (1986) of an infinitely long flexible plate with a uniformly distributed spring foundation is developed to account for the effect of the rigid upper wall of the channel. This type of flexible insert is chosen because the critical modes in its destabilisation can have much shorter wavelengths than the wall length, thus allowing its deformation to be approximated by a travelling wave with the form,

$$\eta = \eta_0 \exp\{ik(x - ct)\}, \tag{3.34}$$

with the flow-velocity perturbation written as,

$$\phi = \Phi(y)\exp\{ik(x - ct)\}, \tag{3.35}$$

where k is the wavenumber, c is the complex wave speed and η_0 is the amplitude of the boundary perturbation. Solving the Laplace Equation (3.4) gives,

$$\Phi(y) = A_1 \exp^{ky} + B_1 \exp^{-ky}, \tag{3.36}$$

with unknown constants A_1 and B_1. By enforcing the boundary conditions in Equations (3.6) and (3.7), A_1 and B_1 are found to be,

$$A_1 = \frac{\eta_0 i(U - c)}{1 - \exp^{2kH}}, \tag{3.37a}$$

$$B_1 = \frac{\eta_0 i(U - c)}{\exp^{-2kH} - 1}. \tag{3.37b}$$

Use of the Bernoulli equation, (3.5), applied to the streamline along $y = 0$ then yields the pressure perturbation,

$$-\Delta p = \rho_{\mathrm{f}} \eta_0 k \left(U - c\right)^2 \zeta \exp\{ik\left(x - ct\right)\}, \tag{3.38}$$

where ζ is a function of channel height defined by,

$$\zeta = \frac{1}{1 - \mathrm{e}^{-2kH}} - \frac{1}{1 - \mathrm{e}^{2kH}}, \tag{3.39}$$

that effectively accounts for the confinement effects of the channel as compared with an open flow for which $\zeta = 1$. Coupling this with the beam equation, (3.1), at $y = 0$ (assuming small/linear deflections) for a plate with no structural damping gives the following characteristic equation (dispersion relation) for the complex wave speed c,

$$\left(\rho_{\mathrm{f}} k\zeta + \rho_{\mathrm{m}} h k^2\right) c^2 - \left(2\rho_{\mathrm{f}} kU\zeta\right) c + \left(\rho_{\mathrm{f}} k\zeta U^2 - Bk^4 - K\right) = 0. \tag{3.40}$$

Following Carpenter and Garrad (1986), the onset of divergence instability occurs when the phase speed, c, first becomes zero as the flow speed is increased. Thus, the flow speed for divergence onset is that for which,

$$\rho_{\mathrm{f}} k\zeta U^2 - Bk^4 - K = 0, \tag{3.41}$$

and its minimum, or critical, value occurs for the wavenumber which satisfies,

$$\frac{\partial(U^2)}{\partial k} = 0, \tag{3.42}$$

where,

$$U^2 = \frac{Bk^4 + K}{\rho_{\mathrm{f}} k\zeta}. \tag{3.43}$$

This minimisation yields the critical wavenumber for divergence onset, k_{d}, and the critical flow speed for divergence is then given by,

$$U_{\mathrm{d}} = \left(\frac{Bk_{\mathrm{d}}^4 + K}{\rho_{\mathrm{f}} k_{\mathrm{d}} \zeta}\right)^{\frac{1}{2}}. \tag{3.44}$$

The critical wavenumber is therefore seen to depend not only on the structural parameters and fluid density but also on the channel height, H, through the function ζ defined by Equation (3.39).

By considering the function ζ, the asymptotic limits can be assessed. From Equation (3.39), $\zeta \to 1$ as $H \to \infty$ and this yields,

$$k_{\mathrm{d}} = \left(\frac{K}{3B}\right)^{\frac{1}{4}} \quad \text{and} \quad U_{\mathrm{d}} = 2\left(\frac{BK^3}{27\rho_{\mathrm{f}}^4}\right)^{\frac{1}{8}}, \tag{3.45a, b}$$

which recovers the results of Carpenter and Garrad (1986) for the open flow (Equation (2.13) of their paper).

At a higher flow speed, modal-coalescence is known to occur when the roots of Equation (3.40) are equal and so by setting the discriminant equal to zero, the critical speed for modal-coalescence flutter is derived as,

$$U_{\mathrm{m}} = \left(\frac{\left(Bk_{\mathrm{m}}^4 + K\right)\left(\rho_{\mathrm{f}}\zeta + \rho_{\mathrm{m}} h k_{\mathrm{m}}\right)}{\rho_{\mathrm{f}}\rho_{\mathrm{m}} h k_{\mathrm{m}}^2 \zeta}\right)^{\frac{1}{2}}, \tag{3.46}$$

for the critical wavenumber k_{m}. It can be shown that setting $k_{\mathrm{m}} = k_{\mathrm{d}}$ yields,

$$U_{\mathrm{m}} = U_{\mathrm{d}}\left(1 + \frac{\rho_{\mathrm{f}}\zeta}{\rho_{\mathrm{m}} h k_{\mathrm{d}}}\right)^{\frac{1}{2}}, \tag{3.47}$$

which again agrees with the open flow result of Carpenter and Garrad (1986) (Equation (2.14) in their paper) in the limit $H \to \infty$ that gives $\zeta \to 1$.

To assess the effect of the channel height in the limit of very narrow channels it is possible to show that $\zeta \to 1/(kH)$ as $H \to 0$, and this yields the divergence and modal-coalescence speeds as,

$$U_{\mathrm{d}} = \left(\frac{H}{\rho_{\mathrm{f}}}\left(Bk_{\mathrm{d}}^4 + K\right)\right)^{\frac{1}{2}} \tag{3.48a}$$

$$U_{\mathrm{m}} = \left(\frac{\left(Bk_{\mathrm{m}}^4 + K\right)\left(\rho_{\mathrm{f}} + \rho_{\mathrm{m}} h k_{\mathrm{m}}^2 H\right)}{\rho_{\mathrm{f}}\rho_{\mathrm{m}} h k_{\mathrm{m}}^2}\right)^{\frac{1}{2}}. \tag{3.48b}$$

In the results that follow, these analytical predictions and asymptotic forms are compared with the results of the state-space analysis for finite flexible inserts. However, the latter analysis does not clearly distinguish between divergence and modal coalescence for a spring-backed wall. As the flow speed increases the plate's behaviour shows a transition from divergence to modal coalescence. This type of gradual transition from divergence, as opposed to an explosive onset of flutter, was also found in the numerical simulations of Lucey and Carpenter (1992). It is therefore difficult to compare the foregoing analytical predictions for modal-coalescence flutter onset (Equations (3.46) and (3.48b)) with the results

of the state-space solution. Thus, only divergence onset for spring-backed flexible plates is considered because this instability yields the critical flow speed and is also shown to be a travelling-wave type of dynamic instability in Pitman and Lucey (2009).

3.2 Validation of the Open Flow Model

It is noted here that the analytical method has already been validated in Section 3.1.4 in the limit of $H \to \infty$ by comparison with the open flow results of Carpenter and Garrad (1986). For finite channel heights, validation by means of comparison with the results from the state-space method when applied to higher order plate types is presented in the results Section (3.3.1).

For the state-space method, the effect of the upper channel wall (the new aspect of this work) will also be demonstrated in the results section by means of comparison with experimental data (Weaver and Païdoussis, 1977) for plates of lower order mode in Section 3.3.1, and by comparison with other studies (Weaver and Païdoussis, 1977) and the analytical method for plates with a higher order mode shape in Section 3.3.1. The remainder of this chapter validates the correct implementation of the structural and fluid mechanics using the finite-difference and state-space methods.

3.2.1 Structural Mechanics

To validate the structural mechanics and finite-difference method, the eigenvectors calculated by the state-space method, when the fluid density is set to zero, can be compared with the in vacuo modes of form,

$$\eta = \eta_0 \sin\left(\frac{n\pi x}{L}\right), \tag{3.49}$$

where n is the mode number. Similarly, the imaginary part of the state-space eigenvalues, S_{I}, can be compared with the theoretical angular frequency of a plate in vacuo, S_0, which is well known to be,

$$S_0 = \left(\frac{n\pi}{L}\right)^2 \sqrt{\frac{B}{\rho_{\mathrm{m}} h}}. \tag{3.50}$$

By setting the fluid density to zero, the plate behaves as in vacuo, as all the fluid mechanics are neglected from the calculations.

The properties used to produce these results are: $L = 0.6$ m, $h = 0.0025$ m, $H = 0.6$ m, $\rho_{\mathrm{m}} = 2600$ kg/m^3, $B = 76.62$ N/m^2 and $\rho_{\mathrm{f}} = 0$ kg/m^3 and this gives a theoretical value of $S_0 = 94.13$ rad/s from Equation (3.50) when calculated for the first mode, $n = 1$.

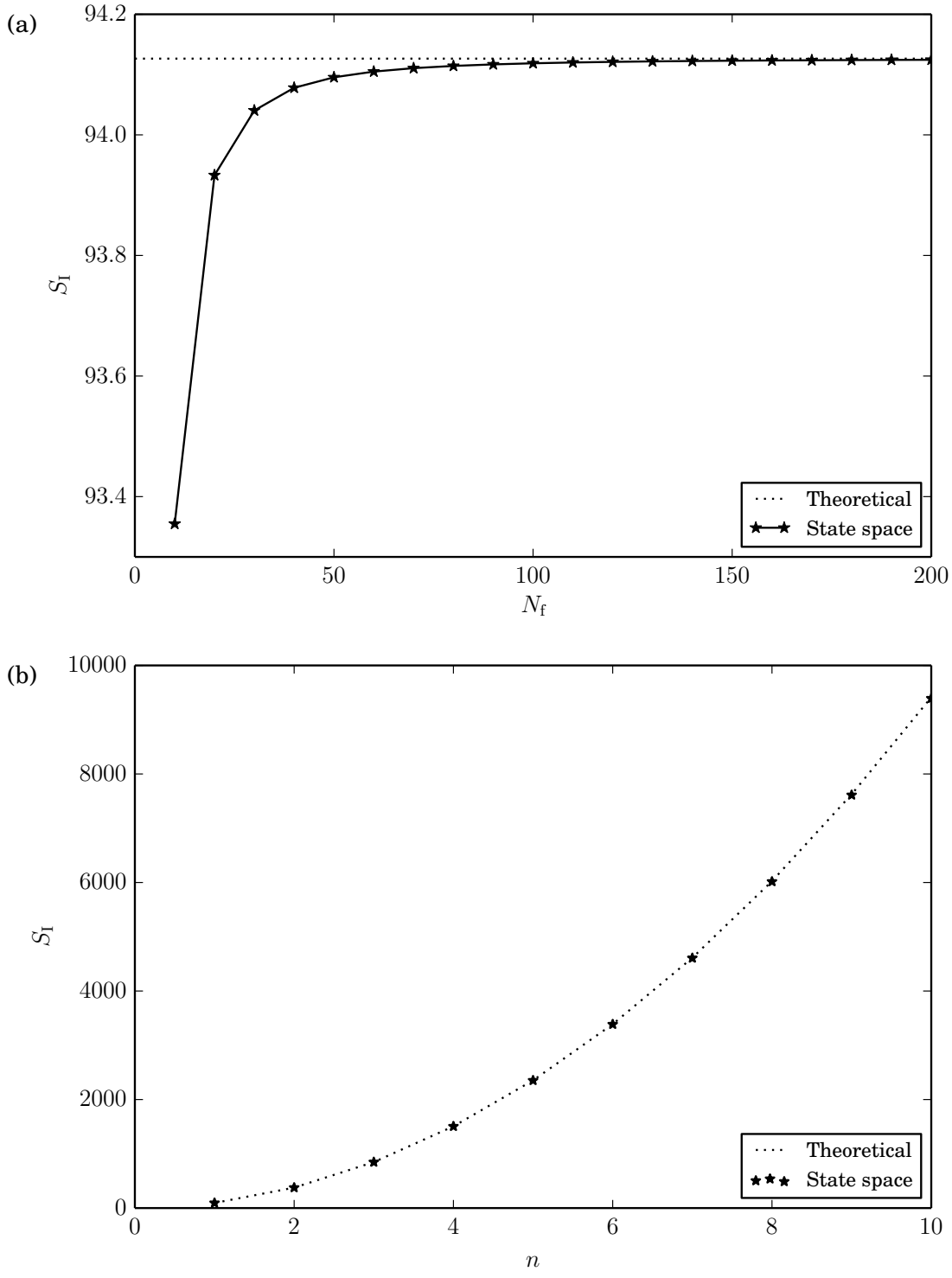

Figure 3.2: (a) Theoretical in vacuo frequency of the first mode, calculated from Equation (3.50) and the lowest imaginary eigenvalue calculated from the state-space method for different discretisations. (b) Theoretical in vacuo frequency calculated from Equation (3.50) for the first ten modes and the lowest ten imaginary eigenvalues calculated from the state-space method when $N_{\mathrm{f}} = 200$.

Figure 3.2 (a) shows the theoretical value of the first mode frequency, $S_0 = 94.13$ rad/s, plotted as a dotted line. Also plotted is the lowest (first mode) imaginary part of the eigenvalues found from the state-space method, S_I. When $N_\mathrm{f} = 10$ the percentage error of the state space method is only 0.82% indicating that in the absence of a fluid, this low level of discretisation is sufficiently accurate. The method becomes more accurate as N_f is increased, with a percentage error of 0.0021% when $N_\mathrm{f} = 200$.

Figure 3.2 (b) plots Equation (3.50) as it varies with the mode, n. Also shown on Figure 3.2 (b) is the imaginary part of the lowest ten eigenvalues calculated from the state space method when $N_\mathrm{f} = 200$. This demonstrates that the state-space method for a plate in vacuo is sufficiently accurate for up to mode ten when $N_\mathrm{f} = 200$. Although it appears that there is no change in the accuracy, the percentage error between the state space method and theoretical equation increases from 0.0021% when $n = 1$ to 0.21% when $n = 10$. This indicates that for a plate displaying a higher order mode shape, the discretisation should be increased in order to maintain the same level of accuracy.

The data presented here clearly shows that the structural mechanics is accurately modelled by the state-space application of the finite-difference method that is used in this work.

3.2.2 State-Space Method

Using the state space method to predict divergence and modal-coalescence onset for a flexible plate in an open flow is well established and here a simple elastic plate is considered to validate the application of the fluid mechanics. Validation of different plate types (including plates with structural damping and spring-backing) in an open flow will be presented in Section 3.3 along with an investigation into the effect of the channel wall.

To provide a convenient comparison with similar studies, the results are presented using a non-dimensional scheme based upon L and L/U as the characteristic length and time scales. The system behaviour can then be summarised by

its dependence upon three non-dimensional parameters, namely, the mass ratio

$$\mu = \frac{\rho_{\mathrm{f}} L}{\rho_{\mathrm{m}} h}, \tag{3.51}$$

and the non-dimensional stiffness ratio,

$$\Lambda^{\mathrm{F}} = \frac{\rho_{\mathrm{f}} U^2 L^3}{B}, \qquad \Lambda^{\mathrm{M}} = \frac{\rho_{\mathrm{f}} U^2 L}{T}, \tag{3.52a, b}$$

defined respectively for simple flexible plates and tensioned membranes, and the non-dimensional channel height H/L. Note that the inclusion of structural damping introduces a further control parameter to the base system. For the spring-backed flexible plate, or compliant wall, L no longer represents the characteristic length scale and therefore appropriate alternatives are found and discussed in Section 3.3.1.

Because the time-scale L/U is inappropriate for plate vibrations at zero flow speed, the non-dimensional frequency, $S' = S/S_0$, used in the results is based upon the angular oscillation frequency of the fundamental mode of the plate in vacuo, given by Equation (3.50).

The eigenvalue solution shown in Figure 3.3 shows excellent agreement with the previous investigations of Pitman and Lucey (2009) (Figure 3 of their paper) and Tan et al. (2013) (Figure 4 of their paper) which were themselves validated against a Galerkin analysis. The divergence-onset prediction of $\Lambda^{\mathrm{F}} = 40$ (for $N_{\mathrm{f}} = 200$) also agrees with the findings of, for example, Weaver and Unny (1970), Lucey and Carpenter (1992), Garrad and Carpenter (1982), and Tan et al. (2013) which use Galerkin, analytical, numerical simulations and eigenvalue methods respectively, thereby validating the present computational modelling and its implementation.

Figure 3.3 also shows the effect of the discretisation level on the eigenvalue solution. It can be seen that as $N_{\mathrm{f}} \to \infty$ the solution converges. For the simple plates and tensioned membranes that are typically characterised by a low-order mode shape, $N_{\mathrm{f}} = 200$ is used throughout, while the spring-backed (compliant wall) requires a greater discretisation due to the higher-order mode shape of the wall. For spring stiffnesses $K = 3.68 \times 10^6$, 3.68×10^7 and 3.68×10^8 N/m^3 it is found that $N_{\mathrm{f}} = 480$, 800 and 1420 respectively, are sufficient to achieve the same

level of numerical convergence based on the critical mode at which divergence occurs.

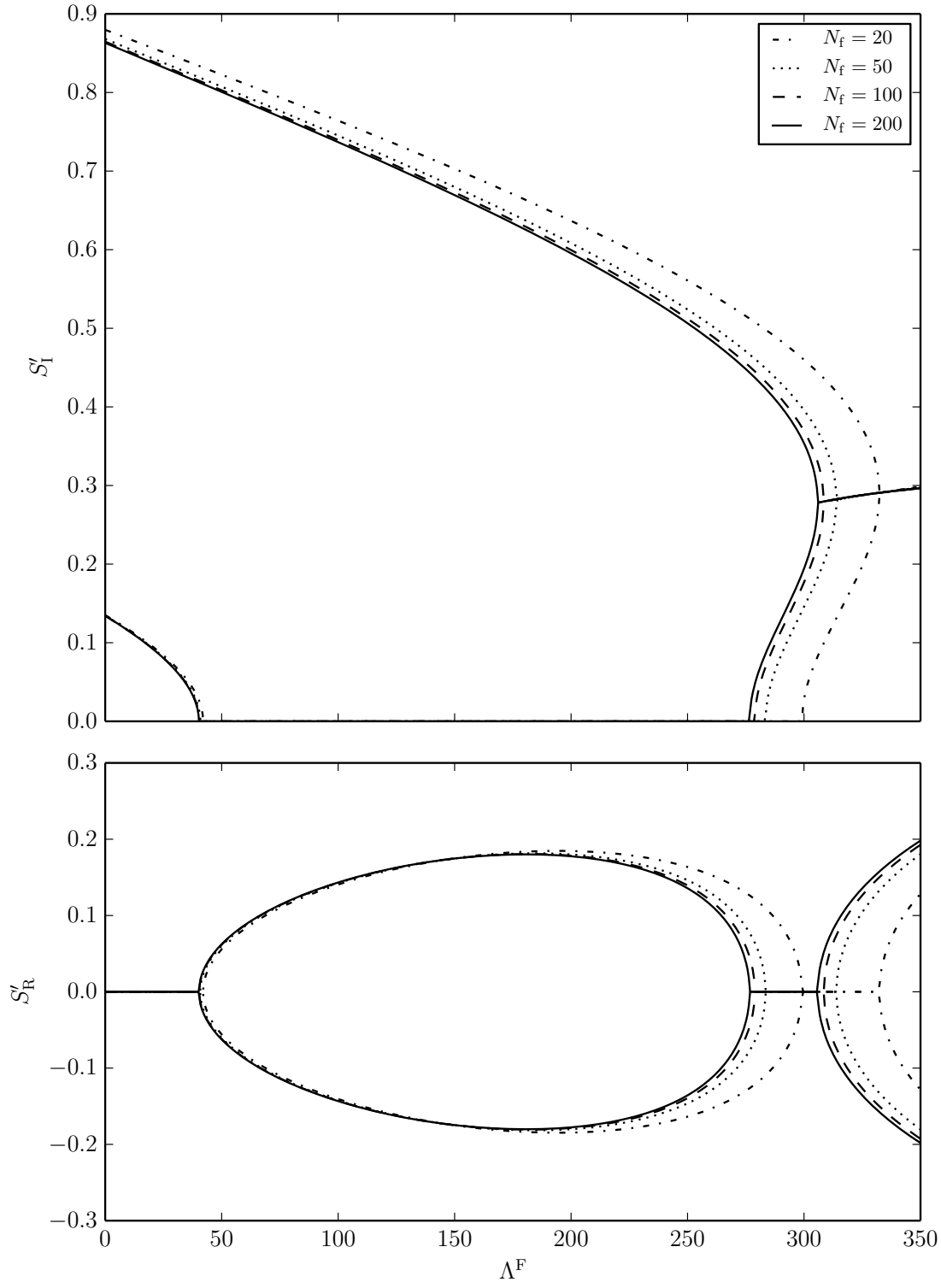

Figure 3.3: Variation of the real (growth/decay) and imaginary (oscillatory) parts of the first two eigenvalues with stiffness ratio (non-dimensional flow speed) at different discretisations when $H/L = \infty$.

3.3 Results

Before progressing, comment is made on the location of the fluid entry and exit boundary conditions. Assessment of the effect of the length chosen for rigid-channel walls up- and down-stream of the flexible insert as seen in Figure 1.2 (a) shows that for wide channels ($H/L > 1.5$) and very narrow channels ($H/L < 0.1$, such as when the spring-backed flexible plate is being considered) changing L_r does not change the eigenvalue solution and therefore when modelling a spring-backed flexible plate we use $L_\mathrm{r} = 0$. For all other channel heights, as when considering a simple elastic plate, a damped plate and a tensioned membrane, $L_\mathrm{r} = 2L$ is sufficiently large for the up- and down-stream rigid walls of the channel not to influence the numerical evaluations to within less than 1%. With the flexible insert modelled by N_f panels (or equidistantly spaced collocation points), the upper rigid wall therefore comprises $5N_\mathrm{f}$ panels so that the system has a total of $N = 10N_\mathrm{f}$ panels. However, for the spring-backed plate the system has a total of $N = 2N_\mathrm{f}$ panels.

3.3.1 Single Sided Channel

Simple Elastic Plate

Herein, the flexible insert studied has the structural dynamics of a flexible plate that, for example, could correspond to a thin aluminium panel. Illustrative dimensional properties used in this section are $h = 0.0025$ m, $\rho_\mathrm{m} = 2600$ kg/m^3, $B = 76.62$ Nm, $d = 0$ Ns/m^3, $K = 0$ N/m^3, $L = 0.6$ m, $L_\mathrm{r} = 1.2$ m and $T = 0$ N/m. A dense fluid such as water is considered with fluid density $\rho_\mathrm{f} = 1000$ kg/m^3. The combination of solid and fluid densities along with the plate geometry yields the mass ratio $\mu = 92.3$ used to generate the non-dimensional results presented in Figures 3.4 and 3.5. The variation with the stiffness ratio (non-dimensional flow speed) of the real and imaginary parts of the eigenvalues for two contrasting channel heights, $H/L = 2$ and 0.1, are shown in Figure 3.4. The real part of the eigenvalue determines the growth/decay rate of plate deflections and the imaginary part determines the oscillation frequency of each mode. Each complex eigenvalue, S, has a complex conjugate but only the positive imaginary

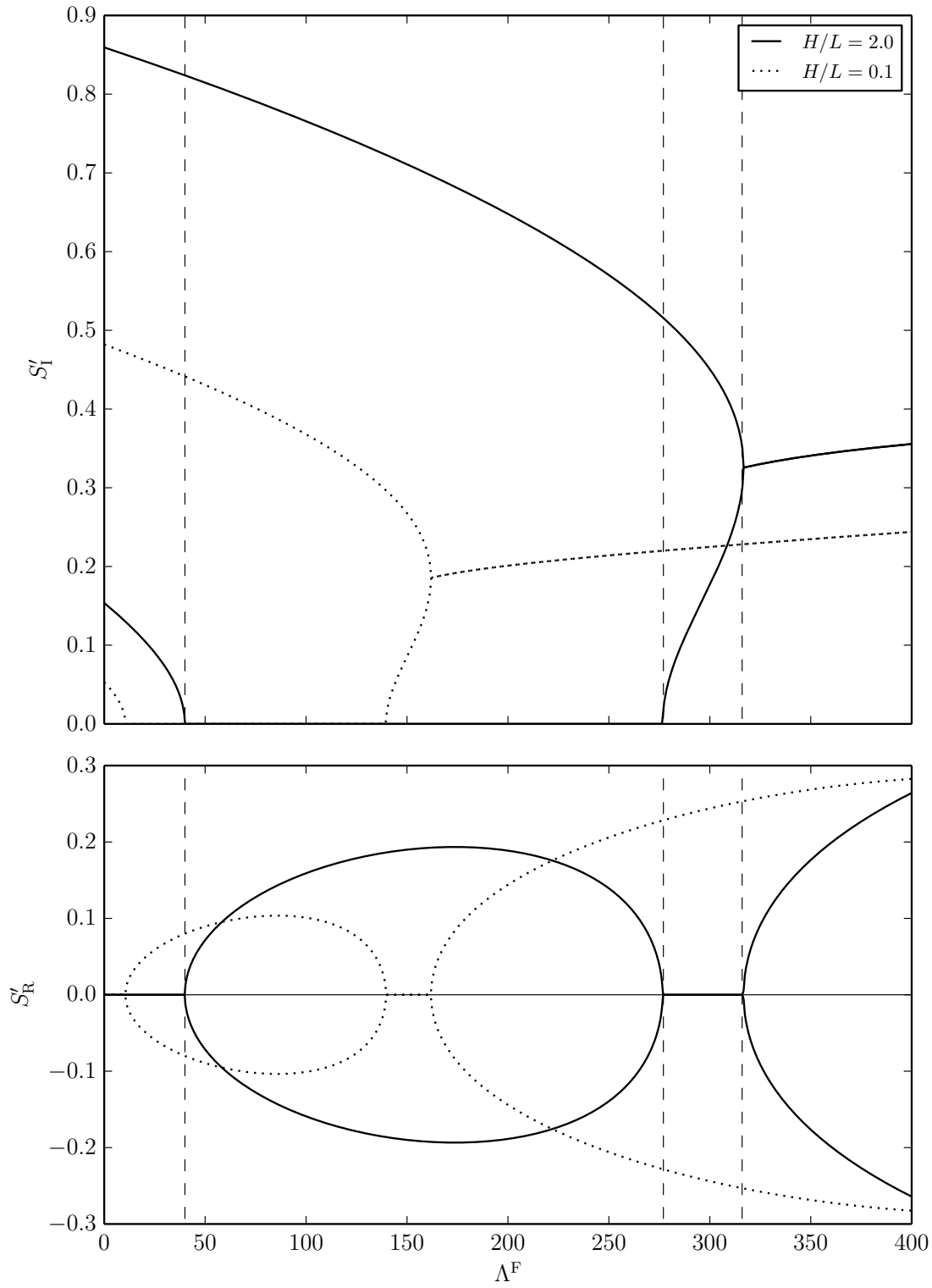

Figure 3.4: Variation of the real (growth/decay) and imaginary (oscillatory) parts of the first two eigenvalues with stiffness ratio (non-dimensional flow speed) for two non-dimensional channel heights for mass ratio $\mu = 92.3$. The vertical dashed lines indicate divergence onset, divergence recovery and flutter onset for the case $H/L = 2$.

values are shown in this figure (and for the remainder of results presented) as a negative oscillation frequency has no physical interpretation in this work. Note that only the lowest two eigenvalues are plotted in this figure although all $2N_{\mathrm{f}}$ eigenvalues of the complete fluid-structure system are calculated.

In Figure 3.4, there are four zones of Λ^{F} (for each channel height) that correspond to four distinct types of plate behaviour (Pitman and Lucey, 2009). These zones are delineated here by vertical dashed lines for the $H/L = 2$ case. The first is the pre-divergence zone, when the eigenvalue of the fundamental mode has an imaginary but no real part, hence the plate displays neutrally stable oscillatory motion where the plate is oscillating but no growth occurs. When the eigenvalue first has a real part, divergence instability sets in and the plate deflection amplifies, with no oscillation. For higher Λ^{F} the real part again becomes zero returning the plate to the neutrally stable oscillatory motion - this range of flow speeds is known as divergence recovery. The final type of behaviour with increased Λ^{F} is initiated by the coalescence of the fundamental and second modes and the plate undergoes a flutter-type motion consisting of both growth and oscillation. For the case $H/L = 2$, Figure 3.4 shows that the transitions - called divergence onset, divergence recovery and flutter onset - between these four zones occur at $\Lambda^{\mathrm{F}} = 40$, 277 and 316 respectively. For the results at $H/L = 2$ the eigenvalue solution agrees very closely with that for the open-flow shown in Figure 3.3; thus after $H/L = 2$, upper-wall effects have become negligible.

The present linear theory predicts the aforementioned zones of wall behaviour that would occur if the applied flow velocity could be established instantaneously. However, in a physical situation the flow velocity would be increased from zero over a finite period of time. Thus, as soon as the flow velocity exceeds that of divergence onset, the wall deformation would grow to reach large amplitudes (for example, see Lucey et al. (1997)), thereby violating the linear assumptions of the present modelling. However, if the flow velocity were increased rapidly from zero so that nonlinear divergence instability did not have sufficient time to become established, then the phenomena of divergence recovery and modal-coalescence flutter for linear disturbances could be realised.

The continuous variations with channel height of divergence onset, divergence

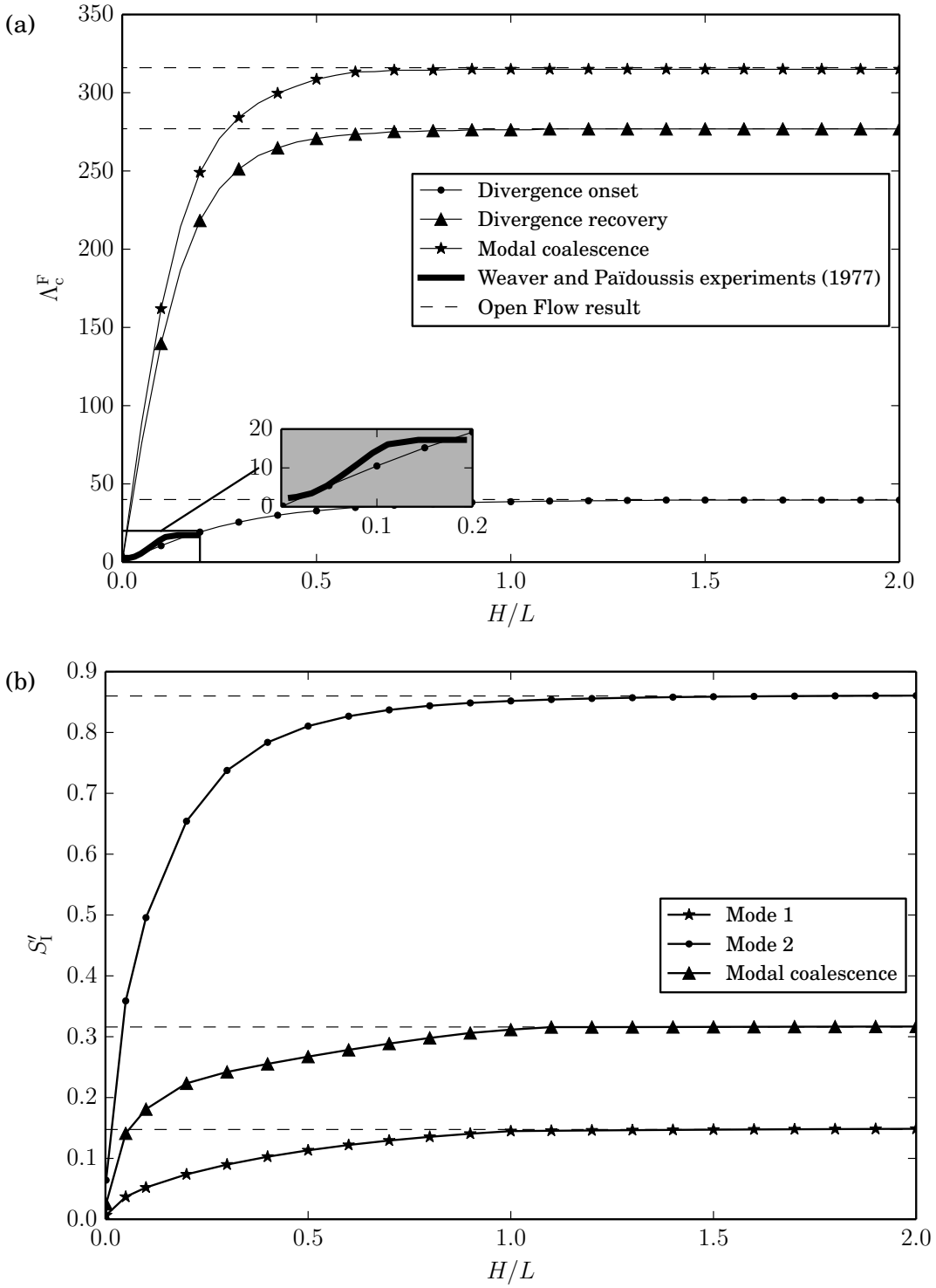

Figure 3.5: The effect of channel height on the FSI of a flexible plate for $\mu = 92.3$: (a) Variation of stiffness ratio values at instability onset or recovery with channel height, and (b) The variation with channel height of Mode 1 and Mode 2 oscillation frequency at zero flow speed and modal-coalescence flutter frequency at onset. In both (a) and (b), the dashed lines indicate values for the equivalent open flow.

recovery and flutter-onset stiffness ratio, Λ_c^F (threshold flow speed for a given flexible plate and fluid), are presented in Figure 3.5 (a). The horizontal dashed lines indicate corresponding values for an open flow, i.e. with $H = \infty$. In the asymptotic limit of increasing channel height, the present results for channel flow approach those for an open flow and that beyond $H/L = 1$ the upper channel wall has effectively ceased to have an effect on the plate's stability characteristics. Below $H/L = 1$, decreasing the channel height monotonically reduces Λ^F for divergence onset. Divergence first occurs at the flow speed for which the plate's restorative forces exactly balance the hydrodynamic stiffness, the first term on the right-hand side of Equation (3.11). Clearly, the magnitude of the hydrodynamic stiffness has been increased by reducing the channel height because a lower critical speed for the instability ensues. At first sight, it might appear that the increase to the hydrodynamic stiffness is caused by the plate deformation changing the effective value of U in Equation (3.11). However, this would be a nonlinear effect because it implies a change to the mean state of the system. In the present linear analysis, the increase to the magnitude of the hydrodynamic stiffness is caused by the effect of the upper channel wall which increases (decreases) the gradient, in the y-direction, of streamline curvature for a plate deformation into (out of) the channel. This occurs because the upper boundary, that has zero curvature, must always remain a streamline of the perturbed flow as it surmounts the deformation of the flexible insert in the lower channel wall.

Weaver and Païdoussis (1977) theoretically analysed a channel-flow system for inviscid flow with both walls flexible using both a Galerkin approach, where each wall was on periodic supports, and a travelling-wave approach weighted for transverse curvature. In each analysis they considered the two cases of walls moving in phase (sinuous) and 180° out of phase (varicose); the latter is closest to the system studied in the present work because it involves a variation to streamline curvature across the channel. Using the Galerkin analysis, Weaver and Païdoussis (1977) found that reducing the channel height caused a maximum reduction in the critical flow velocity for divergence of 29%, which corresponds to approximately a 54% decrease in Λ^F. This finding differs from the results presented herein where the critical non-dimensional flow speed for divergence

reduces to zero as $H/L \to 0$. However, for this limit, our results agree with those of the travelling-wave analysis of Weaver and Païdoussis (1977). Weaver and Païdoussis (1977) also show that above $H/L = 1$, in both of their theoretical models, the critical flow velocity for divergence is the same as for the open-flow case; a similar value for this threshold is demonstrated in the results of Figure 3.5 (a).

Also included as an insert in Figure 3.5 (a) are experimental data reported by Weaver and Païdoussis (1977) in Figure 8 of their paper. A flattened tube was constricted, effectively creating flow between parallel flexible walls, and the flow velocity at which a flapping instability occurred, associated with divergence as opposed to flutter, was recorded for various constrictions. A best-fit line of their results was converted into the non-dimensional scheme given by Equations (3.51) and (3.52)a by setting $H = 0.5b$ where b was the gap between their surfaces - because they considered two flexible surfaces instead of just one - and setting $L = 0.5\lambda$ where λ was the observed wavelength of the flapping. Good agreement is found between the predictions presented here and these experimental results for small H/L.

Figure 3.4 (b) also shows how channel height affects further features of the FSI system. Reducing the channel height decreases the frequency and growth/decay rate at a given flow speed. At zero stiffness ratio (zero flow speed) a lower channel height results in lower oscillation frequencies for both the fundamental and second mode, implying a higher fluid inertia, the fourth term on the right-hand side of Equation (3.11). This is due to the additional y-constraint on the decay of fluid perturbation imposed by the upper channel wall. Thus, for narrow channels, fluid perturbations due to the flexible-plate motion extend a significant distance upstream and downstream of the moving-wall section as reflected by the need to model the rigid upstream and downstream regions, described earlier. A further consequence is that reducing the channel height reduces the initial frequency difference, at $\Lambda^{\mathrm{F}} = 0$, between the fundamental and second modes. Modal-coalescence then occurs at a lower value of Λ^{F} and the size of the static divergence loop becomes smaller. Thus, while reducing the channel height leads to a reduction in the critical flow speed for divergence onset, beyond that threshold

both the range of flow speeds over which divergence occurs and its growth rate are reduced. However, the more violent flutter instability beyond divergence sets in at a lower flow speed and frequency.

The effect, as a continuous variation, of the upper channel-wall height on the first and second mode frequency at zero flow speed is shown in Figure 3.5 (b) along with the frequency at which modal-coalescence occurs. These results suggest that channel-height may have a significant effect on transient growth within the system through non-normality because Coppola and de Luca (2010) show that the frequency spacing between the lowest two modes is directly linked to the beating frequency of transient growth; this will be investigated in Chapter 4.

Damped Plate

The effect of including structural damping in the system is now considered. For simplicity, a dashpot-type damping, seen in Equation (3.1), with $d = 7500$ Ns/m^3 is used and the remaining system parameters are the same as in Section 3.3.1. This value is chosen to facilitate appropriate comparison with the open-flow results presented in Pitman and Lucey (2009) and its value represents an amplitude attenuation of 50% per cycle of the fundamental in vacuo plate mode.

Figure 3.6 shows the effect of including structural damping in the system that yielded Figure 3.4 (a). As would be expected, in the pre-divergence regime of stiffness ratio, the effect of structural damping is to attenuate the modes that were neutrally stable for the elastic plate. Turning to the range of stiffness ratio that yields instability, it is evident that the inclusion of structural damping both increases the size of the divergence loop and rotates it anticlockwise about the $S_{\mathrm{R}} = 0$ axis. This occurs because the dashpot-type damping exercises a greater effect at the higher modal frequencies that are obtained at lower values of Λ^{F}. However, the combination of these two effects upon the divergence loop is such that for each channel height the divergence-onset stiffness ratio remains the same as for the plate with no damping; this is most evident for the case $H/L = 2$ in Figure 3.4 (a) for which the divergence-onset threshold has been marked with the dashed line $\Lambda^{\mathrm{F}} = 40$, the same threshold shown in Figure 3.4 (a). This is

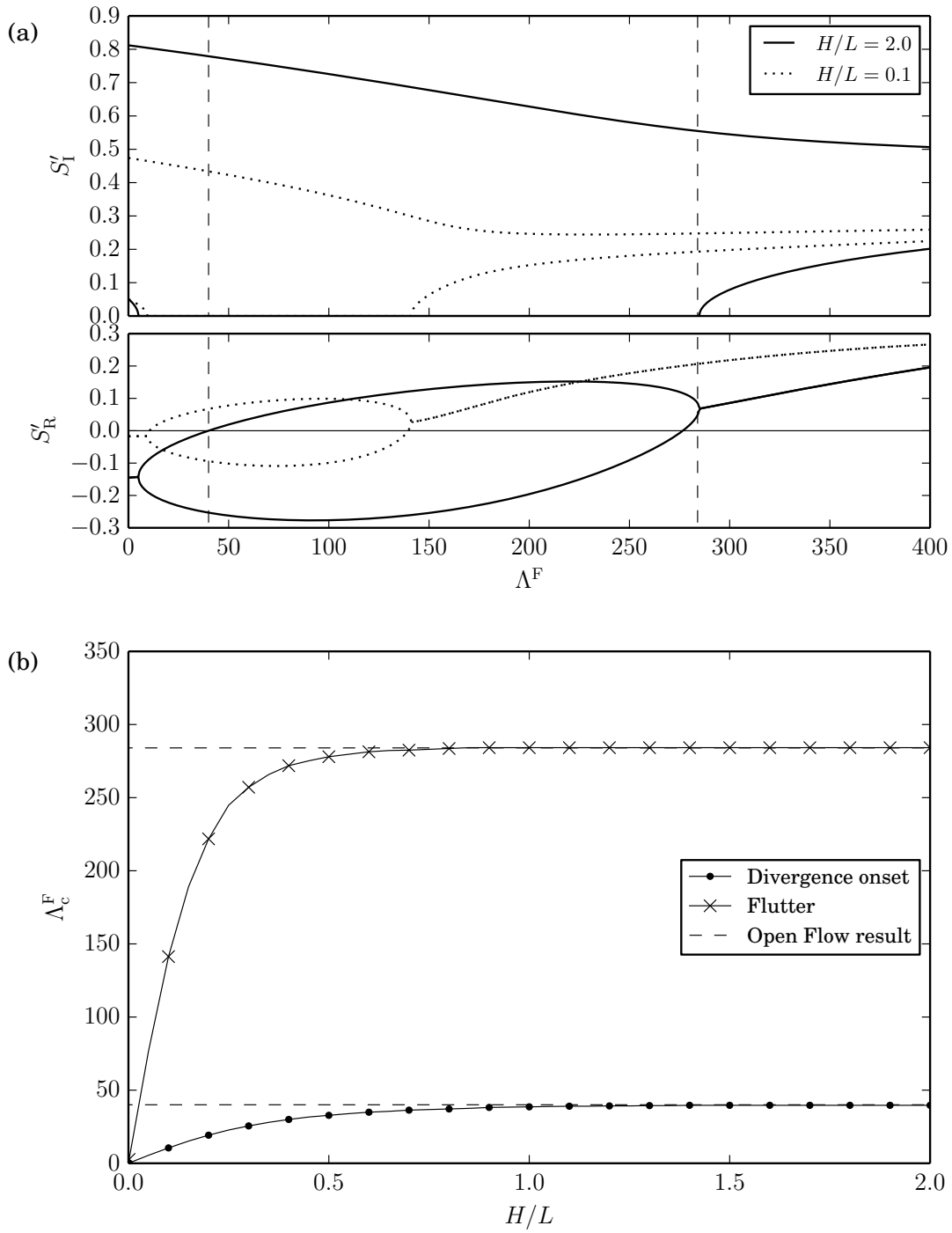

Figure 3.6: The effect of channel height on the stability of a structurally damped plate with mass ratio $\mu = 92.3$: (a) Variation of the real (growth/decay) and imaginary (oscillatory) parts of the first two eigenmodes with stiffness ratio (non-dimensional flow speed) for two non-dimensional channel heights; the vertical dashed lines indicate divergence and flutter onset for the case $H/L = 2$, and (b) Variation of the stiffness ratio values at instability onset or recovery with channel height; the dashed lines indicate values for the equivalent open flow.

to be expected because divergence onset occurs as a static phenomenon and the absence of motion means that structural damping does not play a part in its determination. Thus, the continuous variation of divergence-onset stiffness ratio with channel height, presented in Figure 3.6 (b) is identical to that seen in Figure 3.5 (a).

At post-divergence stiffness ratios structural damping exercises significant changes in the morphology of the eigenvalue solution that are similar to those found by Pitman and Lucey (2009) for the open-flow case. Firstly, there is no divergence-recovery zone, because the real parts of the fundamental and second modes are no longer symmetrical about $S_{\mathrm{R}} = 0$. Secondly, instead of a distinct point at which coalescence of the oscillatory-part of the frequency occurs, there is now a gradual transition in the unstable behaviour of the plate from divergence to flutter. The same modification (as compared with that for an elastic plate) to the eigenvalue solution morphology is also found when very low levels of damping are included. These effects, and the relationship between divergence and flutter, were demonstrated and discussed in the numerical work of Lucey and Carpenter (1992).

For the $H/L = 2.0$ case, the channel is sufficiently wide enough that the upper channel wall has no effect on the eigenvalue solution and the results in Figure 3.6 (a) agree with the open flow results of Pitman and Lucey (2009), indicating that the inclusion of structural damping has been correctly implemented. Figure 3.6 (b) gives a complete data set for the stability bounds of a damped plate as they vary with H/L.

Effect of Mass Ratio

The results for the simple elastic plate and structurally damped plate pertain to the mass ratio $\mu = 92.3$. Attention is now turned to the effect of channel height on the system behaviour for two lower values of mass ratio, $\mu = 9.23$ and $\mu = 0.923$. The physical data used is as for the simple elastic plate but with the fluid density changed to $\rho_{\mathrm{f}} = 100$ kg/m^3 and $\rho_{\mathrm{f}} = 1$ kg/m^3; the latter case closely represents air flow past an aluminium plate.

Figure 3.7 (a) shows the eigenvalue solutions at a channel height $H/L = 0.1$

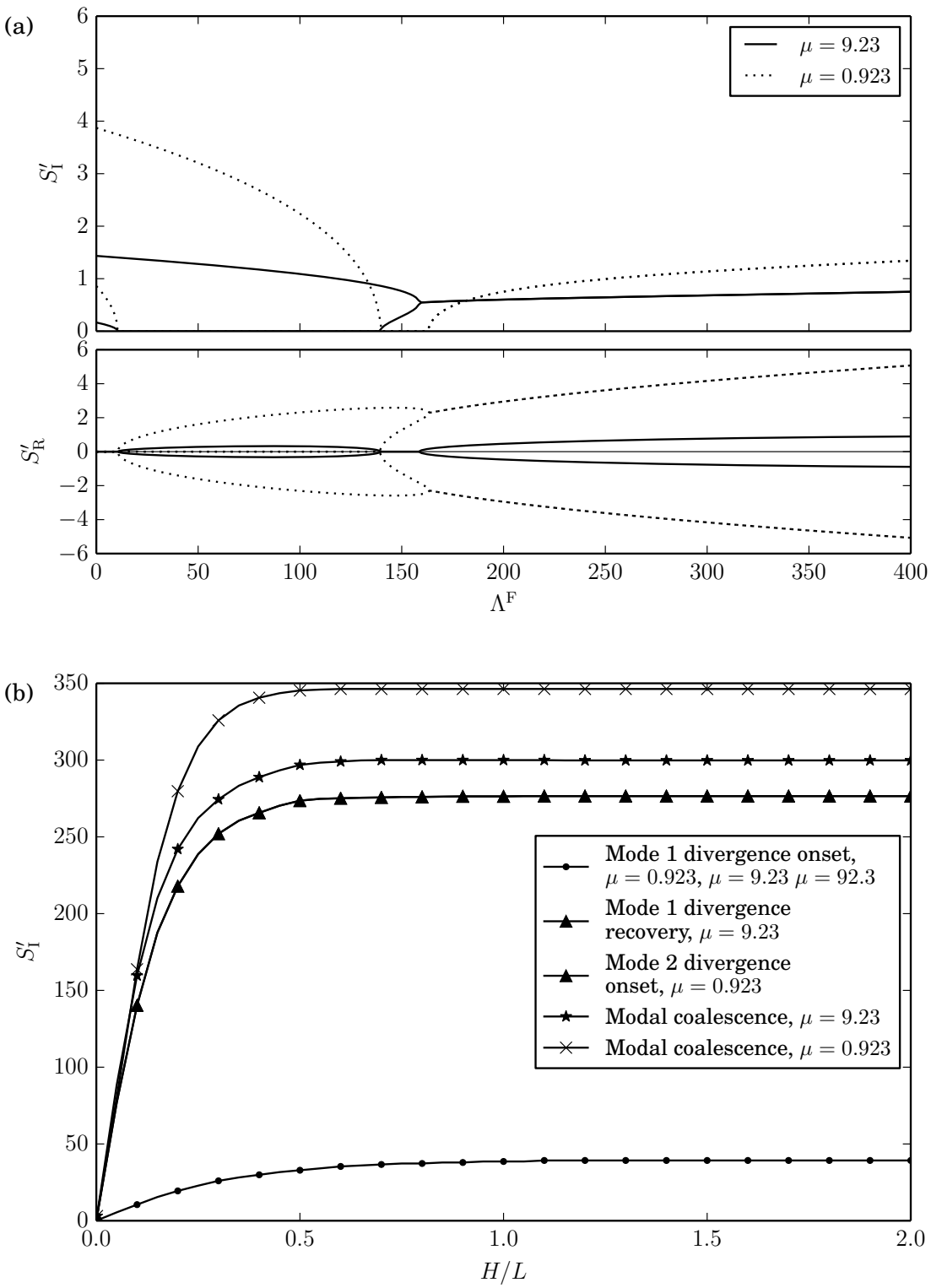

Figure 3.7: The effect of channel height on the stability of an elastic flexible plate for different mass ratios, μ: (a) Real and imaginary parts of the first two eigenvalues as a function of stiffness ratio (non-dimensional flow speed) at $H/L = 0.1$, and (b) Variation of stiffness ratio values at instability onset or recovery with channel height.

for each of $\mu = 9.23$ and 0.923. For $\mu = 9.23$ the solution morphology is seen to be the same as that in Figure 3.4 (a). The continuous variation of divergence-onset, divergence recovery and flutter-onset threshold values, Λ_c^F, with channel height are presented in Figure 3.7 (b) and are seen to follow very similar trends to the corresponding results for an undamped plate with $\mu = 92.3$ in Figure 3.5 (a). This finding agrees with Weaver and Païdoussis (1977) who concluded that the overall effect of the upper-channel wall proximity is largely unchanged by the mass ratio.

In contrast, for the mass ratio $\mu = 0.923$ in Figure 3.7 (a), a change to solution morphology has occurred. While the critical mode continues to be Mode-1 divergence with its onset stiffness ratio unchanged by mass ratio for a given channel height (since the instability is static exactly at onset) divergence recovery does not occur with increasing Λ^F, but instead Mode-2 divergence occurs and, with further increases, the two divergence modes coalesce to give flutter. The quantitative summary of the respective threshold values as they vary with channel height is presented in Figure 3.7 (b). This different sequence of instability transitions has been presented and its physical causes explained in Tan et al. (2013) for the corresponding open-flow configuration. What can be concluded from the new results of the present paper is that reducing the channel height does not modify the special solution morphology that applies at very low mass ratios and that for sufficiently wide channels ($H/L > 1$), the system behaves like the open flow.

Tensioned Membrane

To complete the investigation of flexible inserts comprising a single structural component, for which the lowest-order modes of deformation based on insert length give the critical values at destabilisation, a tensioned elastic membrane is considered. The system parameters are the same as for the simple elastic plate but with the flexural rigidity set to zero, $B = 0$ Nm and a tension of $T = 10000$ N/m applied. The system has the same mass ratio as for the simple elastic plate, that is $\mu = 92.3$. This type of insert has more relevance to applications in biomechanics than the preceding flexible-plate systems.

Figure 3.8 (a) displays the dependence of system eigenvalues on the stiffness

ratio (non-dimensional flow speed), Λ^{M}, defined using the membrane tension as seen in Equation (3.52b). The frequencies are now non-dimensionalised by the theoretical angular oscillation frequency of the fundamental mode of the membrane in vacuo,

$$S_0 = \left(\frac{\pi}{L}\right)\sqrt{\frac{T}{\rho_{\mathrm{m}} h}}. \tag{3.53}$$

The eigenvalue solution is qualitatively similar to that of the simple elastic plate, the physical interpretation of which, discussed therein, carries across to the phenomenology of the tensioned membrane. Although divergence, divergence recovery and flutter now occur at much lower values of the stiffness ratio, the dimensional flow speeds at which instabilities set in is within the same order of magnitude for the physical data given, when compared with the simple elastic plate.

The interaction of a tensioned membrane with viscous channel flow has received significant attention. Studies such as those of Luo and Pedley (1996), Luo and Pedley (2000), Huang (2001) and Jensen and Heil (2003) model unsteady laminar flow and (with the exception of Huang (2001)) large amplitude deformations. Therefore, direct comparison with the present results that use ideal flow can only be at a very broad level. What the two types of system are seen to have in common is that reductions to the membrane tension - that increase the value Λ^{M} in the present work - cause the onset of instability to occur at a lower flow speed or Reynolds number. In studies of viscous flow, the channel height determines the Reynolds number and thus its reduction would be stabilising because the overall balance between inertial forces and viscous forces changes in favour of the latter. In the present system the opposite is true because the destabilising inertial forces are intensified by reductions to the channel height with no ameliorating viscous effects. This effect is summarised in Figure 3.8 (b). It is noted that the absence of viscous effects in the present modelling renders the results non-physical for extremely low values of H/L. As a landmark, below $H/L = 0.003$ the dimensional data that is used here would yield Reynolds numbers in the laminar range of flow speeds, when using the kinematic viscosity of water at 20°C and the flow speed at divergence onset as the characteristic speed; this limitation also applies to the flexible-plate cases analysed in the previous results.

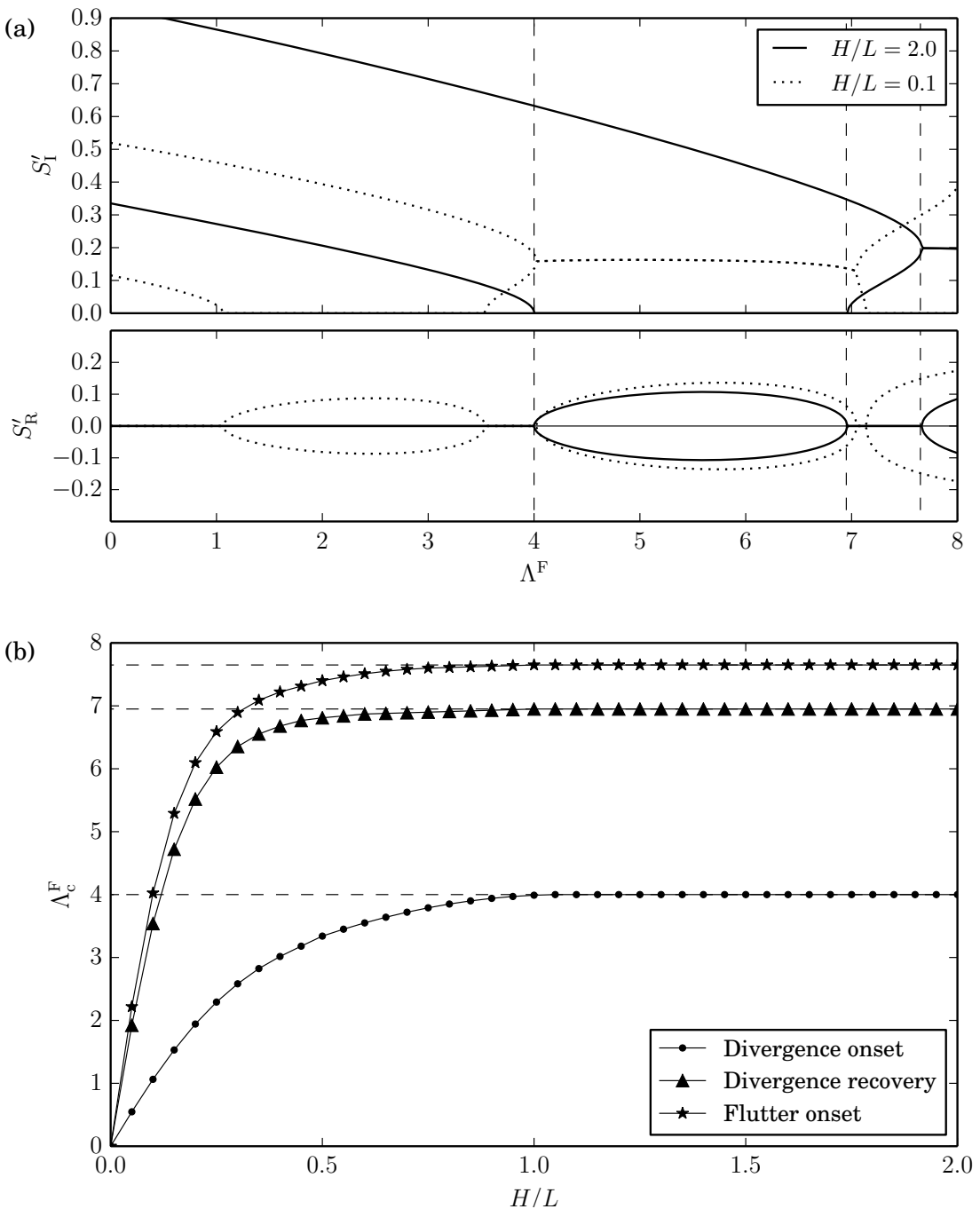

Figure 3.8: The effect of channel height on the stability of a tensioned membrane with mass ratio $\mu = 92.3$: (a) Variation of the real (growth/decay) and imaginary (oscillatory) parts of the first two eigenvalues with stiffness ratio (non-dimensional flow speed) for two non-dimensional channel heights; the vertical dashed lines indicate divergence onset, divergence recovery and flutter onset for the case $H/L = 2$, and (b) Variation of stiffness ratio values at instability onset or recovery with channel height; the dashed lines indicate values for the equivalent open flow.

Finally, in common with the flexible-plate results of Figure 3.4, the effects of channel height become insignificant for H/L greater than 1, beyond which the system behaves identically to that of a tensioned membrane subjected to an open-flow.

Spring-Backed Flexible Plate

The stability of a flexible plate supported by a uniformly distributed spring foundation is now considered. The introduction of a further structural component - the spring backing - creates significantly different stability characteristics because, for example, divergence onset is now determined by the combination of plate flexure, spring stiffness and the hydrodynamic-stiffness fluid loading. In particular, it is no longer the low-order modes having wavelengths of the order of the plate length that are the first to be destabilised as found for the inserts without spring-backing. Accordingly, the plate length, L, is not a suitable characteristic length for the FSI system and the following non-dimensional scheme, based upon a local characteristic length ($\rho_{\mathrm{m}}h/\rho_{\mathrm{f}}$), is introduced following Lucey and Peake (2003) wherein,

$$H' = \frac{H\rho_{\mathrm{f}}}{\rho_{\mathrm{m}}h}, \qquad U' = \frac{U\left(\rho_{\mathrm{m}}h\right)^{3/2}}{\rho_{\mathrm{f}}B^{1/2}} \qquad \text{and} \qquad K' = \frac{K\left(\rho_{\mathrm{m}}h\right)^{4}}{B\rho_{\mathrm{f}}^{4}}. \qquad (3.54\text{a, b, c})$$

Thus, Equations (3.54)a and b replace the control parameters that are the mass ratio, μ, and stiffness ratio, Λ^{F}, defined respectively by Equations (3.51) and (3.52), while the spring foundation introduces the additional control parameter, K'. The length of the flexible insert, L, contributes the further control parameter, $L' = \left(L\rho_{\mathrm{f}}\right) / \left(\rho_{\mathrm{m}}h\right)$, but it will be seen this has only a marginal influence on system response for the cases studied herein where the wavelength of the critical mode is much shorter than the panel length, a situation promoted by increases either to insert length or the stiffness of the spring foundation.

The system parameters used here are $h = 0.01$ m, $\rho_{\mathrm{m}} = 852$ kg/m^3, $B = 0.0444$ Nm, $d = 0$ Ns/m^3, $L = 0.6$ m, $L_{\mathrm{r}} = 0$ m, $T = 0$ N/m and $\rho_{\mathrm{f}} = 1000$ kg/m^3, with spring-backing of strengths $K = 3.68 \times 10^6$ N/m^3, $K = 3.68 \times 10^7$ N/m^3 and $K = 3.68 \times 10^8$ N/m^3 considered. The illustrative physical data given for this system is close to those of the compliant walls investigated by

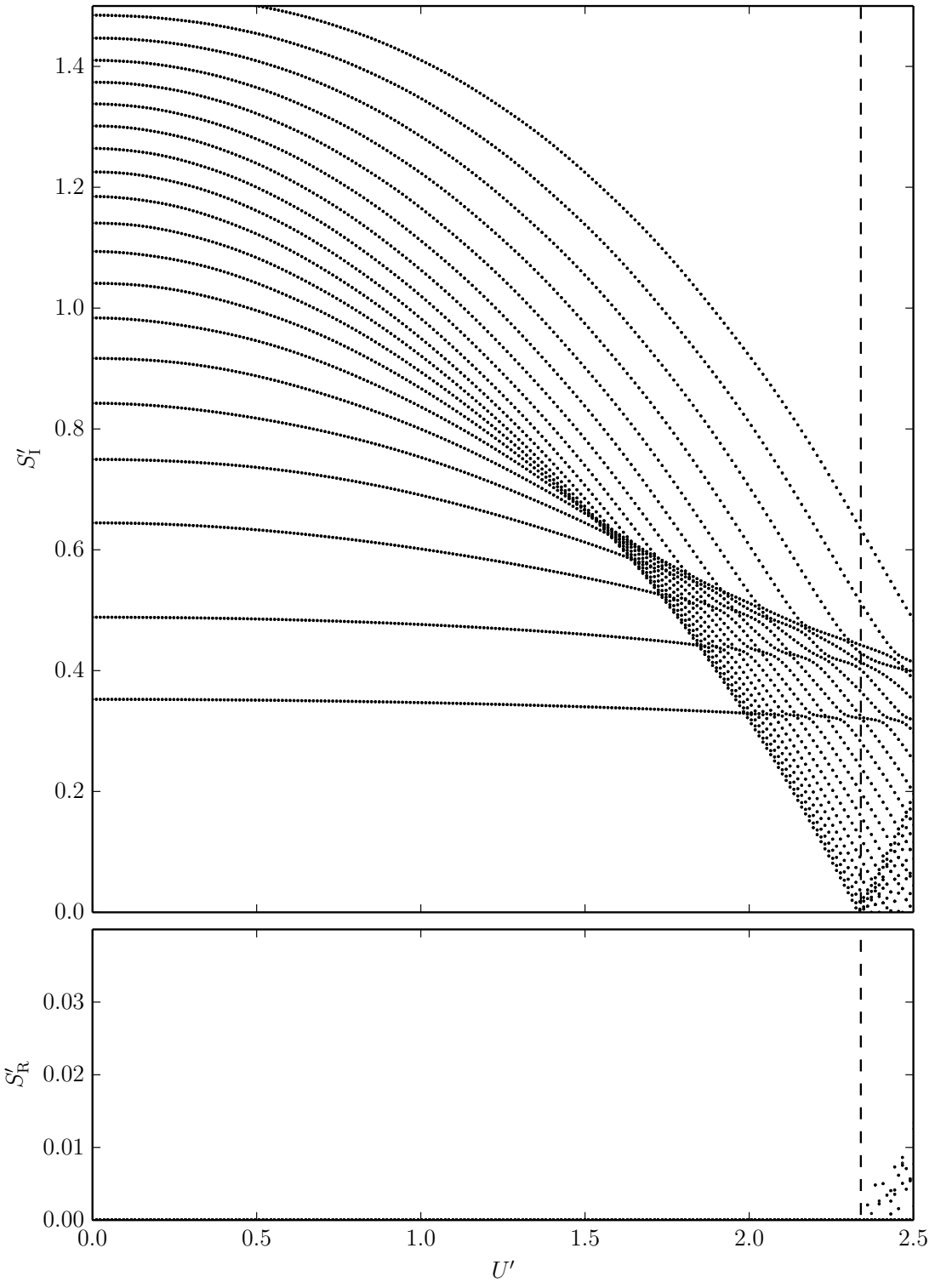

Figure 3.9: The variation of the real and imaginary parts of the 40 lowest, positive eigenvalues with flow speed for a spring-backed flexible plate with mass ratio $\mu = 70.4$ in an open flow. The vertical dashed line indicates the critical flow speed at which the eigenvalues first have a positive real value.

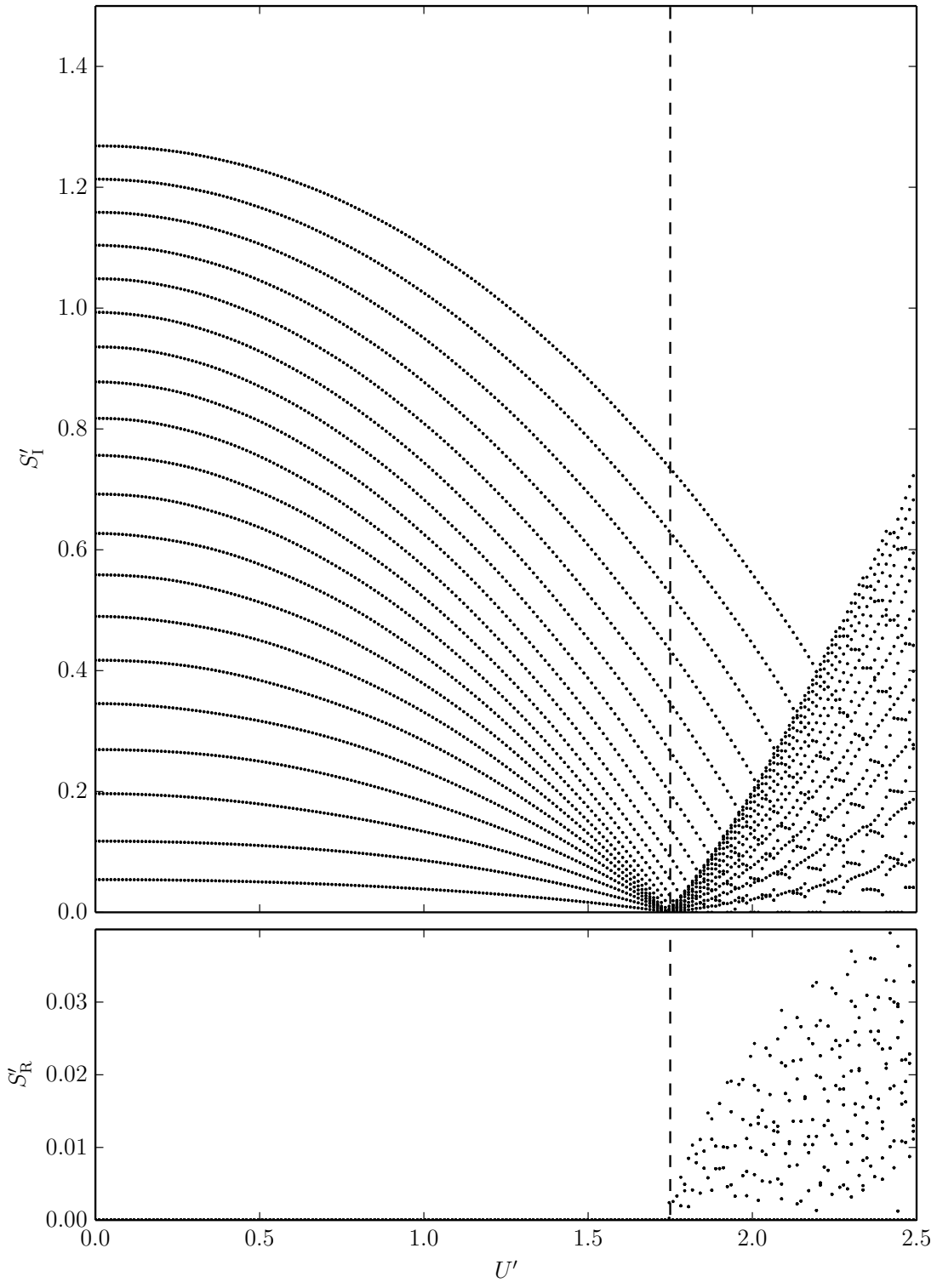

Figure 3.10: The variation of the real and imaginary parts of the 40 lowest, positive eigenvalues with flow speed for a spring-backed flexible plate with mass ratio $\mu = 70.4$ in a channel flow with $H' = 0.7$. The vertical dashed line indicates the critical flow speed at which the eigenvalues first have a positive real value.

Carpenter and Garrad (1986), Lucey et al. (1997) and Pitman and Lucey (2009) that were chosen to represent water interacting with the compliant coating of Kramer (1960) that showed the best performance for transition postponement in an open boundary-layer flow.

Figures 3.9 and 3.10 respectively show the dependence of the lowest 40, positive eigenvalues of the FSI system on the flow speed for the equivalent open flow and for a channel with $H' = 0.7$ when $K' = 4.367$. In these figures the onset of divergence occurs when the real part of an eigenvalue first becomes positive; the flow speed at which this occurs is marked in each of Figures 3.9 and 3.10 by a vertical dashed line. For the open-flow case ($H' = \infty$), divergence onset occurs at $U' = 2.34$. By plotting the associated eigenvector, or tracing the mode that first crosses the $S_{\mathrm{I}} = 0$ axis in Figure 3.9, the critical mode is found to be 24, giving the critical wavelength, $\lambda'_{\mathrm{s}} = 5.87$ where $\lambda'_{\mathrm{s}} = (\lambda_{\mathrm{s}}\rho_{\mathrm{f}}) \,/\, (h\rho_{\mathrm{m}})$. These critical values agree well with the predictions of $U' = 2.30$ and $\lambda'_{\mathrm{s}} = 5.72$, given by Equations (3.45) that recovered the analytical expressions of Carpenter and Garrad (1986) for a corresponding compliant wall of infinite length. It is remarked that $\lambda'_{\mathrm{s}}/L' = 0.0834$ for the critical mode arising at divergence onset in Figure 3.9, thus, at this very small value of the ratio of disturbance wavelength to insert length, the actual length of the flexible insert has little influence on the critical mode and flow speed for divergence onset.

At flow speeds just above divergence onset, Pitman and Lucey (2009) showed that divergence instability is realised as slow downstream-travelling amplifying waves, a form that is predicted by a travelling-wave theory based upon a wall of infinite extent. This realisation of divergence instability as slow downstream-travelling waves continues to hold in the present channel-flow system.

Comparing the result of Figure 3.9 with that of Figure 3.10 it is seen that finite channel height reduces the critical flow speed for divergence onset, although the solution morphology of the eigen-system is largely unchanged. The critical mode now has a wavelength $\lambda'_{\mathrm{s}} = 6.12$ which is longer than that of the corresponding open-flow case. The variation of divergence-onset flow speed with channel height is summarised in Figure 3.11 (a) for the parameters used to generate Figure 3.10 and two further levels of foundation spring-stiffness, K'. Also included in this

figure are the analytical predictions of Equation (3.44) based upon the assumption of an infinitely long flexible insert for each of the spring foundations. As would be expected, the lines of critical flow speed are displaced upwards for higher values of K'; a stiffer wall has a higher critical speed. It is also noted that the wavelength of the critical mode becomes shorter as K' is increased. For each of the pairs of lines associated with a K', the effect of reducing the channel height is seen to be destabilising and this effect begins to occur below values of H' that are lower when K' is higher. Thus, the effect of channel height scales with the wavelength of the critical mode. This suggests that a general result for all spring-backed flexible plates is attainable. An alternative non-dimensional system is therefore considered by defining channel height relative to critical wavelength, $H/\lambda_{\rm s}$, and non-dimensionalising the flow speed as a stiffness ratio defined as,

$$\Lambda^{\rm I} = \frac{\rho_{\rm f} U^2}{(BK^3)^{1/4}}, \tag{3.55}$$

which is based upon the length scale and flow-to-structural pressure ratio implicit in Equations (3.45)a, b and discussed in Lucey et al. (1997). Re-plotting all of the data in Figure 3.11 (a) gives the result of Figure 3.11 (b) in which the different K'-curves have collapsed onto a single variation of divergence-onset flow speed with channel height.

Having definitively characterised the divergence-onset results from the state-space analysis of an insert with finite length, albeit long relative to the wavelength of the critical mode, attention is now given to the validity of the analytical prediction based upon the assumption of an insert of infinite length. The latter is plotted in Figure 3.11 (b) along with the results of the asymptotic limits, $H \to 0$ and $H \to \infty$, given by the non-dimensionalised forms of Equations (3.45b) and (3.48a) respectively. The two methods clearly agree well and it is noted that the percentage difference between the two methods (being 2.43% for $H/\lambda_{\rm s} > 0.6$) reduces with the channel height so that, for example, at $H/\lambda_{\rm s} = 0.02$ there is a 0.2% difference. The simple asymptotic forms, Equations (21b) and (24a), are seen to yield excellent agreement with the results of full theoretical treatments over a surprisingly wide range of each of the low and high values H/λ_c for which they are solutions in the exact limit.

To explain why there is better agreement as the channel is made narrower,

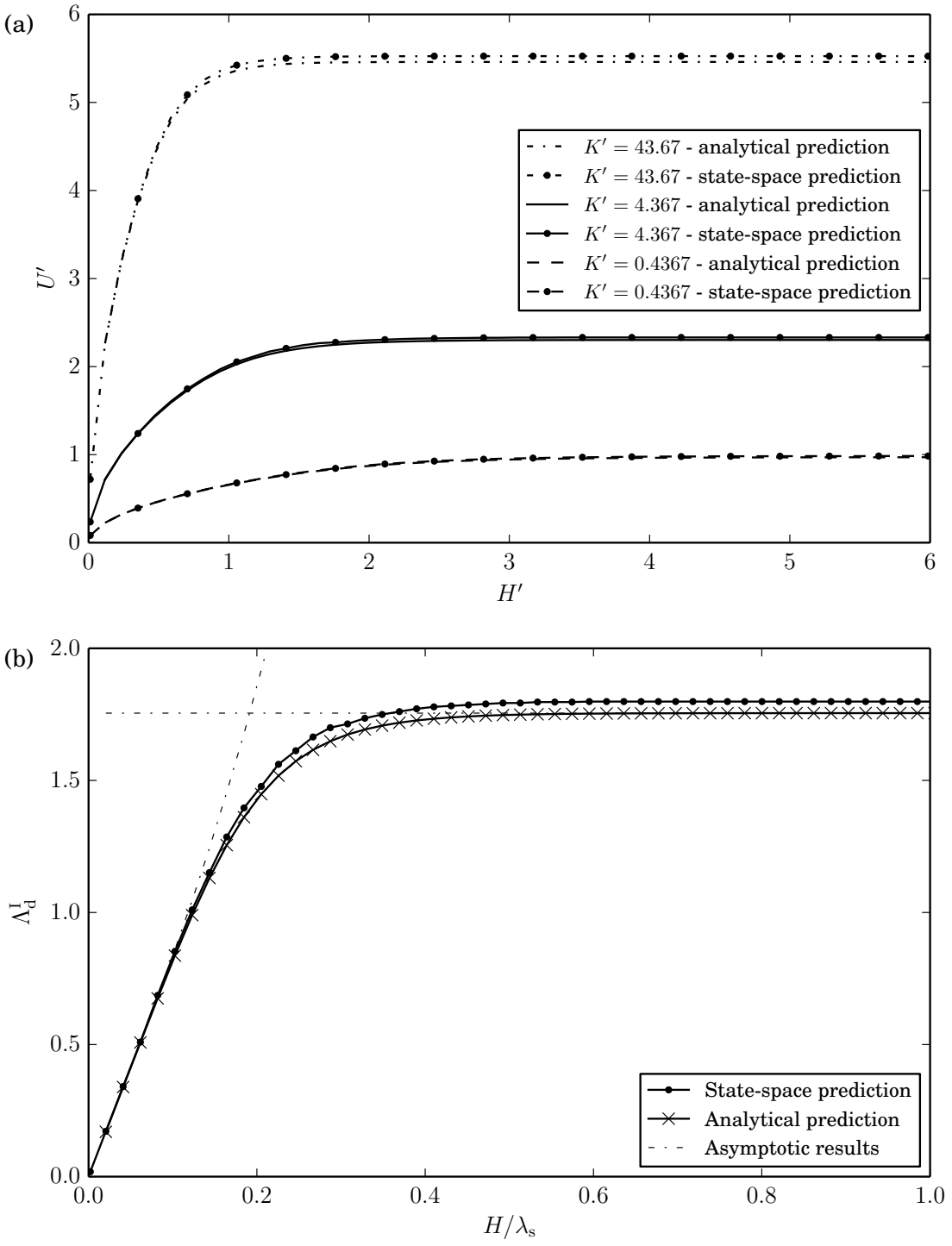

Figure 3.11: The dependence of divergence-onset flow speed of a spring-backed flexible plate on channel height comparing the results of analytical and state-space forms for three different spring foundations: (a) using the non-dimensional scheme of Lucey and Peake (2003) and (b) a non-dimensional scheme based upon that used in Lucey et al. (1997) including, as dot-dashed lines, the asymptotic results of Equations (3.45b) and (3.48a) of the analytical predictions.

Figure 3.12 (a) compares insert deformations for the case $K' = 4.367$ and channel height $H' = 2.0$ (effectively an open flow) at divergence onset ($U' = 2.3$) as assumed in the travelling-wave solution (upper panel) and as calculated using the state-space solution (lower panel). It is evident that while both support a critical mode with the same wavelength, the latter features an amplitude modulation, the shape of which is very close to that of the fundamental mode that has been sketched in using a dashed line. Amplitude modulation was shown in the divergence waves predicted by Pitman and Lucey (2009) for an open flow at flow speeds higher than that of divergence onset; their results also identify unstable states where the amplitude modulation takes the shape of the second and third modes of the overall panel. However, it is most likely that the lowest energy state - that of the fundamental - would dominate the physical destabilisation of the finite flexible wall. Figure 3.12 (b) makes the same comparison as Figure 3.12 (a) but now for channel flow with $H' = 0.5$, again exactly at divergence onset ($U' = 1.47$). For the finite wall (lower panel) there is now little evidence of amplitude modulation in the calculated deformation and therefore the form assumed in the travelling-wave assumption of disturbances (upper panel) yields results that more closely agree with the exact representation of the compliant insert.

To demonstrate how the condition of finiteness affects the hydrodynamic loading, Figure 3.12 (c) shows the spatial variation of the coefficient of the hydrodynamic stiffness term in Equation (3.11) for a uniform deformation amplitude, as assumed in the analysis of a flexible wall of infinite length, for each of $H' = 0.5$, $H' = 2.0$ and the corresponding open flow each at the flow speed of divergence onset. Clearly the pressure evaluation based upon the assumption of an infinite flexible wall (not plotted) would yield a constant value across the wall for each case in Figure 3.12 (c). For the finite-wall pressure evaluation, the pressure loading is seen to be constant across the middle region of flexible wall but there is significant variation adjacent to the leading and trailing edges of the flexible panel. This reflects the fact that for a finite insert, each spatial location is unique with respect to the hydrodynamic influence it receives from the effect of boundary deformations upstream and downstream of it. For open flows, a discussion, and mathematical demonstration, of the spatial variation of hydrodynamic forces

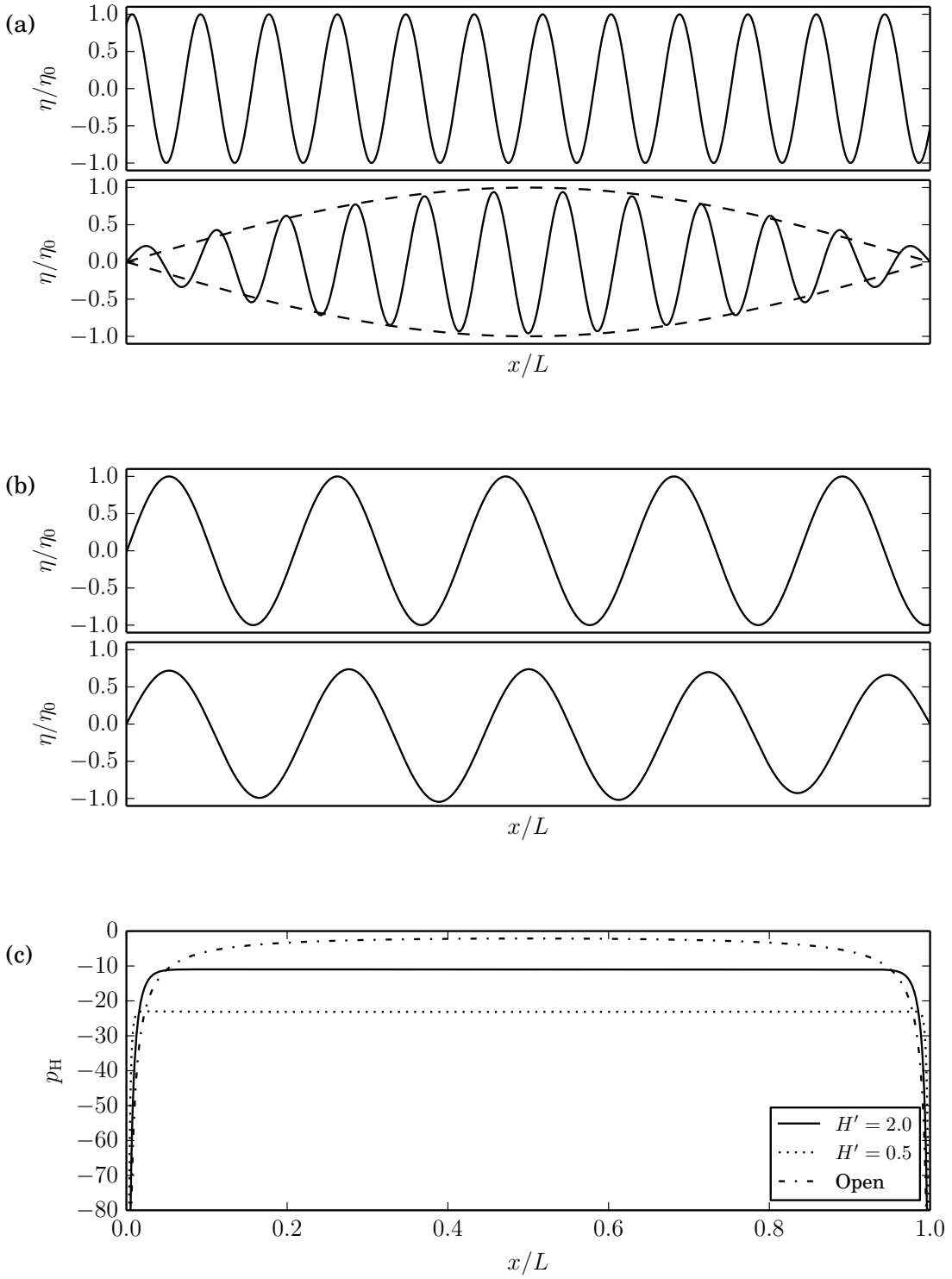

Figure 3.12: Flexible-wall deformation at divergence onset when $K' = 4.367$ as assumed in the analytical method (upper) and as predicted by the state-space solution (lower) when: (a) $H' = 2.0$, and (b) $H' = 0.5$. (c) The spatial variation of the hydrodynamic-stiffness coefficient for uniform deflection amplitude at divergence onset for the open flow and the two channel heights used for (a) and (b).

over a compliant wall of finite length is presented in Lucey and Carpenter (1993b) and the special modelling required to model finite panels using travelling-wave approaches is presented in Peake (2004). It is the imbalance between structural forces and pressure loading for uniform amplitude that leads to amplitude modulation - the state in which these forces are exactly balanced across the entire flexible wall - when a finite wall is correctly analysed. However, what the results Figure 3.12 (c) clearly show is that as the channel height is reduced, the extent of the influence of the leading- and trailing-edge effects on the pressure reduces and therefore the assumptions in the travelling-wave model are less restrictive in its representation of a truly finite compliant wall interacting with an inviscid fluid flow.

The present travelling-wave analysis is now extended to include spring-backed flexible plates to replace both rigid walls of the channel so as to compare the findings with those of Weaver and Païdoussis (1977). The methods outlined in Section 3.1.4 are modified to make both channel walls flexible by changing the boundary conditions to,

$$\frac{\partial \phi}{\partial y} = \frac{\partial \eta}{\partial t} + U\frac{\partial \eta}{\partial x} \qquad \text{at} \qquad y = \eta, H + \eta. \tag{3.56}$$

The variation of divergence-onset flow speed with channel height for $K' = 4.367$ are presented in Figure 3.13 using a non-dimensional flow velocity defined by Weaver and Païdoussis (1977) wherein $\bar{V} = U/c$ and c is a reference free-wave speed of the flexible wall; for a spring-backed flexible plate c is given by,

$$c = \sqrt{\frac{1}{\rho_{\mathrm{m}} h}\left(\frac{Bk^4 + K}{k^2}\right)}. \tag{3.57}$$

To generate a reference value, k is chosen to be the critical wavenumber defined by Equation (3.45a). Both in-phase (sinuous) and out-of-phase (varicose) deformations of the flexible channel are plotted as well as the results for a channel with just one flexible wall and the corresponding predictions of the state-space solution when the insert is very long. When both walls of the channel are flexible, the present results show close qualitative agreement with the results of Weaver and Païdoussis (1977) shown in Figure 6 of their paper that were obtained using a travelling-wave assumption for the stream-wise variation of wall deformations

combined with a modal weighting to account for transverse three-dimensional effects. Exact quantitative agreement could not be expected because of the transverse effects in Weaver and Païdoussis (1977) that increase the divergence-onset flow speed as compared with a two-dimensional analysis and because in the present study a spring-backed flexible-plate is used. The present results, like those of Weaver and Païdoussis (1977) show that the divergence-onset flow speed tends to infinity for in-phase (sinuous) deformations as the channel height is reduced and serve as a further source of validation. For this case, the flow does not vary across the channel cross-section; it is effectively one-dimensional, following the curved contour of the deformed channel. Destabilisation occurs when the centrifugal force of the fluid flow exceeds the restorative forces of the channel walls. Clearly the centrifugal force depends upon the mass of fluid, hence the channel height, traversing the curved path and therefore reducing channel height increases the required flow speed for destabilisation.

When out-of-phase (varicose) motion of the walls occurs, the present results indicate that reducing the channel height is destabilising and that in the limit

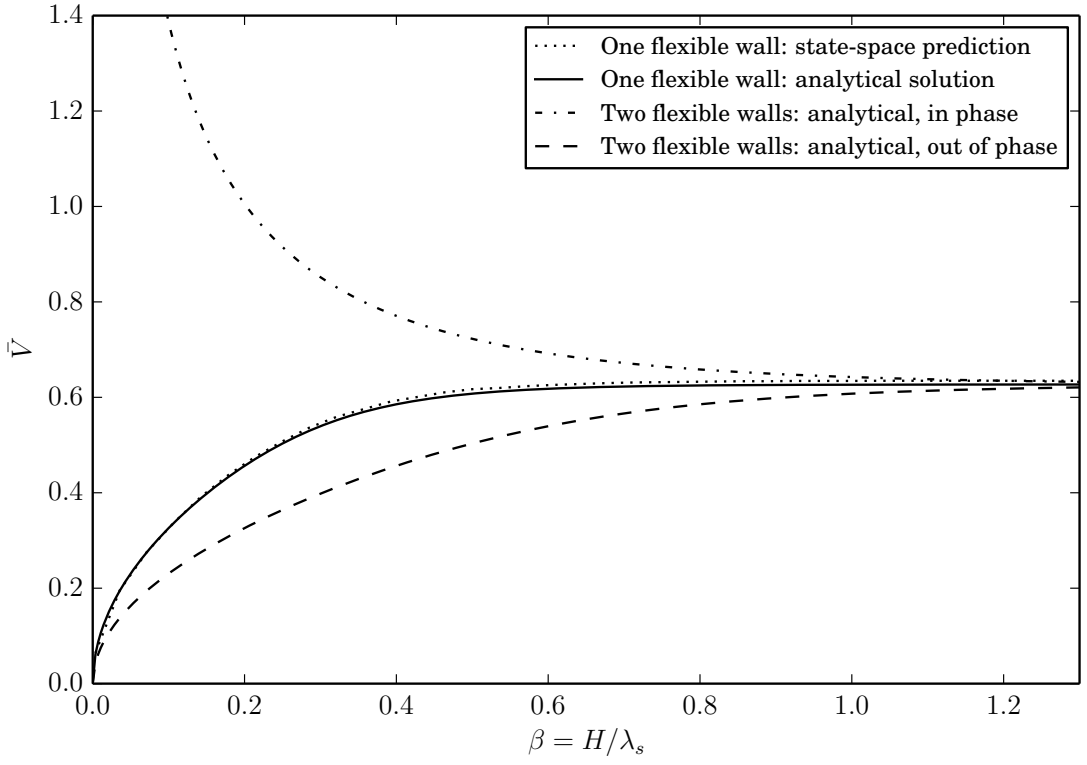

Figure 3.13: Analytical prediction for one and two flexible-channel walls compared with the state-space results.

$H \to 0$, instability occurs at zero flow speed; this echoes the findings of Weaver and Païdoussis (1977). The results in Figure 3.13 for one flexible wall show the same trends as those of varicose motion although the destabilising effects of channel height occur at lower values of channel height. When the channel height for the two-sided flexible insert is twice that used in the analysis of a one-sided flexible insert, exact collapse of results occurs showing that the straight channel centreline of the former has the same effect as the flat upper wall in the one-sided spring-backed flexible plate case.

The present investigation of a spring-backed flexible plate as one wall of a fluid-conveying plane channel has resulted in the characterisation of divergence onset as a single variation of non-dimensional critical flow speed with channel height that accounts for all of the system's physical parameters. This definitive quantification shows that reducing the channel height has a destabilising effect, in that it reduces the critical flow speed, and that channel-height effects scale with the wavelength of the critical divergence mode. The analytical treatment, based upon a travelling-wave assumption of disturbance form is shown to agree well with the predictions of the state-space solution that correctly accounts for the finiteness of the flexible insert. The relatively small differences in the predictions of the two methods developed here has been explained as arising from amplitude modulation of the critical mode when fixed leading- and trailing-edge are strictly enforced. However this disparity has been shown to reduce as channel height is decreased. Finally, simple asymptotic forms of the full analytical solution have been shown to provide excellent approximations of critical speed over significant ranges of both small and large channel heights.

3.3.2 Double Sided Channel

Attention is now turned to the case of a flexible insert comprising a section of one wall of a surface that separates two channel flows that are otherwise rigid, conveying a potential flow as depicted in Figure 1.2 (c).

The properties in each the results presented here are kept constant so as to focus on the effect being varied and are, unless otherwise stated: $L = 0.6$ m, $h = 0.0025$ m, $H_1 = 0.6$ m, $\rho_{\mathrm{m}} = 2600$ kg/m^3, $B = 76.62$ N/m^2 and $\rho_1 = 1000$

kg/m^3 with no structural damping, spring-backing or tension. These dimensions give a mass ratio $\mu = 92.3$.

When the properties of the two channels differ, Λ^{F} refers to the properties of channel one and the results are presented in terms of a variable κ which relates the properties of Channel 2 to those of Channel 1, i.e. $U_2 = \kappa_U U_1$ or $\rho_2 = \kappa_\rho \rho_1$.

Setting the fluid density in one channel to $\rho_{\mathrm{f}} = 0$ kg/m^3 reproduces the open flow result of Figure 3.3 when the channel walls are sufficiently far away.

Varying the Channel Height

The system considered here is one where each channel has the same system properties, i.e. $\rho_1 = \rho_2$, $U_1 = U_2$ and $H = H_1 = H_2$. The eigenvalue curves for various channel heights, H, are shown in Figure 3.14 (a). In each case, the four distinct flexible-wall behaviour types noted for the single sided channel in Section 3.3.1: pre-divergence, divergence, divergence recovery and modal-coalescence flutter are still present. In this case however the critical stability bounds are altered from the single sided channel, even as $H/L \to \infty$.

The results presented here can be compared to those of Guo and Paidoussis (2000) when they consider pinned-pinned boundary conditions. The form of the eigenvalue solutions are largely the same except that their finite length central surface does not appear to experience divergence recovery, likely due to flow not being completely separated by the central surface.

It can be seen from Figure 3.14 (a) that reducing the channel height causes each instability type to occur at a lower non-dimensional flow velocity, and the values of the imaginary part of the eigenvalues are reduced; thus at a zero flow speed the narrower channel causes the wall to oscillate at a lower frequency. This is due to an increase in pressure on the flexible wall caused by the closer proximity of the outer walls. It can also been seen that the form of the eigenvalue curves is unchanged by the parameter H. Guo and Paidoussis (2000) and Epstein et al. (1995) show that reducing the channel height causes both divergence (Guo and Paidoussis (2000)) and flutter (Epstein et al. (1995)) to occur at lower flow velocities which agrees with the results found here.

The effect of H on the critical flow velocity of each instability type is shown

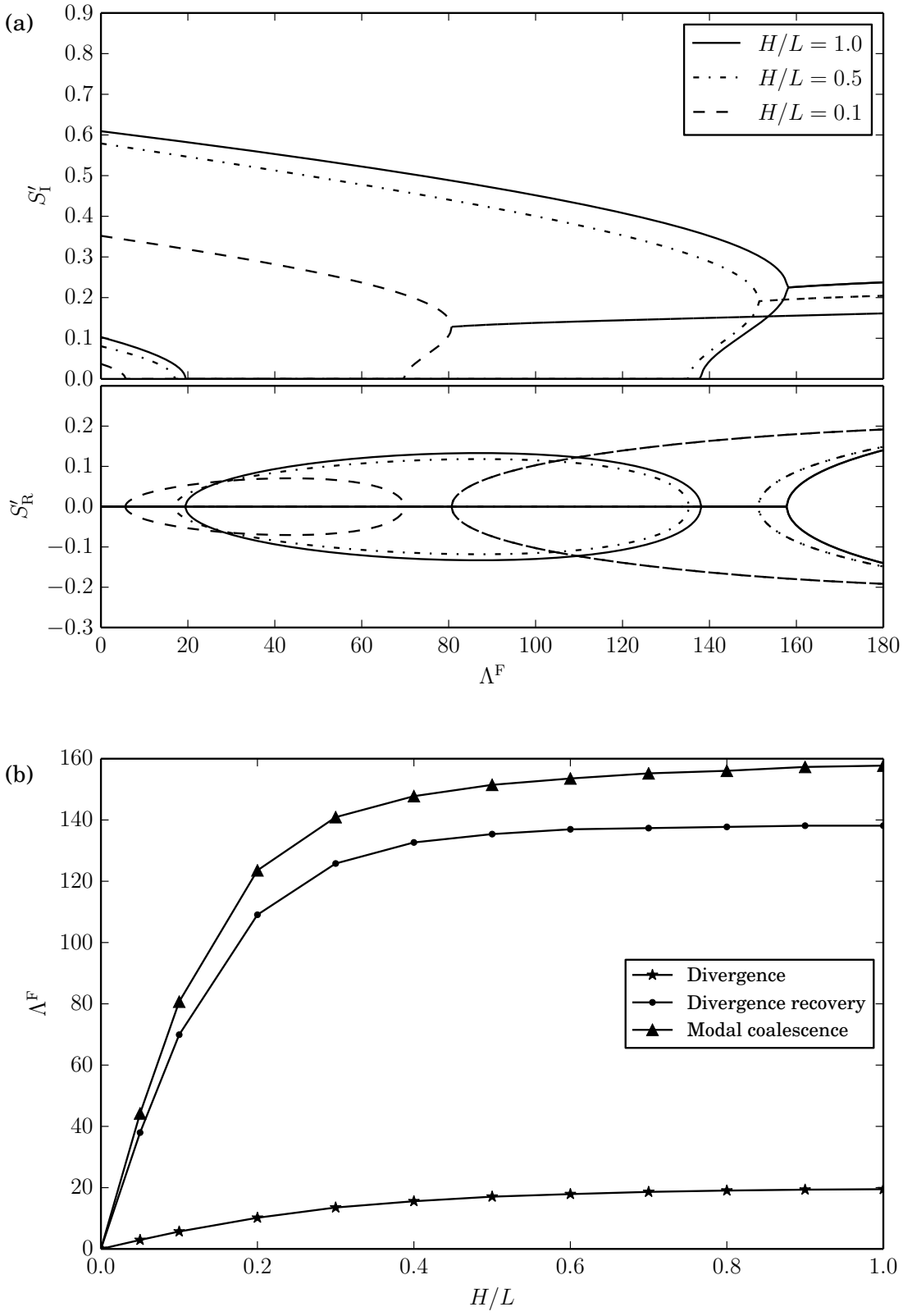

Figure 3.14: Effect of varying the channel height, $H = H_1 = H_2$, (a) Eigenvalue curves at three different non-dimensional channel heights, (b) Summary of the effect of channel height on the onset of divergence, divergence recovery and modal-coalescence flutter.

in Figure 3.14 (b) and it can be seen that they asymptotically approach a value where the flexible-wall behaviour is no longer affected by the upper and lower rigid walls at sufficiently large H. This happens at approximately $H/L = 1$ which agrees with Guo and Paidoussis (2000) although in both results it can be seen that there is still a very small effect from the channel walls for greater channel widths, more noticeably for modal-coalescence. We note that the critical non-dimensional flow velocities for divergence, divergence recovery and modal-coalescence are $\Lambda^{\mathrm{F}} = 20, 137, 160$ respectively for H/L large enough that the presence of the outer walls is small enough that the critical flow velocities do not vary significantly for wider channels. These are approximately half the critical values found by Tan et al. (2010) and shown in Section 3.3.1 which is to be expected as the pressure is doubled by the presence of fluid on both sides of the wall. This serves as a source of validation that the state-space method has been correctly applied to this geometry.

Varying the Channel Densities

Here the effect of varying the fluid density in Channel 2 and maintaining the fluid density of Channel 1 as a constant ($\rho_1 = 1000$ kg/m^3) is considered. The channel heights are set equal at $H_1 = H_2 = 0.6$ m, hence $H_1/L = H_2/L = 1$. The fluid density of Channel 2 is given by $\rho_2 = \kappa_\rho \rho_1$ and the effect of varying κ_ρ on the eigenvalues is shown in Figure 3.15 (a). It can be seen that reducing the fluid density in channel two results in instability onset occurring at higher applied flow speeds due to the decrease in the pressure on the flexible wall. This effect has been summarised in Figure 3.15 (b). Again, it can also be seen that the form of the eigenvalue curves remains unchanged and that the frequency decreases with κ_ρ.

When the fluid density in Channel 2 is zero, the system can be considered as being the same as the open flow case and the eigenvalues for large enough H/L are the same as shown in Tan et al. (2010). This also agrees with the results of Section 3.3.1 for large values of H/L and the onset speed of divergence $\Lambda^{\mathrm{F}} = 40$ recovers the well known value for the open flow (Weaver and Unny (1970), Pitman and Lucey (2009) and Tan et al. (2010)).

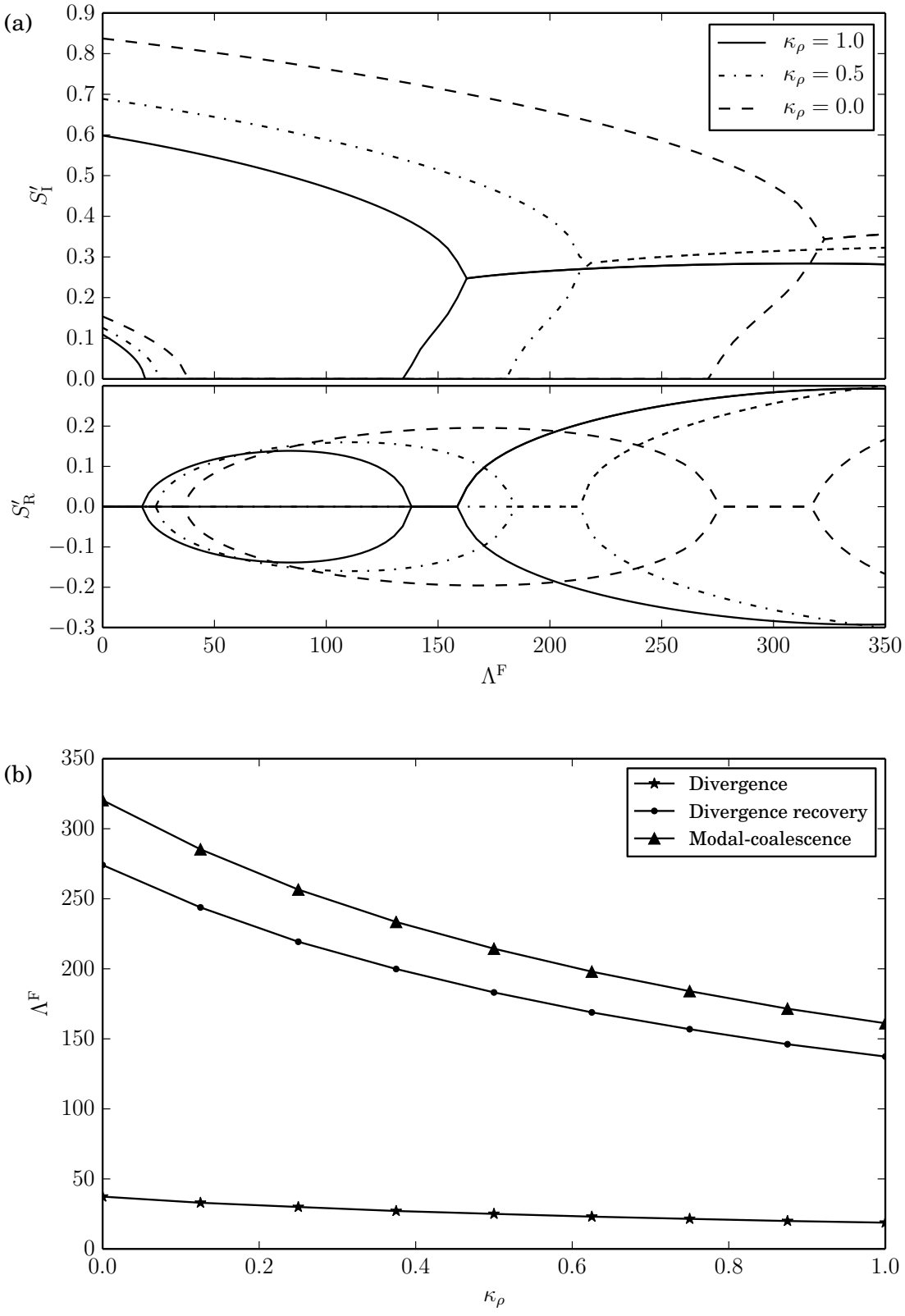

Figure 3.15: Effect of varying the fluid density in one channel for $H_1/L = H_2/L = 1$, (a) Eigenvalue curves at three different fluid densities, (b) Summary of the effect of fluid density on the onset of divergence, divergence recovery and modal-coalescence flutter.

Channels of Differing Flow Velocities

To consider channels of different flow velocities the height and fluid density of each channel is maintained ($H_1 = H_2 = 0.6$ m, hence $H_1/L = H_2/L = 1$ and $\rho_1 = \rho_2 = 1000$ kg/m^3) and the flow velocities in each channel are related by κ_U, so that $U_2 = \kappa_U U_1$.

When $0 \leq \kappa_U \leq 1$, reducing κ_U causes instability onset to occur at higher applied flow velocities as can be seen in Figure 3.16 (a). In this case the eigenvalues do not change with κ_U at a zero flow velocity because only the fluid inertia forms the pressure load at $U_1 = U_2 = 0$, i.e. when $\Lambda^{\mathrm{F}} = 0$.

However when $-1 \leq \kappa_U < 0$, the eigenvalue curves change qualitatively as well as quantitatively as can be seen in Figure 3.16 (b). At $\kappa_U = 0.0$ in Figure 3.16 (a), the divergence-recovery zone is noticeably smaller and has disappeared completely when $\kappa_U = -0.5$ as shown in Figure 3.16 (b). Instead of the divergence-recovery zone, the second mode destabilises before modal-coalescence occurs and the flexible wall displays a new type of behaviour known as second mode divergence. Modal-coalescence then occurs ($\Lambda^{\mathrm{F}} = 225$ for $\kappa_U = -0.5$) and at even higher flow velocities the second mode divergence takes place again as can be seen in the $\kappa_U = -0.75$ case. The form of these eigenvalue curves remains constant as κ_U continues to decrease for $-1.0 < \kappa_U \leq 0.0$, where the range of non-dimensional flow speeds at which modal-coalescence flutter occurs gets smaller as κ_U decreases. At $\kappa_U = -1.0$ there is no modal-coalescence between modes 1 and 2 and beyond $\Lambda^{\mathrm{F}} = 175$ mode 2 divergence is the dominant instability.

A summary of the onset of each instability type as it varies with κ_U is shown in Figure 3.17 where the two cases of divergence recovery can be seen for negative κ_U. It can be seen in Figure 3.17 that divergence onset is symmetrical about $\kappa_U = 0$, indicating that divergence onset is only affected by the magnitude of the flow velocity and not the direction. This does not hold true for modal-coalescence.

The non-dimensional deflections of the flexible wall shown in Figure 3.18 for (a) $\kappa_U = 1.0$ and (b) $\kappa_U = -1.0$ demonstrate that when each channel has equal but opposite flow velocities, the wall deflections are symmetrical about the mid-point of the flexible wall. This does not occur in all other cases as the channel with the greatest flow velocity causes the beam deflections to be skewed in the

direction of the flow.

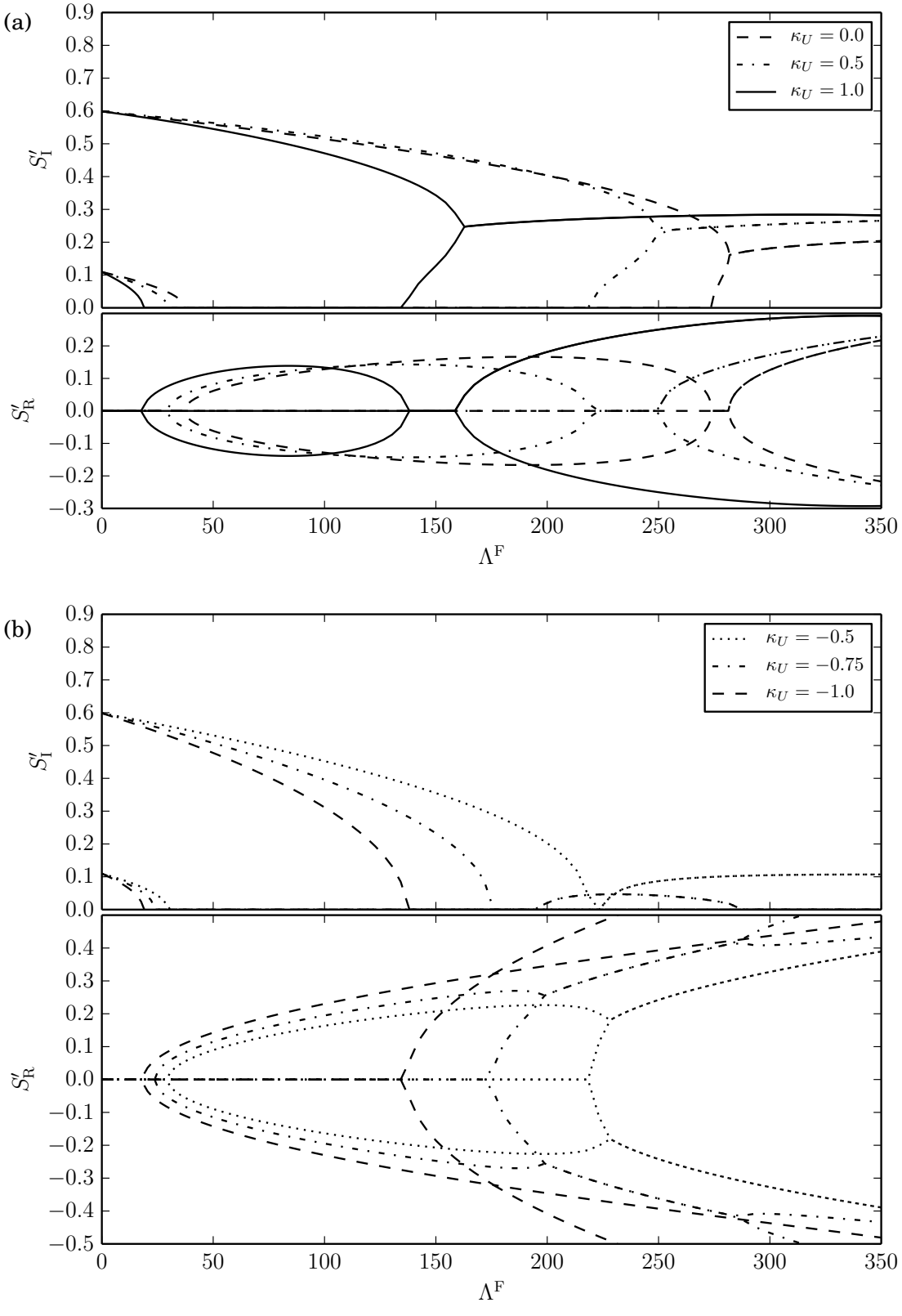

Figure 3.16: Effect of channels of different flow velocities where $U_2 = \kappa_U U_1$, (a) Eigenvalue curves at three different values of κ_U for $0 \leq \kappa_U \leq 1$, (b) Eigenvalue curves at three different values of κ_U for $-1 \leq \kappa_U \leq 0$.

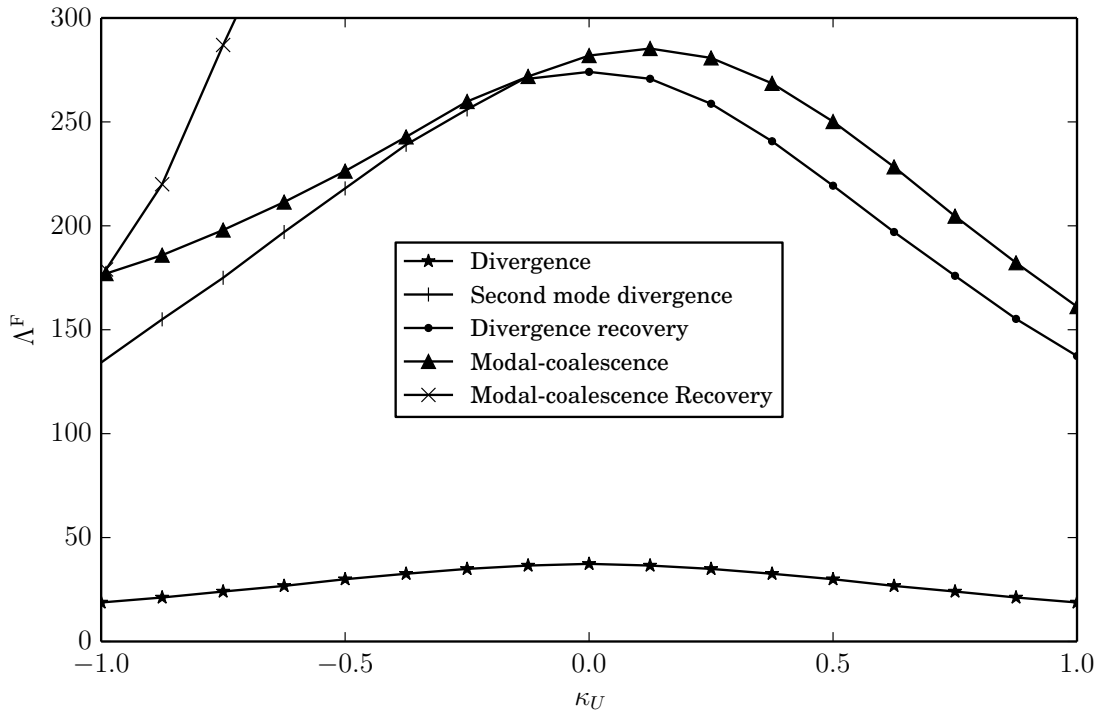

Figure 3.17: Summary of the effect of varying κ_U on the onset of each instability type for $-1 \leq \kappa_U \leq 1$.

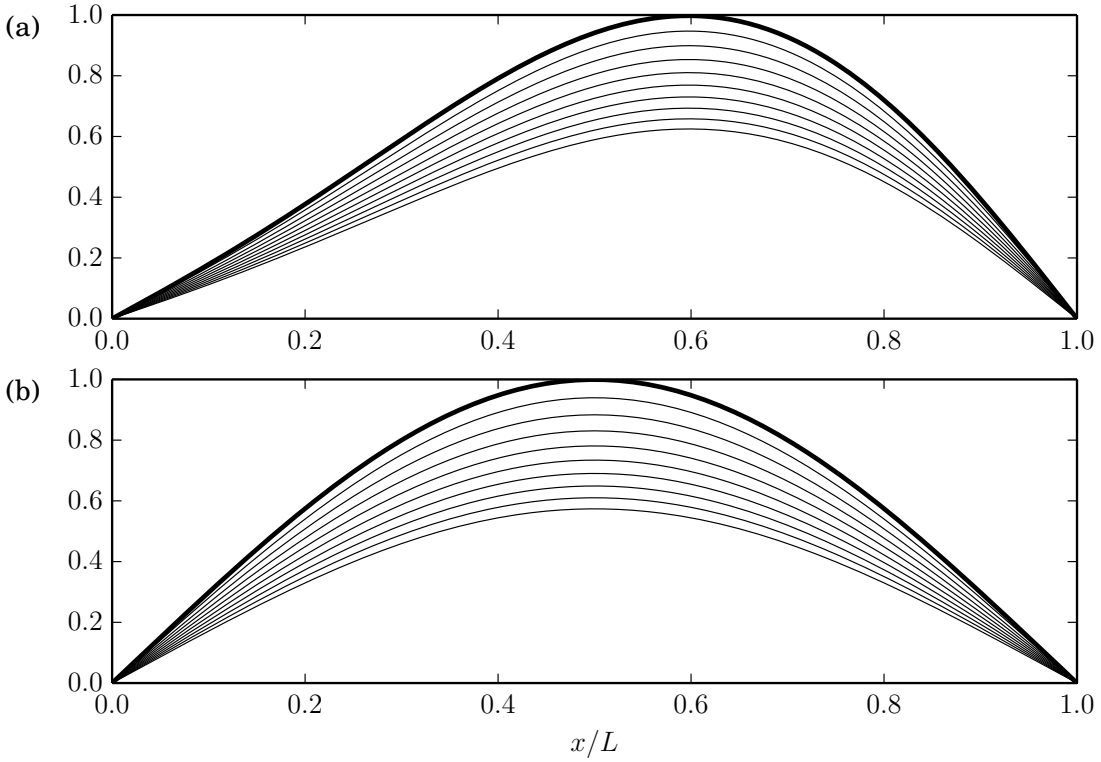

Figure 3.18: Non-dimensional beam deflections for mode 1 divergence instability at $\Lambda^F = 45$ for (a) $\kappa_U = 1.0$ and (b) $\kappa_U = -1.0$. The bold line indicates the final position of the flexible wall.

3.4 Summary

3.4.1 Single Sided Channel

An extension of the modelling of Pitman and Lucey (2009) that comprises a hybrid of computational and theoretical methods has been developed to study the stability of a flexible insert in one wall of an otherwise rigid channel conveying an inviscid flow. Results for the case where the upper channel wall is sufficiently far from the lower wall in which the flexible insert is embedded recover the results of previous studies of the classical problem of a flexible panel or compliant wall interacting with an open flow. For flexible inserts comprising a structure for which the critical mode at instability onset is much shorter than the panel length, an analytical solution has been developed. In the limit of infinite channel-wall separation, this solution recovers the equivalent formulae derived for an open flow. These limiting cases serve to validate each of the two approaches developed, that account for the confinement effects of finite channel height.

A comprehensive investigation of the stability of a range of flexible-insert types has been conducted using an eigen-analysis of the fluid-structure system. In all cases it was found that reducing the channel height causes the onset of divergence and modal-coalescence flutter to occur at lower flow velocities and the frequency of both system modes prior to instability onset and flutter to be reduced. These effects have been quantified in non-dimensional form. For simple plates and membranes, there is a channel height-to-insert-length, H/L, typically unity, above which the effects of the upper wall are negligible irrespective of the mass ratio of the FSI system and whether structural damping is included.

For the more complex structure of a spring-backed flexible plate (or compliant wall), it is found that the effect of the channel height scales with the wavelength of the critical mode as opposed to the overall length of the flexible insert. When comparing the two methods developed and deployed for this type of flexible wall, it has been shown that the analytical solution based upon a travelling-wave form of wall deformation, predicts divergence-onset flow speeds that agree very well with the corresponding analysis of a finite insert using the state-space solution. The agreement improves as the channel height is decreased. This has been shown

to arise from a reduction, as the channel height is decreased, in the amplitude modulation of the divergence mode that occurs when fixed insert ends are modelled. This finding suggests that the classical hydrodynamic-stability approach used to make more complete fluid-flow models tractable, for example when perturbations to mean flow velocity profile arising from viscous effects are modelled, will provide a good approximation of compliant-wall interactions if the channel height is small. Simple asymptotic forms of the full analytical solution have been shown to provide excellent approximations of critical speed over appropriate ranges of channel height and these can serve as useful design formulae in engineering applications.

The overall contribution of these results is a comprehensive set of stability bounds for inviscid channel flow interacting with a flexible insert. These results effectively represent the FSI of flexible inserts in an otherwise rigid-walled channel at the limit of infinite Reynolds number and therefore provide useful engineering approximations for applications wherein the Reynolds number of the flow is very high. They can also serve as a benchmark - as the infinite Reynolds-number limit - for the validation of future theoretical and computational models wherein turbulent flow at finite Reynolds number interacts with and destabilises a compliant insert.

3.4.2 Double Sided Channel

A state-space method has been developed for a finite elastic wall that separates two inviscid channel flows. The wall and fluid motions are coupled at the fluid-solid boundary by the pressure and the flow velocity at which instabilities in the wall occur are predicted for a given set of system parameters. Overall, the results show how the properties of the system can be varied in order to delay or advance the onset of instability in a flexible wall bounded by two distinct channels.

It is found that making one or both of the channels narrower causes instability to occur at lower flow velocities, as does increasing the fluid density in one channel from zero to a value equal to that in the other channel.

When the two channels have flows at different velocities, decreasing the flow velocity in one channel is stabilising as would be expected. When the fluids

are flowing in opposite directions the eigenvalue morphology changes; there is no longer a divergence-recovery regime, but second mode divergence occurs instead, followed by the usual modal-coalescence flutter. When the flows are at exactly opposite velocities, modal-coalescence no longer occurs. This effect can be explained by considering the four pressure terms in Equation (3.11). The hydrodynamic stiffness does not depend on the flow direction but only its magnitude and the hydrodynamic inertia does not depend on the flow velocity but only the fluid density, whereas the hydrodynamic damping depends on both the magnitude and direction of the flow velocity. It is this damping term that couples the modes at high enough flow velocities resulting in modal-coalescence. When the two channels have exactly opposite velocities this coupling effect is cancelled out and modal-coalescence of the first two modes can no longer occur.

Chapter 4

Non-Modal Analysis

In Chapter 3 linear (small amplitude) deflections of a finite flexible insert in open and channel flows are considered to investigate the stability bounds of divergence and modal-coalescence flutter. In Chapter 5 nonlinear (large amplitude) deflections of a finite flexible plate are considered, where the large deformations grow from an initial small amplitude disturbance. This Chapter serves as a bridge between the linear and nonlinear investigations to establish whether large amplifications are possible from transient growth by considering the maximum energy bound of the system and whether nonlinear disturbance growth may occur before linear instability onset, as predicted from the linear eigen-analysis. Open and channel flow systems are considered as depicted in Figures 1.1 (a) and 1.2 (a) respectively. This chapter outlines the method used, followed by results with comparisons from similar previous investigations.

Where results show high finite amplitude deformations of the plate, it is noted that further nonlinear structural forces such as induced tension have a significant impact, and that nonlinear fluid mechanics may also influence the results, however they have not been considered in this chapter as the method uses a superposition of the linear eignmodes. The nonlinear modelling is considered in Chapter 5.

4.1 Method

4.1.1 Transient Growth

The governing equations of a potential open flow over a finite flexible plate are the same as those presented in Section 3.1.1 and they are solved by the same method outlined in Section 3.1.2. In this way the eigenvalues and eigenvectors of the system are calculated. Transient energy amplifications are then considered using a method based on that of Schmid and de Langre (2003), Coppola and de Luca (2010) and Tsigklifis and Lucey (2013). Transient effects and non-normal effects were first investigated by Schmid and Henningson (2001) and methods and a range of applications have been detailed and explored by Trefethen and Embree (2005). The energy norm for the present system is defined by Tsigklifis and Lucey (2013) as,

$$\begin{gathered} E(t) = \frac{1}{2}\int_0^H \int_0^L \left(|u_x|^2 + |u_y|^2\right) \mathrm{d}x\, \mathrm{d}y + \\ \frac{1}{2}\int_0^L \left(\rho_\mathrm{m} h \left(\frac{\partial \eta}{\partial t}\right)^2 + B\left(\frac{\partial^2 \eta}{\partial x^2}\right)^2 + K\eta^2\right) \mathrm{d}x, \end{gathered} \tag{4.1}$$

where u_x and u_y are the fluid perturbations in the x and y directions respectively. In the case of the channel flow, H is the height of the upper channel wall whereas for the open flow, H is the distance above the flexible plate such that,

$$u_y(x, H, t) \to 0. \tag{4.2}$$

The kinetic energy of the flow is evaluated by the first integral of Equation (4.1) whereas the plate kinetic energy is evaluated by the first term of the second integral and the potential energy (comprising the strain and spring potential) is evaluated by the second two terms of the second integral.

To consider the changes in the energy of the system, irrespective of the initial conditions, an energy growth function is defined as,

$$G(t) = \max_{E(0)\neq 0} \frac{E(t)}{E(0)}. \tag{4.3}$$

Following Tsigklifis and Lucey (2013), Ehrenstein and Gallaire (2005) and Åkervik et al. (2008), the disturbances are then constructed as a linear superpo-

sition of the two-dimensional temporal modes,

$$\{X\left(x,y,t\right)\} = \sum_{j=1}^{N} \epsilon_j\left(t\right)\{\hat{X}_j\left(x,y\right)\}, \tag{4.4}$$

where $\epsilon_j\left(t\right) = \exp\left(-ist\right)\epsilon_j\left(0\right)$ for complex eigenvalues S and $\{\hat{X}_j\left(x,y\right)\}$ are the N normalised eigenvectors from the state-space method. The energy growth function, expressed in the basis of the eigenmodes, is then,

$$G\left(t\right) = ||\left[L\right]\exp(\left[\Lambda\right]t)\left[L\right]^{-1}||_2^2, \tag{4.5}$$

where $[\Lambda]$ is a matrix with each diagonal entry having a unique eigenvalue, $\Lambda_{ii} = S_i$, and $[M] = [L]^T[L]$ is the Cholesky decomposition of the Grammian matrix $[M]$ given by,

$$\begin{aligned} M_{ij} &= \frac{1}{2}\int_0^L\int_0^H u_{x,i}u_{x,j}^* + u_{y,i}u_{y,j}^*\mathrm{d}y\mathrm{d}x \\ +\frac{1}{2}\int_0^L \rho_{\mathrm{m}}h\left(\frac{\partial\eta}{\partial t}\right)_i\left(\frac{\partial\eta^*}{\partial t}\right)_j &+ B\left(\frac{\partial^2\eta}{\partial x^2}\right)_i\left(\frac{\partial^2\eta^*}{\partial x^2}\right)_j + K\left(\eta_i\eta_j^*\right)\mathrm{d}x, \end{aligned} \tag{4.6}$$

where * denotes the complex conjugate.

The function G creates an envelope of the maximum growth of energy at a given time, t, and the initial condition that causes this energy growth is:

$$\{X_0\} = [L]^{-1}\{z\}, \tag{4.7}$$

where $\{z\}$ is the right singular vector of the Grammian matrix, $[M]$.

It is then possible to break down the energy into the flow kinetic energy, structural kinetic energy and structural potential energy to consider their contribution to the evolution (in time) of the total energy of the system.

4.1.2 Velocity Perturbation

To calculate the velocity perturbations u_x and u_y, a value of H must first be identified (only for the open flow) and an appropriate grid chosen. From Equation (3.8), it can be seen that the perturbation potential decays with $1/y$. Here it is sufficient to set $H = L$ as any velocity perturbation in the y-direction above this height is negligible, so $H = L$ satisfies Equation (4.2). An N by M grid is formed where N is the discretisation of the lower wall and M is the number of points in the y-direction, spaced evenly between $y = 0$ and $y = H$.

The velocity perturbations at each point on the grid are then given by,

$$u_x = \frac{\partial \phi}{\partial x} \quad \text{and} \quad u_y = \frac{\partial \phi}{\partial y}, \tag{4.8a, b}$$

where ϕ is calculated from Equation (3.8) and where η and $\partial\eta/\partial t$ are given by the eigenvectors calculated from the state-space method.

4.2 Results

The non-dimensional eigenvalues, S', and non-dimensional time, t', are defined by,

$$S' = \frac{S}{S_0} \qquad \text{and} \qquad t' = tS_0, \tag{4.9a, b}$$

where S_0 is the theoretical angular oscillation frequency of the fundamental mode for a plate in vacuo, calculated using Equation (3.50). The system behaviour is also governed by the mass ratio, μ, and the non-dimensional stiffness ratio (non-dimensional flow velocity), Λ^{F}, given by Equations (3.51) and (3.52) respectively.

Although $2N$ eigenvalues are calculated, the only eigenvalues (and corresponding eigenvectors) of interest are the ones that have converged for the discretisation level being used. For this reason, only the 100 eigenvalues with the lowest absolute imaginary part are included in the transient analysis calculations. Although no formal validation is presented for this work, sub-components were validated in Chapter 3 and further validation will be performed throughout the results section by way of comparison with a range of similar investigations.

4.2.1 Open Flow

Simple Elastic Plate

The results presented here use the same system parameters as in Section 3.3.1 with a grid size of $N \times M = 200 \times 200$. The mass ratio of this system is $\mu = 92.3$.

To help understand the non-modal analysis performed here, first the spectrum of eigenvalues calculated from the state-space method is considered. Figures 4.1 (a), (b) and (c) show the four eigenvalues with the smallest absolute imaginary part (although a total of $2N$ eigenvalues are calculated) at non-dimensional flow speeds $\Lambda^{\mathrm{F}} = 32$, 36 and 38 respectively. These flow speeds correspond to $0.8\Lambda^{\mathrm{F}}_{\mathrm{DO}}$, $0.9\Lambda^{\mathrm{F}}_{\mathrm{DO}}$ and $0.95\Lambda^{\mathrm{F}}_{\mathrm{DO}}$ respectively, where $\Lambda^{\mathrm{F}}_{\mathrm{DO}}$ is the divergence-onset flow speed for the open flow $\Lambda^{\mathrm{F}}_{\mathrm{DO}} = 40$. These flow speeds were chosen as it is the small amplitude plate deflections that are being considered, found in the pre-divergence range of flow speeds. The eigenvalues are shown to lie on $S_{\mathrm{R}} = 0$ and this holds true for all the $2N$ eigenvalues calculated. It can be seen that as the flow speed increases, the difference between the oscillation frequency (imaginary

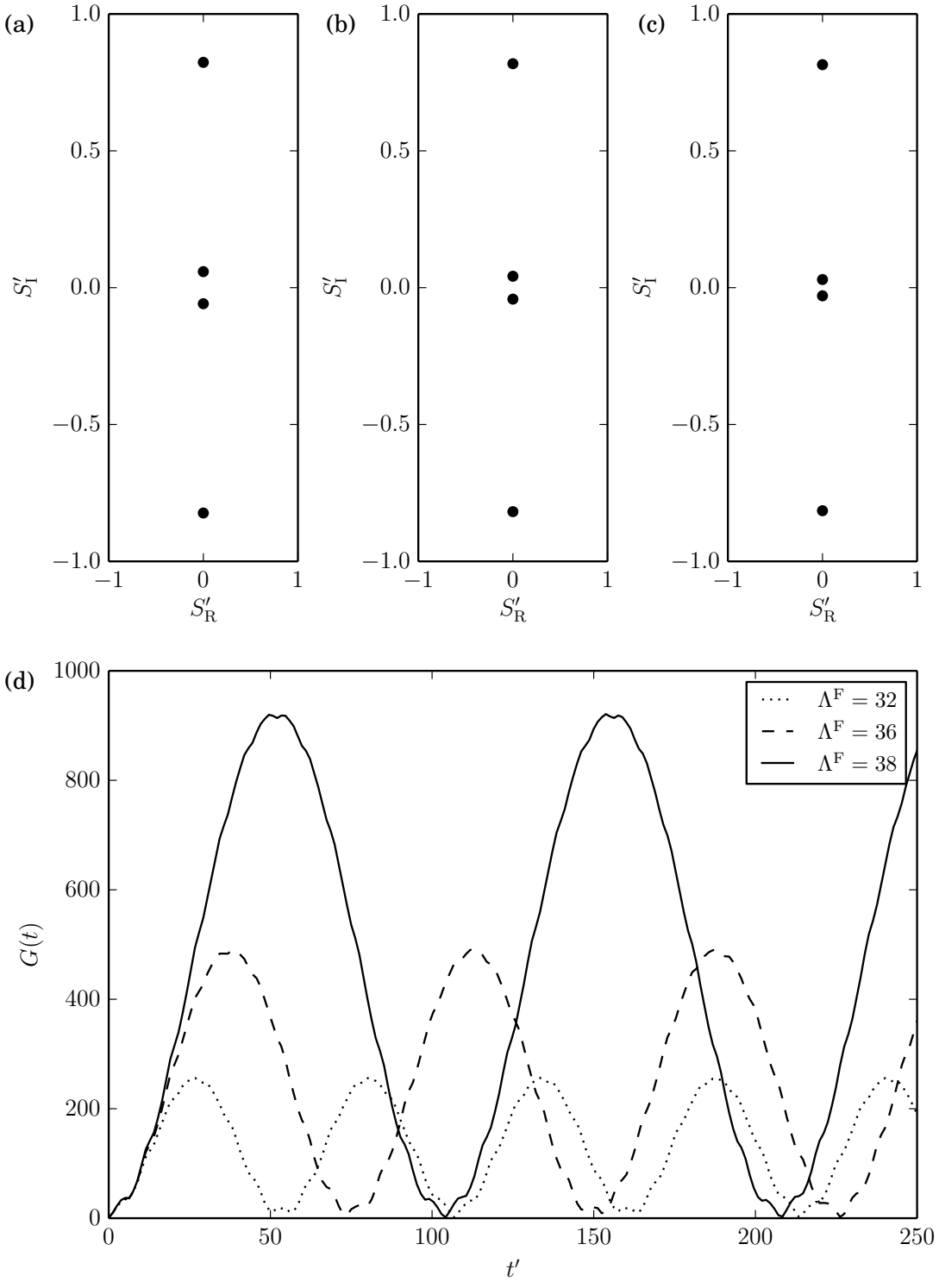

Figure 4.1: The eigen spectrum for a flexible plate without structural damping at: (a) $\Lambda^{\mathrm{F}} = 32$, (b) $\Lambda^{\mathrm{F}} = 36$ and (c) $\Lambda^{\mathrm{F}} = 38$ respectively. (d) Energy growth function $G(t)$ at each corresponding flow speed with non-dimensional time, t'.

eigenvalue) of the lowest two modes and their complex conjugates increases as the lowest mode frequency reduces faster than the second lowest. When the lowest frequency eigenvalue has a zero imaginary value, the real part becomes positive and divergence occurs.

The energy growth function, $G(t)$, given by Equation (4.5), can be seen in Figure 4.1 (d) at the flow speeds corresponding to Figures 4.1 (a), (b) and (c). The energy displays an oscillatory behaviour where the plate alternately extracts and releases energy from the fluid. Similar oscillatory behaviour was also found by Coppola and de Luca (2010) for a pinned-pinned plate in supersonic flow and Schmid and de Langre (2003) for a system with two degrees of freedom. The maximum value of $G(t)$ increases as the flow speed increases and this agrees with the results of Coppola and de Luca (2010). Figure 4.1 (d) is replotted in Figure 4.2 with a logarithmic scale to provide a more convenient comparison with the results of other studies.

Figure 4.3 (a) shows the relationship between the maximum of the energy growth function, $G_{\max}$, as it varies with flow speed. It can be seen that there is

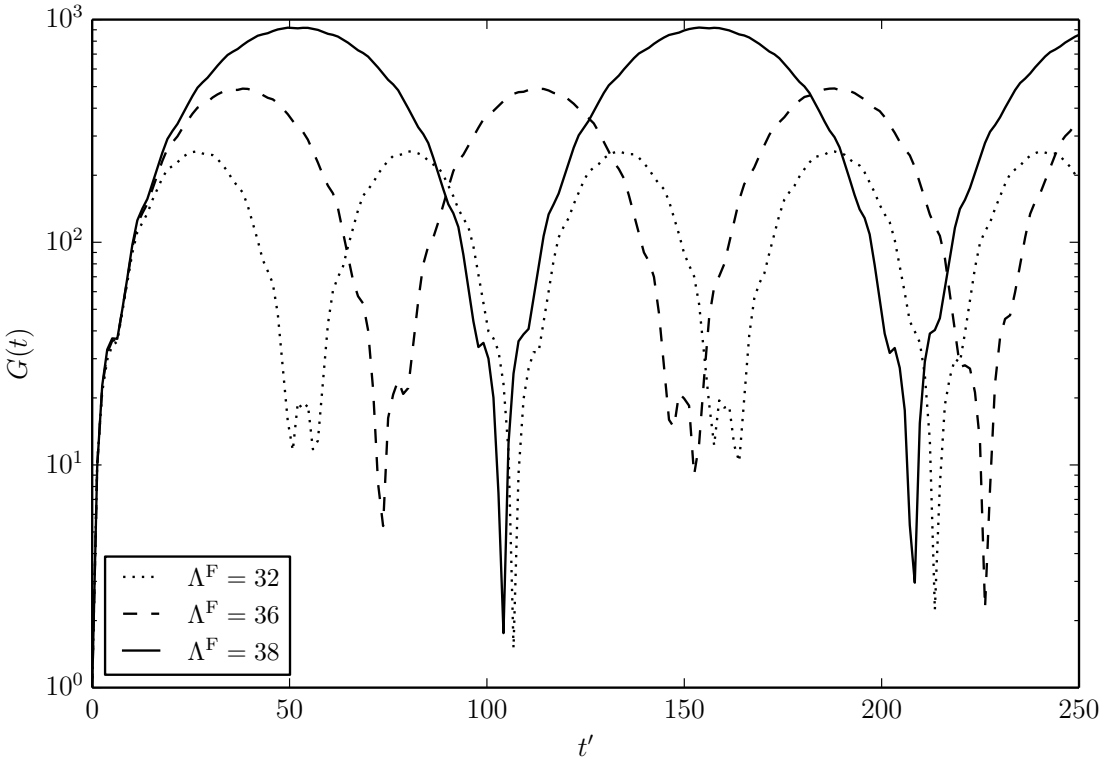

Figure 4.2: Energy growth function $G(t)$ at three different flow speeds with non-dimensional time, t'.

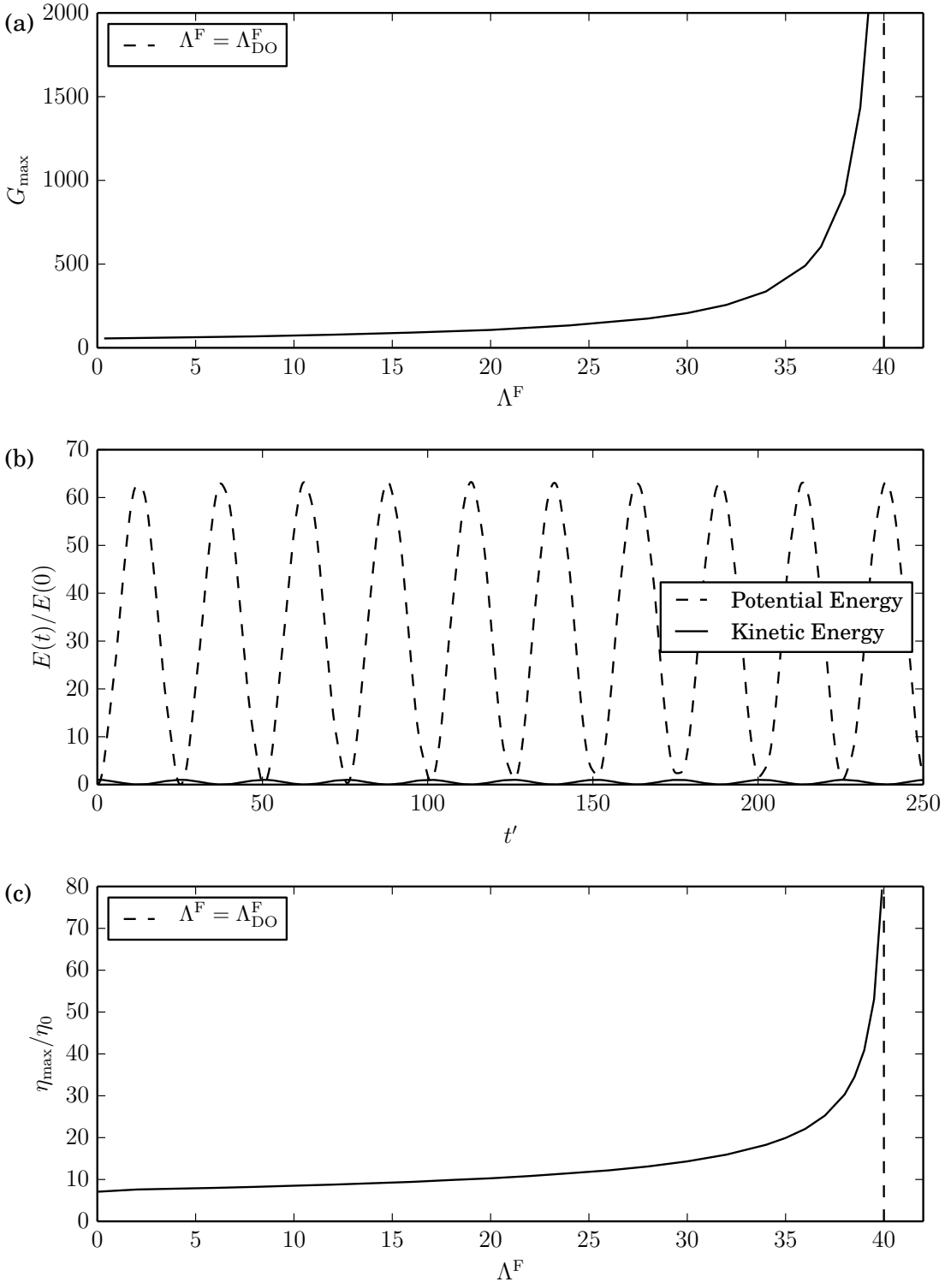

Figure 4.3: (a) Maximum energy growth rate with non-dimensional flow speed, (b) Kinetic and potential energy with non-dimensional time for $\Lambda^F = 5$ and (c) Maximum non-dimensional plate deflection with non-dimensional flow speed.

an asymptote at the divergence-onset flow speed, with $G_{\max}$ becoming infinitely large as it approaches $\Lambda^{\mathrm{F}}_{\mathrm{DO}}$, beyond which exponential growth in time occurs. The results exhibit the same characteristics as Figure 11 in Coppola and de Luca (2010) for a subsonic flow with clamped boundary conditions at the plate ends.

The transient growth of the kinetic and potential energy with time is shown in Figure 4.3 (b) for non-dimensional flow speed $\Lambda^{\mathrm{F}} = 5$. As there is no spring-backing considered here the potential energy is comprised only of the plate's strain energy. It can be seen that the strain energy dominates the energy response. As the plate oscillates, the strain energy grows with the plate deflection, becoming zero when the plate returns to the $y = 0$ position. The kinetic energy is out of phase with the strain energy, having a maximum value when the plate is at a $y = 0$ position and reducing as the plate grows and slows down. The kinetic energy has a zero value when the plate stops to change direction within each oscillation, which is when the strain energy, and plate deflection is greatest. From Chapter 3 (Figure 3.3) it is known that as the flow speed is increased, the oscillation frequency of the plate reduces, becoming zero at divergence onset, so for this reason the kinetic energy of the system is smaller at faster flow speeds, becoming negligible just before divergence onset. This reduction in oscillation frequency also causes the beat frequency of the energy growth rate to reduce and therefore the beating time period for the energy growth function increases with Λ^{F} which can be seen in Figure 4.1 (d). The strain energy, however, increases with flow speed.

While Figure 4.3 (b) may appear to be like the divergence instability demonstrated in Chapter 3, it is the nonlinear induced tension which acts as a restoring force for the divergence instability which is not modelled in this linear analysis. The plate is stable, but with transient growth, and can be considered to be a type A behaviour using the classifications of Schwartz et al. (2009) where type A is stable with transient growth in a linear system, type B is a stable with transient growth in a nonlinear system and type C is a by-pass transition where transient growth triggers the flutter instability below the critical flow speed.

By considering the maximum growth in potential energy at any given flow speed, it is possible to consider the corresponding growth of plate deflection,

$\eta_{\max}/\eta_0$, shown in Figure 4.3 (c), where $\eta_{\max}$ is the peak amplitude of the plate at its maximum deflection and η_0 is the amplitude of the plate at its initial position. From Figure 4.3 (a), it is expected that the flexible plate deflections would become infinitely large as the flow speed approaches divergence onset, so clearly large (nonlinear) deflections are possible in the pre-divergence range of flow speeds. However even for lower flow speeds, the maximum plate deflection has the potential to grow large enough to necessitate full nonlinear calculations, dependent on the initial deflection given.

The non-dimensional beating period of the energy growth function, T', is plotted in Figure 4.4 (a) as it varies with the non-dimensional flow speed, further demonstrating the increase in beating period with Λ^{F} that was seen in Figure 4.1

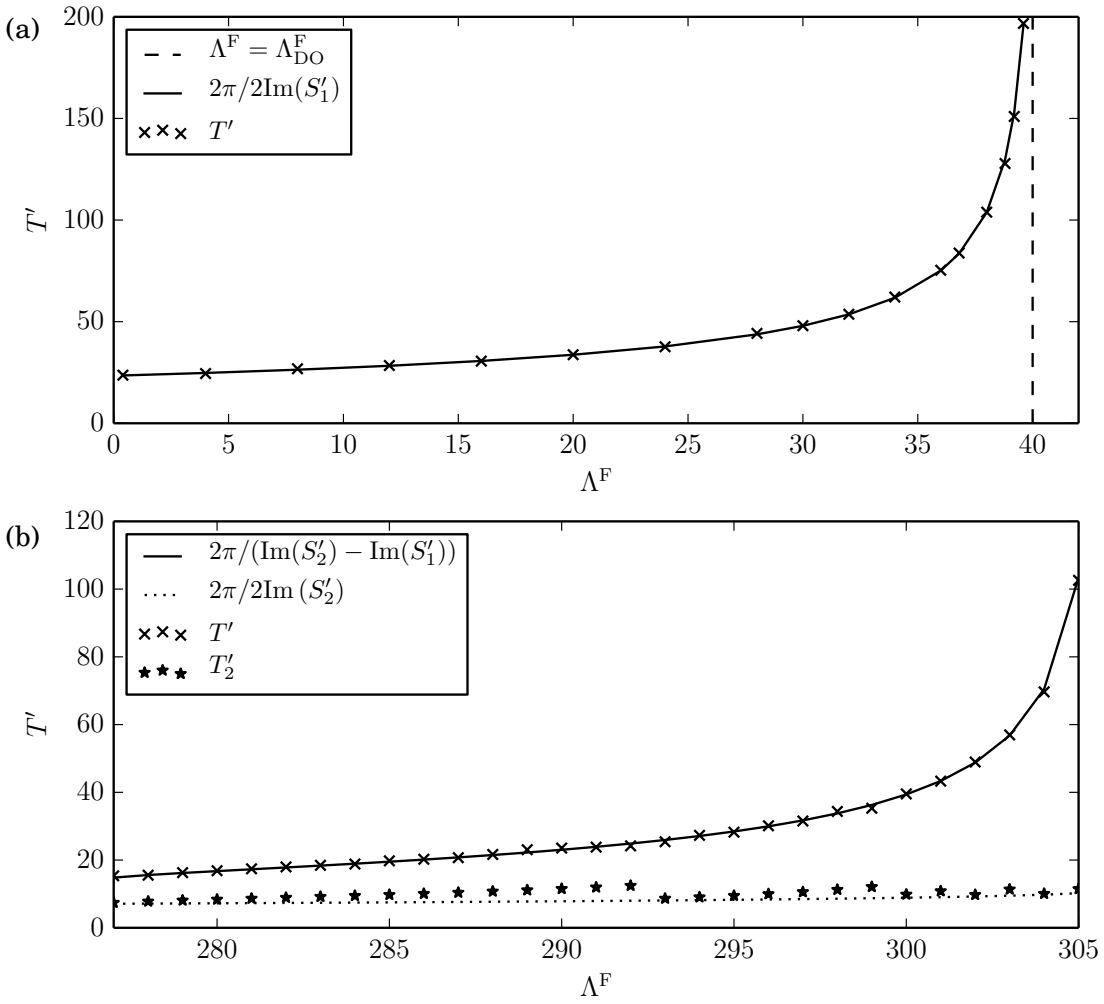

Figure 4.4: Beating period of the energy growth function with non-dimensional flow speed for: (a) pre-divergence and (b) divergence recovery.

(d). This shows a similar trend to that shown in Figure 4.1 (a) for $G_{\max}$. That the beating period increases with Λ^{F} and approaches infinity at instability onset, agrees with the results of Coppola and de Luca (2010). They state that when modelling a clamped-clamped plate in subsonic flow using a modelling technique similar to that of Kornecki et al. (1976), the beating period scales with the spacing between the lowest imaginary eigenvalue and its complex conjugate, $2\,\mathrm{Im}\,(S_1')$. Figures 4.1 (a), (b) and (c) show that this spacing decreases with increasing flow speed. Also plotted on Figure 4.4 (a) is $2\pi/2\,\mathrm{Im}\,(S_1')$, which agrees almost exactly with the beating period found from the transient growth analysis.

Coppola and de Luca (2006) and Coppola and de Luca (2010) found that for a pinned-pinned beam in a supersonic flow, the beating period and the difference between the imaginary part of the lowest two eigenvalues, $(\mathrm{Im}\,(S_2') - \mathrm{Im}\,(S_1'))$, are related by $T' = 2\pi/\left(\mathrm{Im}\,(S_2') - \mathrm{Im}\,(S_1')\right)$. In the case of supersonic flow, the first instability encountered is modal-coalescence flutter and the difference between the lowest two eigenvalues decreases as flow speed increases. In the present work $(\mathrm{Im}\,(S_2') - \mathrm{Im}\,(S_1'))$ increases with flow speed. However, when the transient growth in the divergence-recovery range of flow speeds (predicted in Section 3.3.1, Figure 3.4) is considered, a better comparison can be given as in this case the difference between the imaginary part of the two lowest eigenvalues is decreasing as the frequencies of mode 1 and mode 2 approach each other, and the system will lose its stability to modal-coalescence flutter.

The beating period for the divergence-recovery range of flow speeds is shown in Figure 4.4 (b) and when compared with the Coppola and de Luca (2006) prediction of $T' = 2\pi/\left(\mathrm{Im}\,(S_2') - \mathrm{Im}\,(S_1')\right)$, the two agree well. The lowest two eigenvalues calculated from the state-space method, for three flow velocities within the divergence-recovery range are shown in Figure 4.5 (a), (b) and (c). It can be seen that as the flow speed increases, approaching modal-coalescence onset, the difference between the imaginary part of the eigenvalues decreases.

The energy growth function for two flow velocities just before modal-coalescence flutter onset is plotted in Figure 4.5 (d) with non-dimensional time. The morphology of the energy growth function at divergence-recovery flow speeds is different to that demonstrated in the pre-divergence range of flow speeds shown in Figure 4.2.

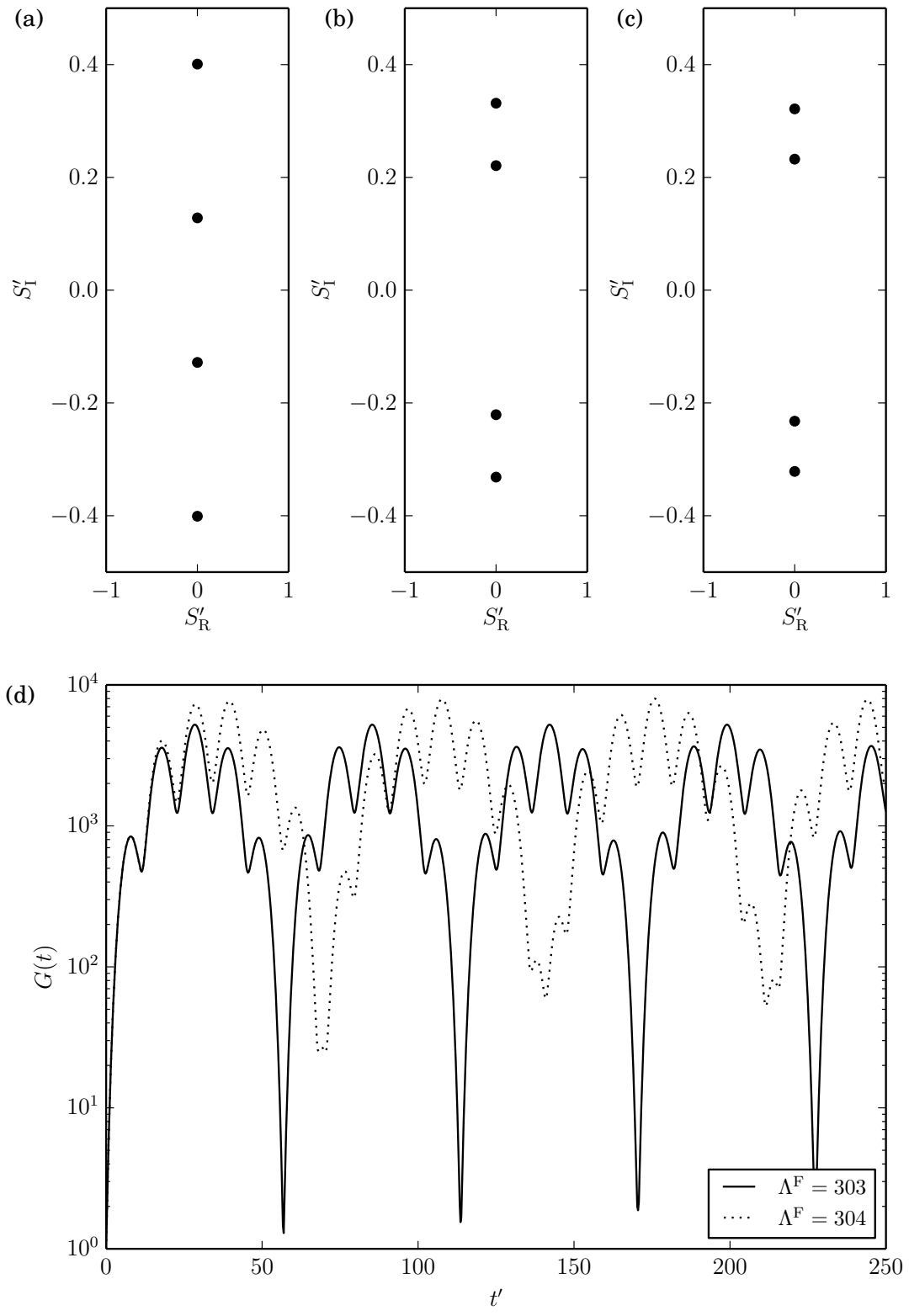

Figure 4.5: The eigen spectrum for a flexible plate without structural damping at: (a) $\Lambda^{\mathrm{F}} = 290$, (b) $\Lambda^{\mathrm{F}} = 303$ and (c) $\Lambda^{\mathrm{F}} = 304$ respectively. (d) Energy growth function $G(t)$ at $\Lambda^{\mathrm{F}} = 303$ and $\Lambda^{\mathrm{F}} = 304$ with non-dimensional time, t'.

Although the energy growth function still has the large oscillations, the beating period of which was plotted in Figure 4.5 (b), another smaller energy oscillation can be seen which becomes more apparent as the flow speed approaches modal-coalescence onset. This smaller oscillation is due to the increasing influence of the mode with the second lowest frequency. The beating period of this mode two oscillation, T_2', approximately scales with the spacing between the imaginary part of second mode and its complex conjugate, $2\,\mathrm{Im}(S_2')$, so that $T_2' \approx 2\pi/2\,\mathrm{Im}(S_2')$. The beating period of mode 2 has also been plotted on Figure 4.4 (b) along with $2\pi/2\,\mathrm{Im}(S_2')$. Although T_2' and $2\pi/2\,\mathrm{Im}(S_2')$ are not always in exact agreement, this is due to the number of small oscillations that are present in each large oscillation of the growth function. Up to $\Lambda^{\mathrm{F}} = 292$ there are two small oscillations present in each large oscillation and there is a greater disparity between T_2' and $2\pi/2\,\mathrm{Im}(S_2')$ with increasing flow speed. At $\Lambda^{\mathrm{F}} = 293$, the mode of the small oscillations has increased to 3, improving the agreement of the two results. This pattern is repeated as the number of small oscillations per large oscillation increases as the flow speed approaches modal-coalescence onset.

Damped Plate

The system parameters used here are the same as for the plate without structural damping but with a dashpot-type structural damping of $d = 750$ Ns/m^3. The mass ratio for this system is $\mu = 92.3$.

When considering the spectrum of eigenvalues, Figures 4.6 (a), (b) and (c) show the four eigenvalues with the smallest absolute imaginary part at non-dimensional flow speeds $\Lambda^{\mathrm{F}} = 32$, 36 and 38 respectively to be compared with Figures 4.1 (a), (b) and (c). In this case the eigenvalues have a non-zero real part, the lowest of which approaches zero as the flow speed increases, becoming positive in the divergence range of flow speeds. The difference between the lowest two eigenmodes again increases as the lowest mode decreases at a faster rate than the second mode. This behaviour can also be seen in Figure 3.6.

Figure 4.6 (d) shows the energy growth rate, G, at flow speeds corresponding to those in Figures 4.6 (a), (b) and (c). When compared with Figure 4.2, the oscillatory behaviour is still present but inclusion of structural damping reduces

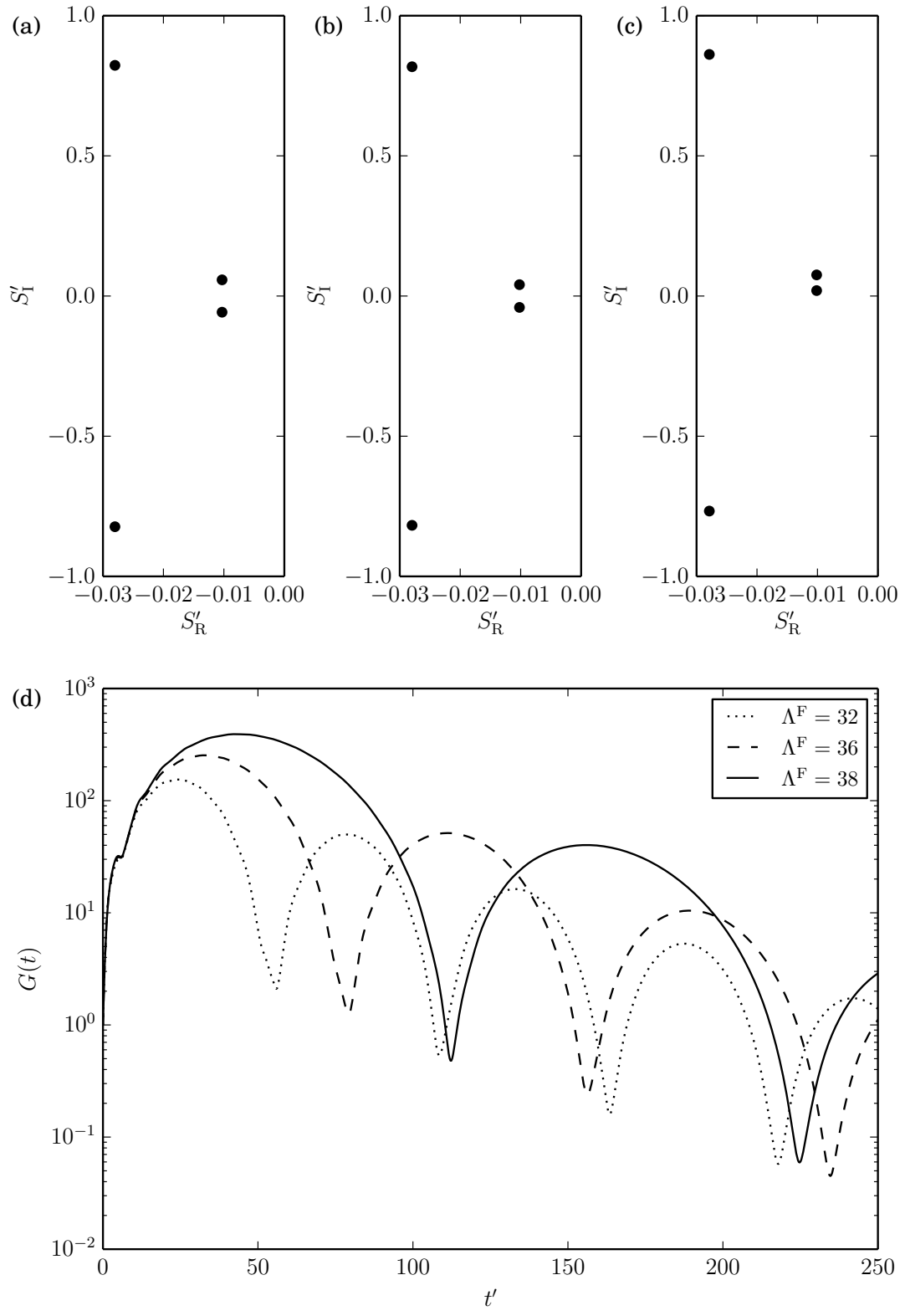

Figure 4.6: Eigen spectrum for a flexible plate with $d = 750$ Ns/m^3 at: (a) $\Lambda^{\mathrm{F}} = 32$, (b) $\Lambda^{\mathrm{F}} = 36$ and (c) $\Lambda^{\mathrm{F}} = 38$ respectively. (d) Energy growth function $G(t)$ at each corresponding flow speed with non-dimensional time, t'.

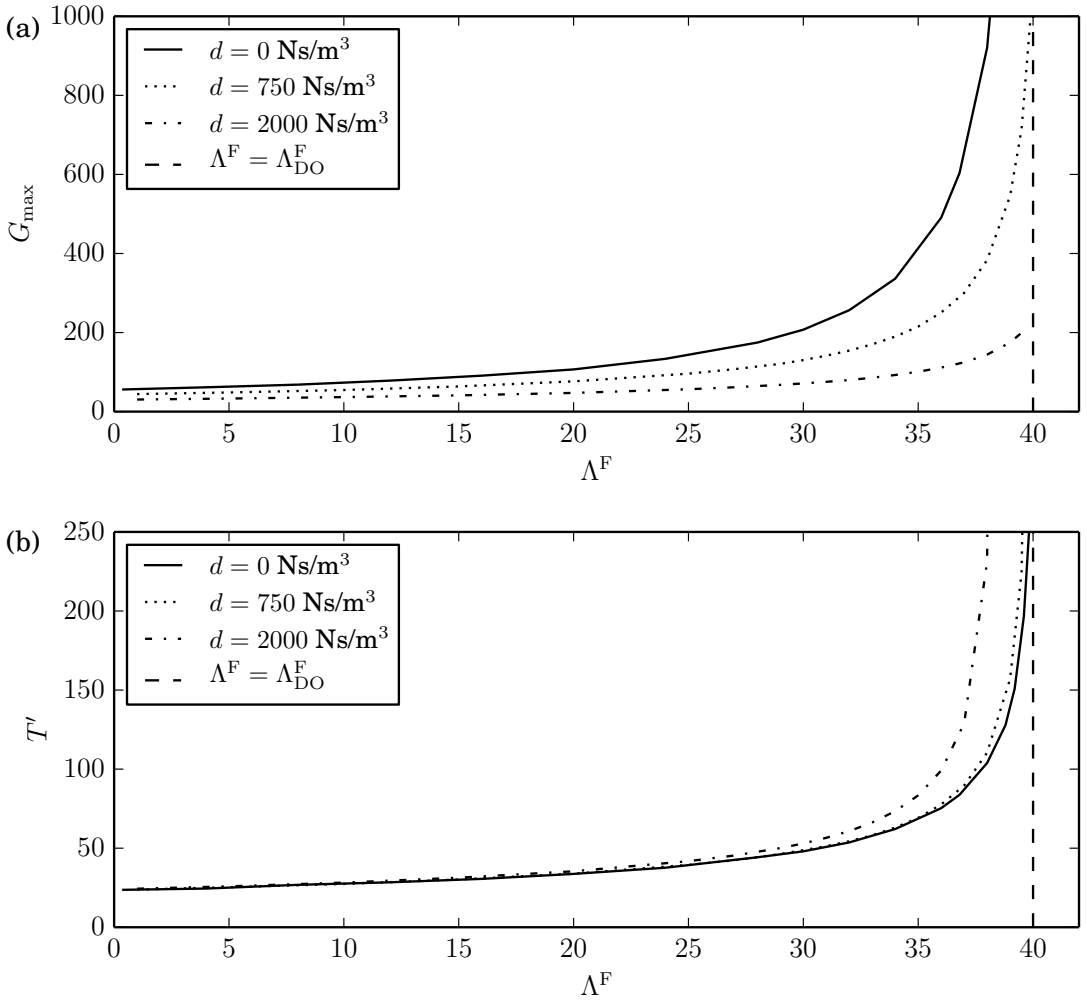

Figure 4.7: (a) Maximum energy growth and (b) Beating period of the energy growth function as they vary with non-dimensional flow velocity for three levels of structural damping.

the growth rate with each oscillation until it is damped down to $G(t) = 0$.

The maximum value of G, $G_{\max}$, as it varies with flow speed is shown in Figure 4.7 (a) as the dotted line. Also plotted on Figure 4.7 (a) are the cases where $d = 0$ Ns/m^3 and $d = 2000$ Ns/m^3. For all three levels of damping, the energy growth function increases with Λ^{F}. The presence of damping reduces the value of $G_{\max}$ for any given flow speed and it is demonstrated that higher levels of damping effect a further reduction of $G_{\max}$, as would be expected. When no damping is present and when $d = 750$ Ns/m^3, $G_{\max}$ appears to asymptote to infinity at the critical divergence-onset speed, however when $d = 2000$ Ns/m^3, $G_{\max}$ reaches a finite value at instability onset.

Figure 4.7 (b) shows the beating period of the energy growth oscillations with flow speed at the same levels of damping as in Figure 4.7 (a). The beating period appears to grow at a slightly faster rate with increasing flow speed when damping is included. The effect that damping has on T' is less significant than the effect on $G_{\max}$. At a zero flow speed the beating periods all converge to the $d = 0$ Ns/m^3 case whereas damping causes a noticeable decrease in $G_{\max}$ for all values of flow speed including $\Lambda^{\mathrm{F}} = 0$.

Effect of Mass Ratio

For the simple elastic and damped plates the mass ratio is fixed at $\mu = 92.3$. In this section, the effect of varying the mass ratio of a simple elastic plate without structural damping is considered. The system parameters are the same as those used in Section 4.2.1 but with varying fluid density, ρ_f. Mass ratios of $\mu = 2$, 5, and 10 are chosen to allow a convenient comparison with the results of Coppola and de Luca (2010) and the corresponding fluid densities used are $\rho_f = 21.7$ kg/m^3, 54.2 kg/m^3 and 108.3 kg/m^3 respectively.

The maximum of the energy growth function as it varies with non-dimensional flow speed is shown in Figure 4.8 (a) for three different mass ratios. As the mass ratio is reduced, the maximum of the energy growth function also decreases. From

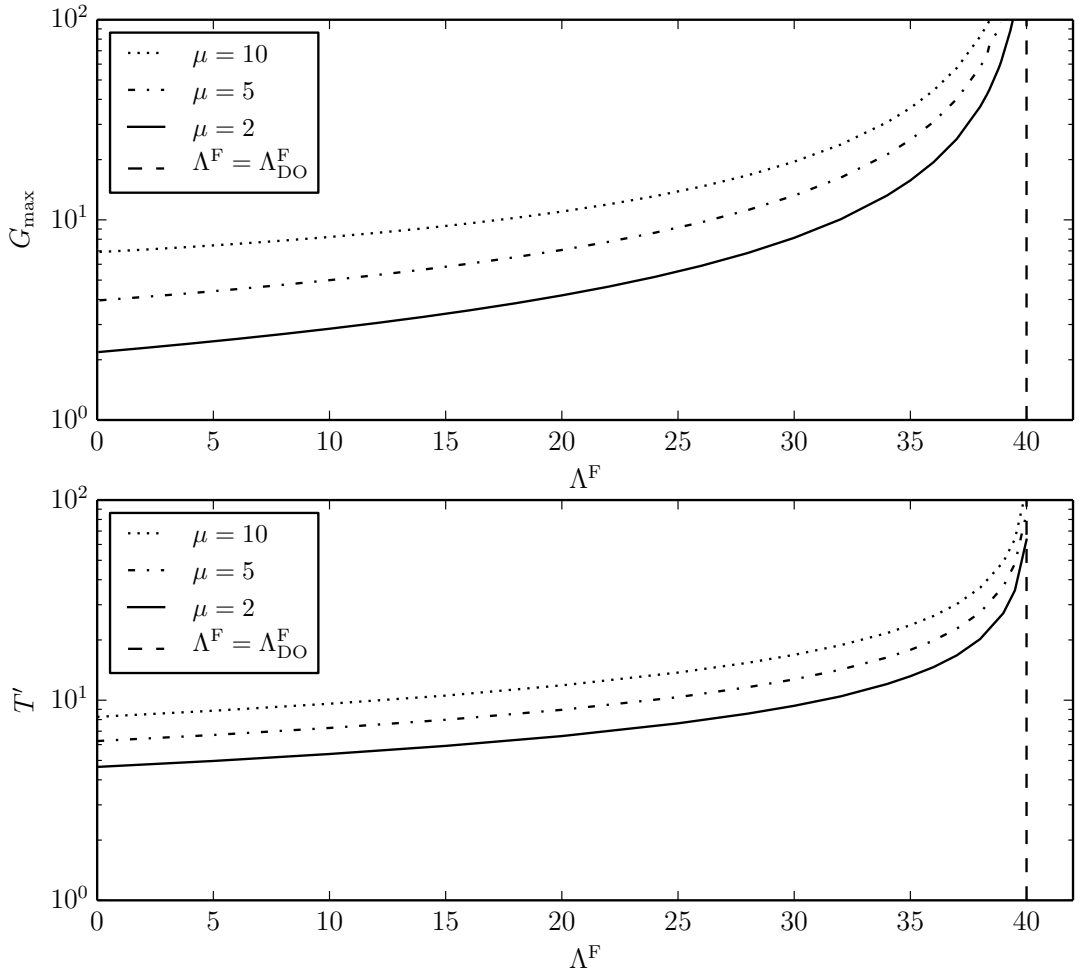

Figure 4.8: (a) Maximum energy growth function and (b) Beating period with non-dimensional flow speed at three different mass ratios.

this it can be inferred that the maximum amplitude of the plate disturbance also reduces. The same effect is seen in Figure 11 (a) from Coppola and de Luca (2010) when considering a subsonic flow, which is opposite to their findings for a supersonic flow. This occurs because reducing the mass ratio is equivalent to reducing the fluid density, and so the system is approaching the in vacuo case. In the in vacuo system all modes are orthogonal and so no transient growth occurs. The mass ratio can also be altered by changing the length of the flexible plate, L. Reducing the length of the plate increases the oscillation frequency of the plate, S'_{I}. This is demonstrated in the eigen-analysis of Chapter 3 (Figure 3.7). At a higher frequency there is less interaction between the modes. Figure 4.8 (a) also demonstrates that regardless of the mass ratio, $G_{\max}$ will always asymptote to infinity at $\Lambda^{\mathrm{F}}_{\mathrm{DO}}$. This is because divergence is a static instability and at divergence onset the oscillation frequency is zero, so the divergence-onset speed is independent of mass ratio. This is also demonstrated in Figure 3.7.

The beating period of the energy growth oscillations is shown in Figure 4.8 (b) as it varies with non-dimensional flow speed for the same three mass ratios shown in Figure 4.8 (a). As the mass ratio is increased, the beating period also increases for a fixed flow speed which is another effect of the added mass in the system. This also agrees with the results of Coppola and de Luca (2010).

4.2.2 Channel Flow

The energy growth function when a flexible insert comprises one wall of a channel flow is now considered using the same illustrative parameters for the simple plate in Section 4.2.1 with a mass ratio, $\mu = 92.3$ and rigid wall lengths $L_\mathrm{r} = 2L$. The energy growth function as it varies with non-dimensional time is shown in Figure 4.9 at $H/L = 0.1$, 0.5 and ∞ (the open flow case) when $\Lambda^\mathrm{F} = 5$. It can be seen that the morphology of the energy growth function does not alter with non-dimensional channel height, but that decreasing H/L causes an increase in the maximum growth that occurs, and an increase in the beating period. This is a further effect of an increase in hydrodynamic stiffness caused by the increased gradient of streamline curvature that occurs as the channel is made narrower, as discussed in Section 3.3.1.

This increase in the energy growth maximum is also demonstrated in Figure 4.10 (a), where for the same three channel heights shown in Figure 4.9, G_max is plotted against Λ^F. In each case the energy growth maximum becomes infinitely

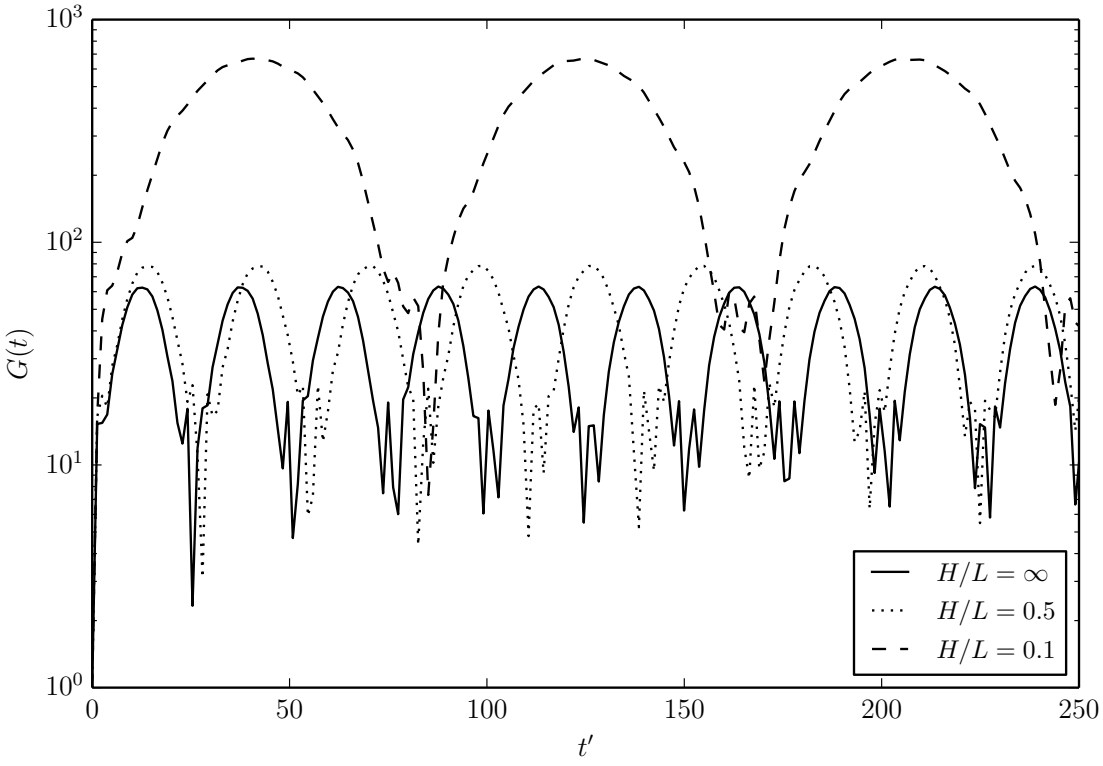

Figure 4.9: Energy growth function at $\Lambda^\mathrm{F} = 5$ for the open flow and at two different channel heights.

large at divergence onset, and the asymptotic values for instability onset for each channel height agree with those predicted by the linear theory of Channel 3.

The beating period as it varies with non-dimensional flow speed is plotted in Figure 4.10 (b) for the $H/L = 0.1$, 0.5 and ∞ cases. This shows the increase of T' as the channel is made narrower that was seen in Figure 4.9. The asymptotic values of Λ^{F} also agree with the onset of divergence predicted by the linear theory, which are marked on Figure 4.9 by the dashed lines.

The streamlines from Equation (4.8) are shown in Figure 4.11 (a) for an open flow and Figure 4.11 (b) for a channel flow with $H/L = 0.25$. This demonstrates how the upper channel wall effects the flow through the channel. In the open

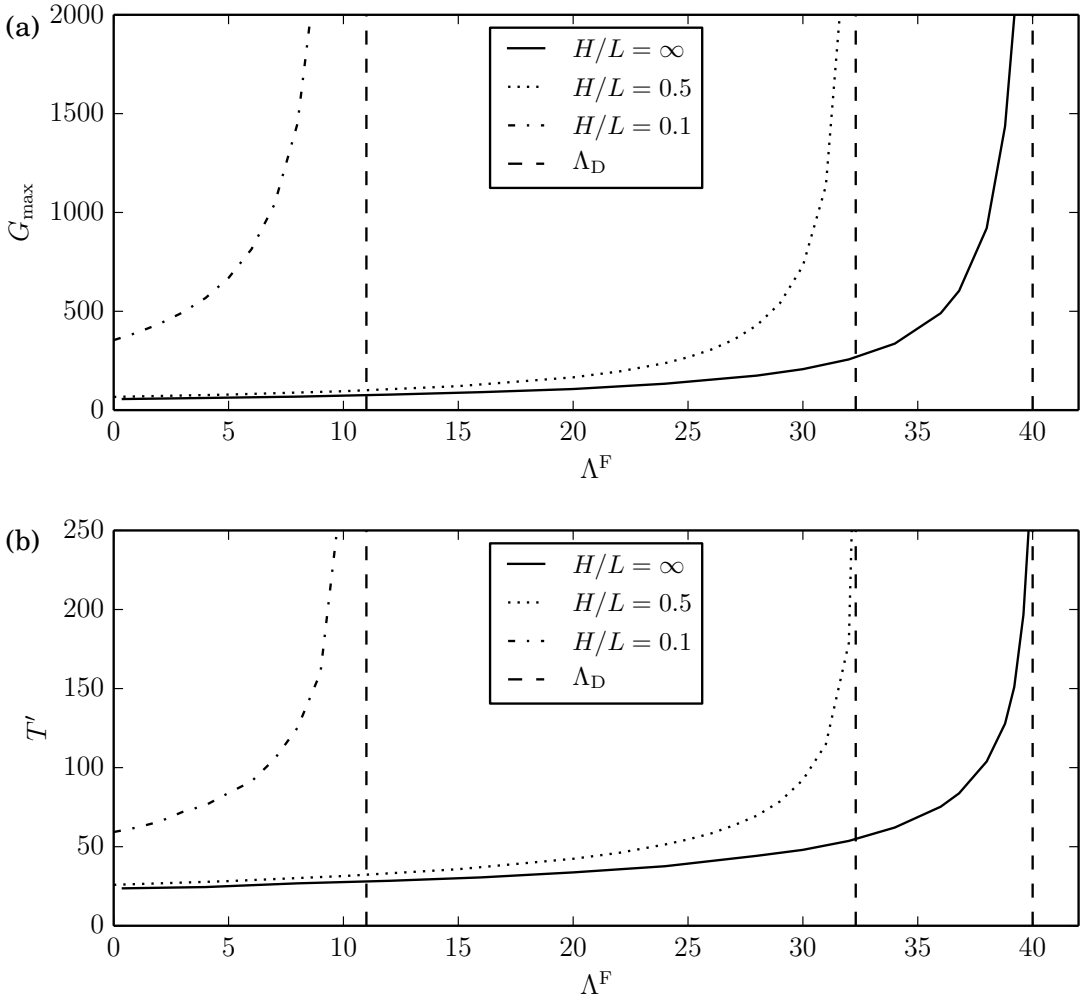

Figure 4.10: (a) Maximum energy growth rate and (b) Beating period with non-dimensional flow velocity for three different non-dimensional channel heights. Dashed lines: divergence onset predicted by the linear theory of Chapter 3.

flow case, the streamlines have an infinite space over which the curvature of the streamline will tend towards zero and it can be seen that at a distance of $y/L = 0.25$ there is still a noticeable curvature. For the channel case however, the streamlines are forced to have a zero curvature at the upper channel wall, therefore increasing the gradient of the curvature. This causes the increase in pressure, via the hydrodynamic stiffness (first term on the right-hand side of Equation (3.11)), for narrow channels when compared with wide channels or the open flow, which causes not only an increase in the transient growth that is possible but also the reduction in instability onset speed discussed in Chapter 3.

The transient growth that can occur in the system is therefore dependent not only on flow velocity and mass ratio but also on channel height.

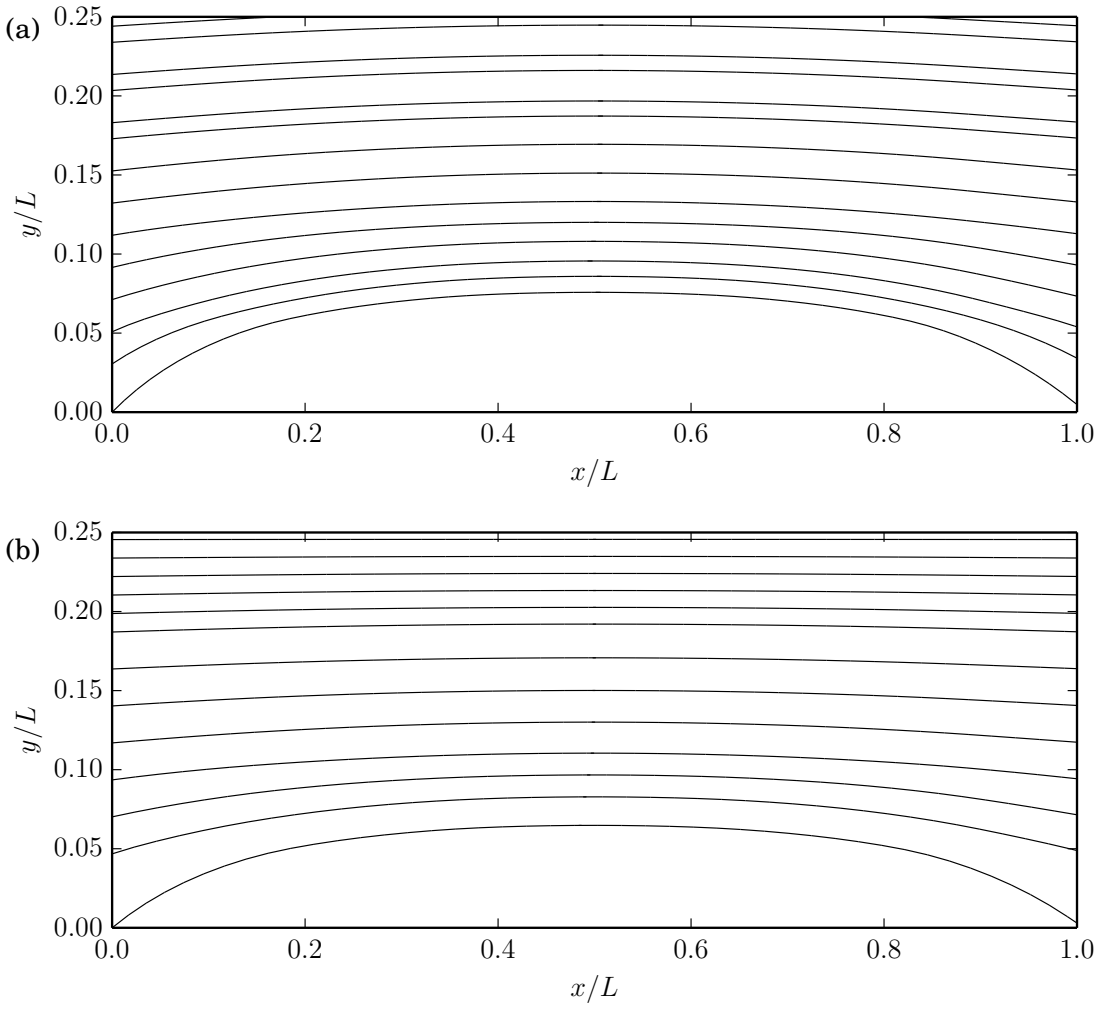

Figure 4.11: Streamlines for; (a) an open flow and (b) a channel with channel height $H/L = 0.25$.

4.3 Summary

A theoretical investigation of the transient growth of global energy of a potential flow over a finite compliant wall has been conducted using eigen-analysis within the non-normality of the system. Only flow velocities in the neutrally stable range are considered as the aim here is to establish whether nonlinear amplitudes may be attained by a means other than divergence or modal-coalescence flutter.

An energy growth function is defined and calculated for a variety of flow speeds. This shows oscillatory behaviour as the plate extracts/releases energy from/into the fluid. The energy growth function has a maximum amplitude and beating period that tends to infinity as the flow velocity approaches divergence onset. The plate has the potential to reach nonlinear amplitudes for the whole range of flow speeds.

It is found that the total energy is mostly comprised of the plate strain energy, and that as the flow speed approaches divergence onset, the system kinetic energy reduces because divergence is a static instability. The effect of damping has been characterised. The inclusion of a dashpot-type structural damping reduces the maximum of the energy growth function significantly and reduces the beating period marginally.

In the divergence-recovery range of flow speeds, the beating frequency is found to be related to the difference between the oscillation frequency of the two lowest eigenmodes which agrees with results of previous investigations. This does not hold true for the pre-divergence range of flow speeds wherein the same trend is seen for the beating period, but the difference in the oscillation frequencies increases with flow speed. In this case the beating period is related to the difference between the lowest frequency and its complex conjugate.

The effect of mass ratio is considered and it is found that reducing the mass ratio reduces the maximum energy growth. This occurs because a lower mass ratio may be achieved by reducing the fluid density, so the system is approaching the in vacuo system, where all the modes are orthogonal. Systems with lower mass ratio are relevant to air flow over metal/glass panels or higher density fluids such as water interacting with short metal/glass panels.

Finally, the transient growth of a finite flexible plate comprising one wall of

a channel flow is investigated with attention to the effect of the proximity of the upper channel wall. It is found that as the non-dimensional channel height is reduced, the maximum energy growth rate, and the beating period of the energy growth both increase. This is a further effect of the increased hydrodynamic stiffness caused by the increased gradient of the streamline curvature of a narrow channel compared with a wide channel.

This investigation demonstrates that large amplitude disturbances can occur in a neutrally stable system. The maximum growth of energy in the flexible insert is dependent on the flow speed, mass ratio and channel height of the system and that, in the absence of nonlinear effects, energy growth will become infinitely large at flow speeds close to instability onset.

Chapter 5

Nonlinear Fluid-Structure Interactions of a Fluid-Loaded Flexible Insert

Chapter 3 investigated the linear fluid-structure interactions of a wide range of different flexible insert types in an open and channel flow, with particular attention paid to predicting the stability bounds and the effect of the proximity of an upper channel wall on these stability bounds. Whereas Chapter 4 considered transient growth as a means to attain large amplitude deflections of a flexible insert at flow speeds before instability occurs as predicted by Chapter 3. This Chapter seeks to investigate the behaviour of an unstable flexible insert within the divergence range of flow speeds where the large amplitude deflections induced by the flow, grow from an initial small disturbance.

The linear approximations and methods used in Chapter 3 are no longer appropriate for divergence-induced large amplitude deflections. In this chapter full nonlinear numerical simulations are developed and run following the method of Lucey et al. (1997) whereby a finite-difference method is coupled with a boundary element method. In addition, the mean-state amplitude of the insert, which is the settled buckled state when structural damping is included, is found using a time-independent iterative method which is compared with a theoretically derived equation for the open flow case.

The methods used are detailed, followed by a validation of the nonlinear

numerical simulations in the open flow and small amplitude numerical simulations in a channel flow. A range of results are presented for both the open and channel geometries with emphasis on the maximum amplitude that occurs from nonlinear oscillations. Although inclusion of flow separation effects such as vortex shedding would be valuable to improve the understanding of the system, inclusion of these features is considered to be out of the scope of this research and the consideration of the mean and maximum deformation is valuable without their inclusion as this gives a measure of the channel blockage when the insert is unstable. The effect of a uniform external pressure applied to the insert is also considered along with the frequency of the nonlinear oscillations.

5.1 Method

5.1.1 Governing Equations

Structural Mechanics

When large deflections are considered, Equation (3.1) is extended to;

$$\rho_{\mathrm{m}} h \frac{\partial^2 \eta}{\partial t^2} + d\frac{\partial \eta}{\partial t} + B\frac{\partial^4 \eta}{\partial x^4} + K\eta - T_{\mathrm{I}}\frac{\partial^2 \eta}{\partial x^2} = -\Delta p(x, y, t), \tag{5.1}$$

where the tension term, T_{I}, is a nonlinear induced tension given by,

$$T_{\mathrm{I}} = \frac{Eh}{L(1-\nu^2)} \int_0^L \left[\left(1 + \left(\frac{\partial \eta}{\partial x} \right)^2 \right)^{\frac{1}{2}} - 1 \right] dx. \tag{5.2}$$

For linear deflections (small η), the induced tension is negligible and hence it can be neglected in the linear structural mechanics of Chapter 3. However, induced tension increases with η, so for large (nonlinear) deflections, this term must be included. Induced tension serves as a restoring force, the effects of which can be seen in the unstable (diverging) systems shown in the results of Section 5.3.

Flow Solution and Pressure

In the linear model, the source/sink singularities were assumed to lie on the undisturbed plane and this is exact in the limit of $\eta \to 0$ as the linear deformation

assumed all perturbations are vanishingly small. For large deflections however, this approximation is no longer valid. To ensure correct results, the source/sink singularities must lie on the deformed flexible insert. The linear approximation allows for the influence coefficients to only be calculated once and the pressure calculations are simplified. However for the fully nonlinear fluid mechanics, the normal, tangential and perturbation influence coefficients must be calculated with every time step to ensure that the singularities move with the insert deflections. Calculations of the influence coefficients are detailed in Section 3.1.3.

The disturbance normal velocity, tangential velocity and velocity potential are respectively given by Equations 3.9 (a), (b) and (c). The source/sink singularity strengths are calculated by applying the no-flux boundary conditions of Equations (3.6) and (3.7) at the fluid-surface interface for the flexible and rigid portions of the insert, which is,

$$I^N \sigma = U \sin\alpha + u_N, \tag{5.3}$$

where α is the angle of each panel with the horizontal given by,

$$\alpha_i = \tan^{-1}\left(\frac{\eta_i - \eta_{i-1}}{\delta x}\right) \approx \left(\frac{\eta_i - \eta_{i-1}}{\delta x}\right), \tag{5.4}$$

to second-order accuracy in η for each panel i, where $\delta x = L/N_\mathrm{f}$.

The Bernoulli Equation (3.5) is now written,

$$\Delta p = 0.5\rho_\mathrm{f}\left(U^2 - \left(U\cos(\alpha) + u_T\right)^2 - u_N^2\right) - \rho_\mathrm{f}\frac{\partial\phi}{\partial t}, \tag{5.5}$$

where,

$$\frac{\partial\phi}{\partial t} = I^\Phi\frac{\partial\sigma}{\partial t} + \sigma\frac{\partial I^\Phi}{\partial t}. \tag{5.6}$$

This allows the fluid pressure from Equation (5.5) to be matched with the surface pressure from Equation (5.1) at the fluid-solid interface.

5.1.2 Coupling Methods and Numerical Simulation

Time stepping numerical simulations are performed which follow the same method as used by Lucey and Carpenter (1992) for small (linear) deflections and by Lucey et al. (1997) for large (nonlinear) deflections.

As for the linear state-space method in Chapter 3, the pressure is matched at the fluid-solid boundary giving a single equation,

$$\{\ddot{\eta}\} = [B]^{-1} \{F(\dot{\eta}, \eta)\}, \tag{5.7}$$

where $[B]$ is a matrix given by,

$$[B] = \rho_{\mathrm{m}} h [I] - \rho_{\mathrm{f}} \left[I^{\Phi}\right] \left[I^{N}\right]^{-1} \cos\{\alpha\}, \tag{5.8}$$

and $\{F\}$ is a vector given by,

$$\{F\} = -\{\Delta p(\dot{\eta}, \eta)\} - d\{\dot{\eta}\} - B[D_4]\{\eta\} - K\{\eta\} + T_{\mathrm{I}}[D_2]\{\eta\}. \tag{5.9}$$

The flexible insert is given an initial displacement of the form,

$$\eta = \eta_0 \sin(\pi x), \tag{5.10}$$

for a specified initial amplitude η_0, and a three-point implicit time stepping routine, with a time step size of δt is performed, using the time-differencing equations,

$$\eta^{t+\delta t} = \frac{1}{3}\left(2\delta t \dot{\eta}^{t+\delta t} + 4\eta^{t} - \eta^{t-\delta t}\right), \tag{5.11a}$$

$$\dot{\eta}^{t+\delta t} = \frac{1}{3}\left(2\delta t \ddot{\eta}^{t+\delta t} + 4\dot{\eta}^{t} - \dot{\eta}^{t-\delta t}\right). \tag{5.11b}$$

Equations (5.7) and (5.11) are iterated to calculate η, $\dot{\eta}$ and $\ddot{\eta}$ at each mass point, until numerical convergence is achieved. The Von-Neumann condition must be satisfied which ensures that the time step is sufficiently small for a given panel length, to maintain a neutrally stable numerical scheme without numerical error, (Smith, 1986). The size of time step used in each simulation is therefore dependent upon the discretisation level used. In this work a nonlinear approximation is used whereby the influence coefficients are calculated every a time steps depending on the size of the time step. It will be demonstrated in Section 5.2 that this provides sufficient accuracy as there are only very small changes in the displacement and velocity of the insert with each time increment.

In the case of the channel flow, an extra iterative loop is added to the simulation program at each time step to ensure that conservation of mass is maintained when the channel is constricted, by assessing the flow velocity through the channel

cross-section. For the range of channel heights and maximum deflections considered in this work, the extra iterative loop is found to have a negligible effect, but when the maximum deflection relative to channel height is very large its inclusion is necessary, although it is noted that in this case it would no longer be suitable to ignore the viscous effects and that alternative modelling techniques should be considered.

5.1.3 Theoretical Investigation

To complement the numerical simulations, a theoretical investigation is developed. Numerical simulations from this work, and from Lucey et al. (1997), show that in the divergence range of flow speeds, a flexible insert displays nonlinear oscillations which are demonstrated and analysed fully in Section 5.3. Knight et al. (2010) derived an equation for a tensioned membrane to predict the peak amplitude of the maximum deflection caused by nonlinear oscillations which is,

$$\eta_{\max} \approx \left(\frac{2\rho_{\mathrm{f}} L^3}{EhI\left(\eta''\right)} \right)^{1/2} U, \tag{5.12}$$

where U, is the dimensional flow speed and $I\left(\eta''\right)$ is an integral which is defined below. This equation was developed theoretically, however it does not take into account flexural rigidity or divergence-onset speed (i.e pre-divergence flow speeds).

Lucey et al. (1997) also give an equation to predict the peak amplitude of the maximum deflection from nonlinear oscillations in an open flow which is,

$$\frac{\eta_{\max}}{h} = 0.128 \left(\Lambda^{\mathrm{F}} - \Lambda^{\mathrm{F}}_{\mathrm{DO}} \right)^{0.503}, \tag{5.13}$$

where $\Lambda^{\mathrm{F}}_{\mathrm{DO}}$ is the well known divergence-onset flow speed for the open flow, $\Lambda^{\mathrm{F}}_{\mathrm{DO}} = 40$. This was developed by finding an equation to fit the curve of discrete data found from their numerical simulations.

The aim here is to theoretically develop an equation to predict the maximum amplitude of oscillations, using a similar method to Knight et al. (2010), but which includes the effect of flexural rigidity and takes into account the onset of divergence.

Starting with the nonlinear beam equation given by Equation (5.1), neglecting damping and spring-backing so that a simple elastic plate is being considered and

removing any time dependence gives,

$$B\frac{\partial^4\eta}{\partial x^4} - T_{\mathrm{I}}\frac{\partial^2\eta}{\partial x^2} = -\Delta p. \tag{5.14}$$

This equation can be non-dimensionalised using $x' = x/L$, $\eta' = \eta/L$ and $\Delta p' = \Delta p/\left(\rho_{\mathrm{f}}U^2\right)$ to give,

$$\frac{B}{\rho_{\mathrm{f}}U^2L^3}\frac{\partial^4\eta'}{\partial x'^4} - \frac{Eh}{\rho_{\mathrm{f}}U^2L(1-\nu^2)}\left(\int_0^1\left[\left(1+\left(\frac{\partial\eta'}{\partial x'}\right)^2\right)^{\frac{1}{2}}-1\right]dx'\right)\frac{\partial^2\eta'}{\partial x'^2} = -\Delta p'. \tag{5.15}$$

Due to the removal of any time dependence, Equations (5.14) and (5.15) are static equations valid for the mean state of the plate oscillations. The deflection, η', can be re-normalised using $\eta'' = \eta'(L/\eta_{\mathrm{mean}})$, where η_{mean} is the peak amplitude of the plate deflection in its mean state. Assuming η_{mean}/L is small, the integral can be simplified by binomial expansion giving,

$$\frac{B}{\rho_{\mathrm{f}}U^2L^3}\frac{\partial^4\eta'}{\partial x'^4} - \frac{Eh}{2\rho_{\mathrm{f}}U^2L(1-\nu^2)}\left(\frac{\eta_{\mathrm{mean}}}{h}\right)^2\left[\int_0^1\left(\frac{\partial\eta''}{\partial x'}\right)^2dx'\right]\frac{\partial^2\eta'}{\partial x'^2} = -\Delta p'. \tag{5.16}$$

Assuming that the plate has a single mode deflection (which was shown to be true for plates with no spring backing at divergence onset in Section 3.3, although at higher flow speeds there is a second mode influence, as discussed in Pitman and Lucey (2010)), the integral inside the brackets (which will now be denoted $I\left(\eta''\right)$) is a constant; $I\left(\eta''\right) = 4.925$. Rewriting Equation (5.16) in terms of the non-dimensional flow velocity $\Lambda^{\mathrm{F}} = \rho_{\mathrm{f}}U^2L^3/B$ (given by Equation (3.52)a) gives,

$$\frac{1}{\Lambda^{\mathrm{F}}}\frac{\partial^4\eta'}{\partial x'^4} - \frac{6I\left(\eta''\right)\eta_{\mathrm{mean}}^2}{h^2\Lambda^{\mathrm{F}}}\frac{\partial^2\eta'}{\partial x'^2} = -\Delta p'. \tag{5.17}$$

For this time independent system, only the curvature-dependent hydrodynamic stiffness term in the pressure evaluation needs to be considered, and so it is possible to write $\Delta p' \approx A\frac{\partial^2\eta'}{\partial x'^2}$, where A is a constant of proportionality. Using the assumption of a single mode deflection gives,

$$\eta' \approx \eta_{\mathrm{c}}\left(t\right)\sin\left(\pi x'\right), \tag{5.18}$$

$$\frac{\partial^2\eta'}{\partial x'^2} \approx -\eta_{\mathrm{c}}\left(t\right)\pi^2\sin\left(\pi x'\right) \tag{5.19}$$

and

$$\frac{\partial^4\eta'}{\partial x'^4} \approx \eta_{\mathrm{c}}\left(t\right)\pi^4\sin\left(\pi x'\right), \tag{5.20}$$

where $\eta_c(t)$ is the deflection at the centre panel at any given time.

Divergence is a static instability and at divergence onset the forces on the plate are perfectly balanced. Below divergence onset the plate displays a neutrally stable oscillatory motion and it is only at flow speeds above this critical value that nonlinear oscillations will occur. Given that the plate deflections are still small (linear) when divergence occurs, the induced tension from the plate will be negligible and therefore,

$$\frac{1}{\Lambda_{\mathrm{DO}}}\frac{\partial^4\eta'}{\partial x'^4} = -\Delta p' = -A\frac{\partial^2\eta'}{\partial x'^2}. \tag{5.21}$$

Using Equations (5.18) and (5.19), it can be shown that $A = \pi^2/\Lambda^{\mathrm{F}}_{\mathrm{DO}}$. Equation (5.16) then becomes,

$$\frac{\pi^2}{\Lambda^{\mathrm{F}}} + \frac{6I(\eta'')\,\eta^2_{\mathrm{mean}}}{h^2\Lambda^{\mathrm{F}}} = \frac{\pi^2}{\Lambda^{\mathrm{F}}_{\mathrm{DO}}}, \tag{5.22}$$

which gives,

$$\frac{\eta_{\mathrm{mean}}}{h} = \left[\left(\frac{\pi^2}{6I(\eta'')}\right)\left(\frac{\Lambda^{\mathrm{F}}}{\Lambda_{\mathrm{DO}}} - 1\right)\right]^{\frac{1}{2}}. \tag{5.23}$$

This equation can be used to predict the the mean-state amplitude of nonlinear oscillations and will be compared with Equations (5.12) and (5.13) from Knight et al. (2010) and Lucey et al. (1997) respectively.

5.1.4 Steady-State Solver

An alternative method to finding the maximum amplitude of the mean state is to perform numerical simulations with dissipation by including high levels of structural damping which will be demonstrated in Section 5.3.1, Figures 5.3 (a) and (c). With the inclusion of damping the flexible insert will eventually settle into a buckled mean state (Lucey et al., 1997). The solution, as plotted on a phase portrait (Figure 5.3 (c)), will spiral towards the attractor that is the mean-state amplitude. However in order to save computation time, it is possible to solve the time-independent system given by Equation (5.14), taking only the hydrodynamic stiffness part of the fluid pressure as the only pressure term which is not dependent on time. Using Equation (5.5) this gives the steady-state problem,

$$B\frac{\partial^4\eta}{\partial x^4} - T_{\mathrm{I}}\frac{\partial^2\eta}{\partial x^2} = -\frac{1}{2}\rho_{\mathrm{f}}\left(U^2 - (U\cos(\alpha) + u_{\mathrm{T}})^2\right). \tag{5.24}$$

Instead of performing a full time stepping simulation, Equation (5.24) can be solved iteratively to find the mean-state deflection shape. The basis equation for this is,

$$\eta_{n+1} = \left[B\left[D_4\right] - T_{\mathrm{I}}\left[D_2\right]\right]^{-1}\left\{\Delta p\left(\eta_n\right)\right\} \tag{5.25}$$

for some initial displacement, $\eta_0 \sin\left(\pi x\right)$. Equation (5.25) is repeated until η_n and η_{n+1} converge.

5.2 Validation

Presented here is validation of the numerical simulations. Validation of the theoretical investigation and steady-state solver will be demonstrated throughout the results by means of comparison with the numerical simulations and other investigations.

5.2.1 Structural Mechanics

To validate the structural mechanics of the finite-difference method as applied by numerical simulations, simulations are run with the fluid density set to zero, thereby neglecting the fluid mechanics of the system so that it behaves as a plate in vacuo. The same system parameters as in Section 3.2.1 are used in order to provide a convenient comparison

Figure 5.1 (a) shows the amplitude of the plate midpoint after being given an initial displacement with an amplitude of $\eta_0 = 0.0002$ m. A discretistion of $N_\mathrm{f} = 10$ panels is used with a time step size $\delta t = 1 \times 10^{-4}$ s. At this discretisation and time step, two iterations are required for convergence at each time. The plate displays the same neutrally stable oscillatory motion that is observed at pre-divergence flow speeds (when a fluid is present). It can be seen that the time period of the oscillations is $T = 0.067$ s, giving an angular frequency of $S_\mathrm{I} = 93.78$ rad/s. This value has a percentage error of 0.37% when compared with the fundamental frequency of $S_0 = 94.13$ rad/s calculated in Section 3.2.1 by Equation (3.50). To improve accuracy, the discretisation level can be increased, but in doing so the time step must reduced to ensure numerical convergence. For a plate in vacuo however, $N_\mathrm{f} = 10$ is sufficient.

It is remarked here that the inclusion of the nonlinear structural term T_I in the plate mechanics has no effect on these results, as the insert deflections are small enough for T_I to be negligible. Similarly, the numerical simulations for small disturbances with a fluid present are the same when comparing the linearised and nonlinear fluid mechanics and differences between the linear and nonlinear numerical simulations only occur at sufficiently large insert deflections.

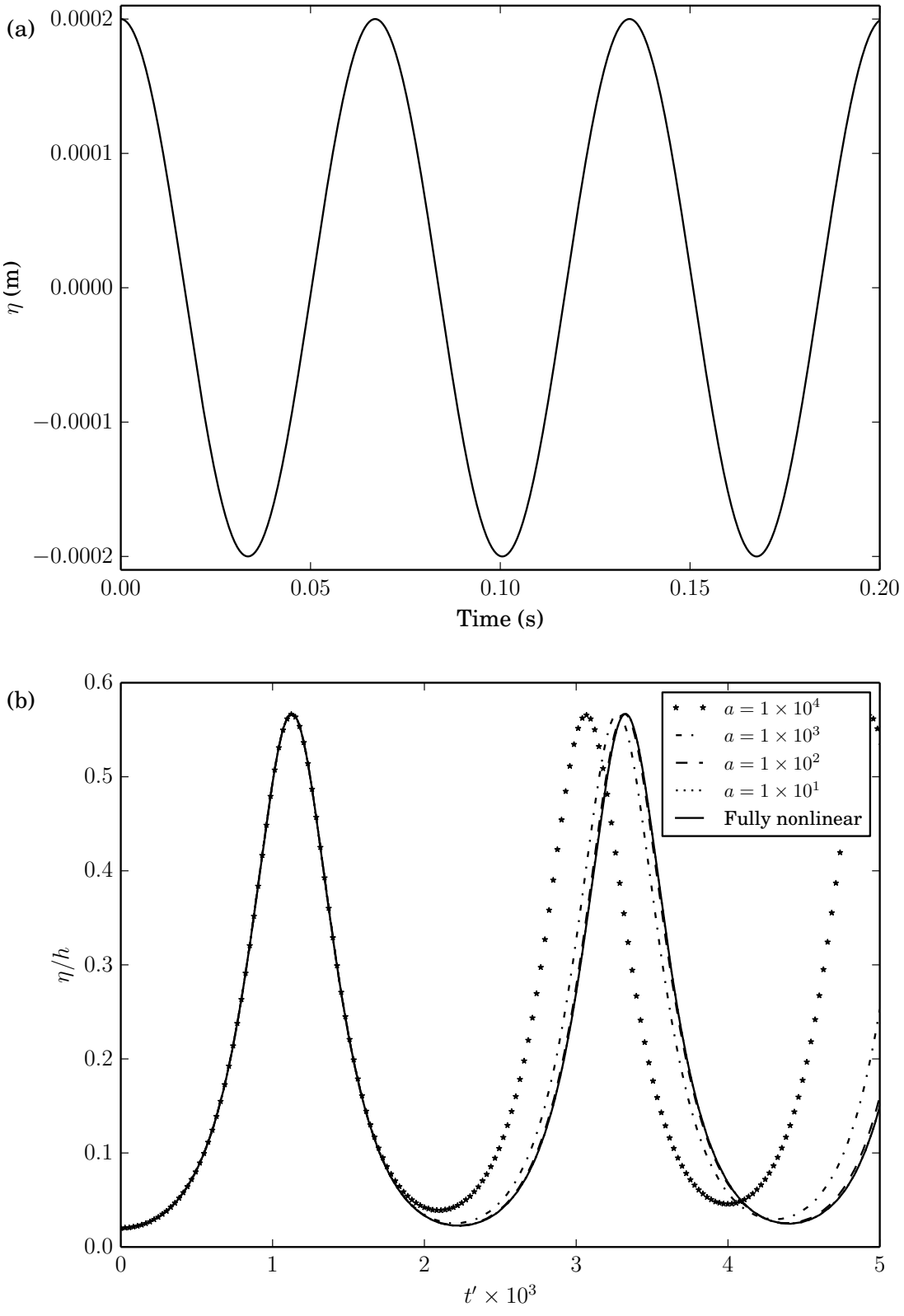

Figure 5.1: Amplitude of the midpoint of an oscillating plate: (a) In vacuo (pre-divergence linear oscillations) with $N_{\mathrm{f}} = 10$. (b) In a fluid (divergence induced nonlinear oscillations) with $\Lambda^{\mathrm{F}} = 61$, $N_{\mathrm{f}} = 30$, using different nonlinear approximations.

5.2.2 Fluid Mechanics

In order to validate this nonlinear numerical simulation model, the deflection history of a simple elastic plate within the divergence range of flows speeds is plotted in Figure 5.1 (b). The plate is given a small initial fundamental mode disturbance with amplitude $\eta_0/h = 0.02$ and as the plate diverges, the amplitude grows, causing the induced-tension restoring force of the plate mechanics to increase. The plate reaches the peak of its velocity when the forces acting upon it are matched, at which point the plate deflection slows, being zero at its maximum deflection, and the plate deflections start to reduce. This behaviour is known as nonlinear oscillations and without the induced tension term, T_{I}, included in the beam equation (5.1), this theoretical model would allow the plate growth caused by divergence to continue indefinitely.

Following Lucey et al. (1997) the same non-dimensional flow speed (given by Equation (3.52) (a)) is used here as in Section 3.3.1. For linear disturbances, the structural forces are dominated by the plate flexure, whereas for large deflections this is not the case. However, Λ^{F} can be rewritten,

$$\Lambda^{\mathrm{F}} = \frac{\rho_{\mathrm{f}} U^2}{E^*} \left(\frac{L}{h}\right)^3, \tag{5.26}$$

where E^* is the effective elastic modulus of the plate material,

$$E^* = \frac{E}{12\,(1-\nu^2)}. \tag{5.27}$$

In this form the non-dimensional flow speed is seen to comprise the product of a Cauchy number and a non-dimensional parameter for the plate dimensions.

The non-dimensional time used is,

$$t' = \sqrt{\frac{B}{\rho_{\mathrm{m}} h^3}} \left(\frac{t}{L}\right) = \sqrt{\frac{E^*}{\rho_{\mathrm{m}}}} \left(\frac{t}{L}\right). \tag{5.28}$$

The second form of Equation (5.28) shows that the non-dimensionalisation is related to the free shear-wave speed of the plate material and plate length, which is,

$$c_{\mathrm{s}} = \sqrt{\frac{B\alpha^2}{\rho_{\mathrm{m}} h}} = \frac{\pi h}{L} \sqrt{\frac{E^*}{\rho_{\mathrm{m}}}}, \tag{5.29}$$

for a plate with a fundamental mode deflection.

The illustrative parameters used for these simulations are the same as in Lucey et al. (1997), that is: $\rho_{\mathrm{f}} = 1000$ kg/m^3, $L_{\mathrm{f}} = 1.0$ m, $h = 0.01$ m, $B = 6500$ Nm, $K = 0$ N/m^3, $\rho_{\mathrm{m}} = 2600$ kg/m^3 and $d = 0$ Ns/m^3 with an applied non-dimensional flow velocity of $\Lambda^{\mathrm{F}} = 61$. This applied flow velocity corresponds to 20 m/s where the critical flow velocity of Λ^{F}=40 corresponds to 16 m/s. The results were found to converge with a discretisation of $N_{\mathrm{f}} = 30$ and time step size $\delta t = 1 \times 10^{-5}$ s ($\delta t' = 0.0158$). Fully nonlinear numerical simulations have been run and the amplitude of the plate midpoint with non-dimensional time is shown in Figure 5.1 (b). These results agree well with those of Kapor (2012), Lucey et al. (1997) and Pitman (2007).

Figure 5.1 (b) also shows the effect of using a nonlinear approximation whereby the influence coefficients are calculated every a time steps rather than with every time step. This approximation is valid because for the very small time steps used here, the plate displacement and velocity only varies slightly with each time step. The reason for using a nonlinear approximation is to significantly cut down on computation time by reducing the total number of calculations required. It can be seen that for this discretisation ($N = 30$) and time step ($\delta t = 1 \times 10^{-5}$ s), a nonlinear approximation of $a = 1 \times 10^2$ or smaller is sufficient to give accurate results.

5.2.3 Numerical Simulations within a Channel

In Section 3.3.1 the divergence-onset flow speed as it varies with non-dimensional channel height H/L is characterised and can be seen in Figure 3.5 (a). A line of best fit of this data is found and given by,

$$\Lambda_{\mathrm{D}} = \Lambda^{\mathrm{F}}_{\mathrm{DO}}(1 - \exp(-3.3H/L)). \tag{5.30}$$

By running numerical simulations and observing the plate behaviour at a given flow speed, it is possible to establish the speed at which divergence occurs at any given channel height. This data, along with Equation (5.30), is shown in Figure 5.2. The illustrative properties used to generate these results are the same as those used in Section 3.3.1 with a mass ratio $\mu = 92.3$. A discretisation of $N_{\mathrm{f}} = 50$, $L_{\mathrm{r}} = 2L$ is used so that $N = 500$ with $\delta t = 1 \times 10^{-5}$ s ($\delta t' = 0.023$). The plate is

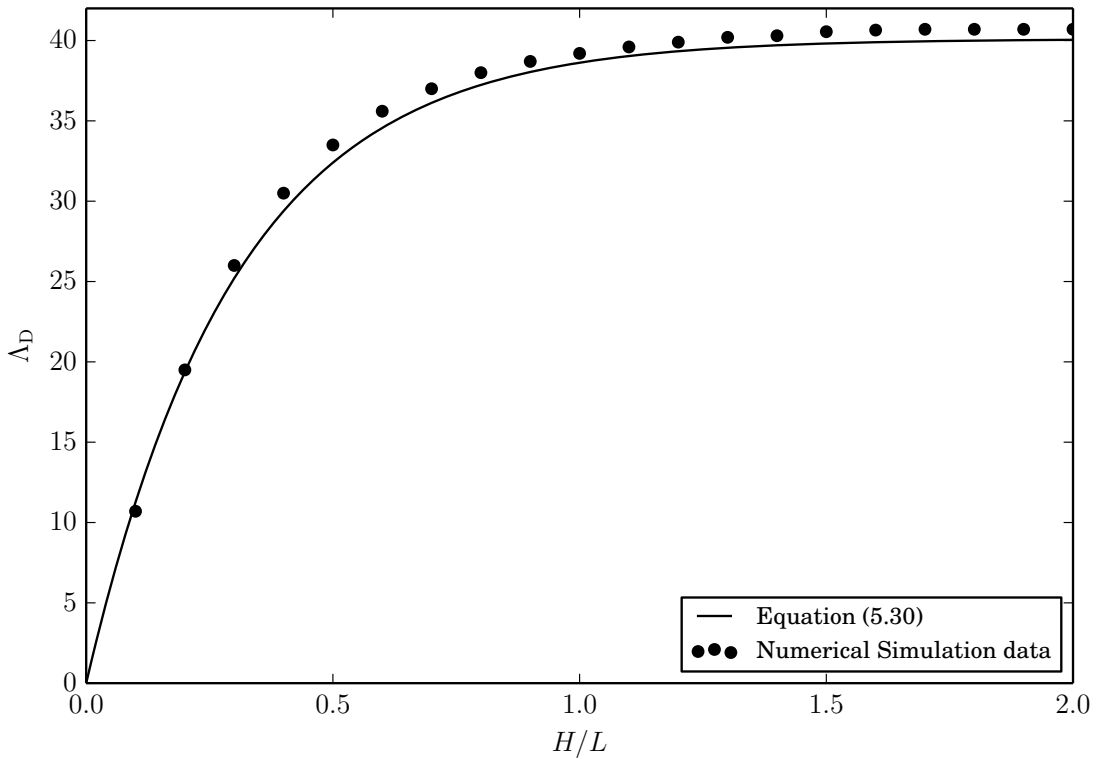

Figure 5.2: Divergence-onset flow speed as given by numerical simulations and as predicted by Equation (5.30).

given an initial fundamental mode disturbance with amplitude $\eta_0/h = 0.08$.

The data from numerical simulations agrees closely with Equation (5.30) thereby validating the implementation of the rigid upper surface, along with the rigid surfaces up- and downstream of the flexible plate by agreement with the results of the state-space solution of Section 3.3.1. It is noted here that this provides validation that the channel geometry is accurately modelled by numerical simulations at small deflections, as divergence occurs when the plate disturbances are still within the linear range of amplitudes. Thus, the results of Figure 5.2 are the same when full nonlinear numerical simulations are performed and when linear numerical simulations are performed. This does not provide validation of the full range of nonlinear effects within a channel. Other nonlinear effects such as flow separation and boundary layer effects will be discussed with the results of Section 5.3.

5.3 Results

5.3.1 Open Flow

Simple Elastic Plate

Nonlinear oscillations in an open flow ($H = \infty$) using the same illustrative system parameters as in Section 5.2.2 are shown in Figure 5.3, where the mass ratio is $\mu = 38.5$ and a non-dimensional flow velocity of $\Lambda^{\mathrm{F}} = 61$ is used. The displacement of the plate midpoint as it varies with non-dimensional time (as in Figure 5.1 (b)) is shown in Figure 5.3 (a) for a plate without structural damping as the dotted line, and for a plate with a high level of structural damping ($d = 10000$ Ns/m^3) shown by the solid line. The inclusion of damping causes the amplitude and time period of each oscillation to decrease until the plate settles in its mean state. In this case, the non-dimensional maximum amplitude of the mean state of the plate is $\eta_{\mathrm{mean}}/h = 0.401$. This compares well with the value of $\eta_{\mathrm{mean}}/h = 0.417$ calculated from Equation (5.23), giving a percentage error of 3.8%.

The mechanics of the nonlinear oscillations are described in Section 5.2.2, where it is remarked that the induced tension term acts as a restoring force for the nonlinear instability. In fact, all nonlinear structural terms are stabilising. It is not as simple, however, to characterise the nonlinear fluid mechanics. Figure 5.1 (b), and Figure 2 from Lucey et al. (1997) both show that with nonlinear structural mechanics, the amplitude of nonlinear oscillations is the same with linear fluid mechanics and nonlinear fluid mechanics, but that the oscillation period is greater when nonlinear fluid mechanics are included. This suggests that the nonlinear fluid mechanics are more destabilising than linear fluid mechanics as it takes longer for the restoring forces to reduce the amplitude of the oscillation.

The plate deformations for a succession of time steps covering the first half of the nonlinear oscillation cycle shown in Figure 5.3 (a) for a plate without structural damping is shown in Figure 5.3 (b) where the bold line represents the plate when it has the amplitude of the mean state. The plate deformations are not symmetrical about $x/L = 0.5$ as the applied flow velocity causes the plate to be skewed in the direction of flow. This figure can be compared with Figure 3 (a) from Lucey et al. (1997). The plate deformations of a structurally damped plate

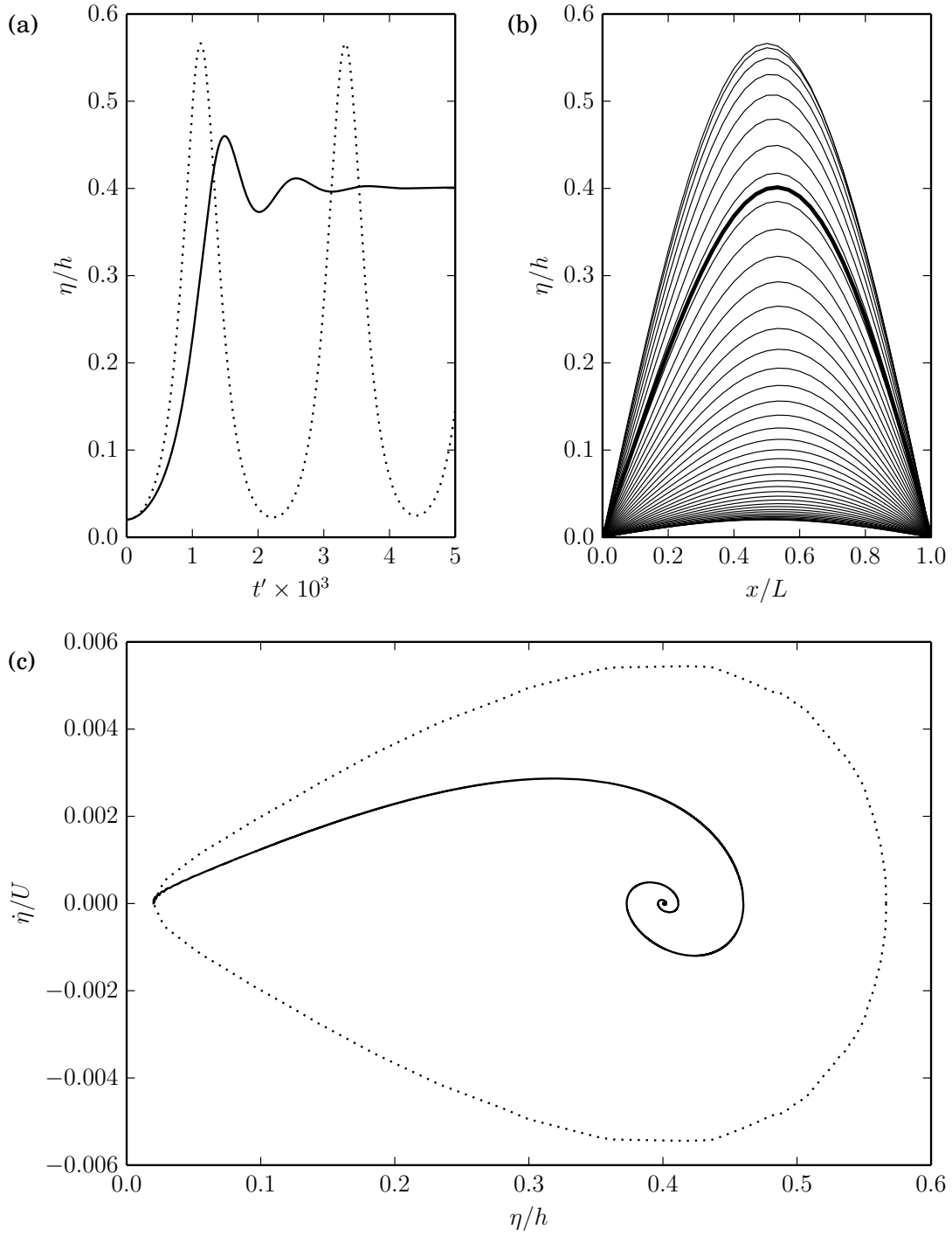

Figure 5.3: Results from numerical simulations of the open-flow ($H = \infty$) when $\Lambda^{\mathrm{F}} = 61$: (a) Displacement of the plate midpoint with non-dimensional time for a plate with ($d = 10000$ Ns/m^3, solid line) and without (dotted line) structural damping, (b) Plate deformations for a succession of time steps covering the first half of a nonlinear oscillation without structural damping; the bold line represents the plate when it has the amplitude of the mean state and (c) Phase portrait for a damped (solid line) and undamped (dotted line) plate.

eventually come to rest on the bold line (mean state) shown.

The phase portrait of the midpoint of both a damped (solid line) and undamped (dotted line) plate are shown in Figure 5.3 (c) and can be compared to Figure 4 of Lucey et al. (1997). For a plate without structural damping the plate motion will continue on the orbit shown, whereas the damped plate can be seen to spiral towards the attractor that is $\eta_{\text{mean}}/h = 0.401$. The plate has been given an initial positive amplitude, however when the plate is given a negative initial amplitude, the results are the reflection of those shown about $\eta/h = 0$, as demonstrated in Lucey et al. (1997). For a full investigation when the plate is given larger initial amplitudes, see Lucey et al. (1997).

By performing numerical simulations without damping, the amplitude of the plate at its greatest deflection, η_{max}, of a nonlinear oscillation for any given flow speed can be found, and similarly the mean-state amplitude, η_{mean}, can be found by including structural damping. A more efficient means to finding η_{mean} is by the

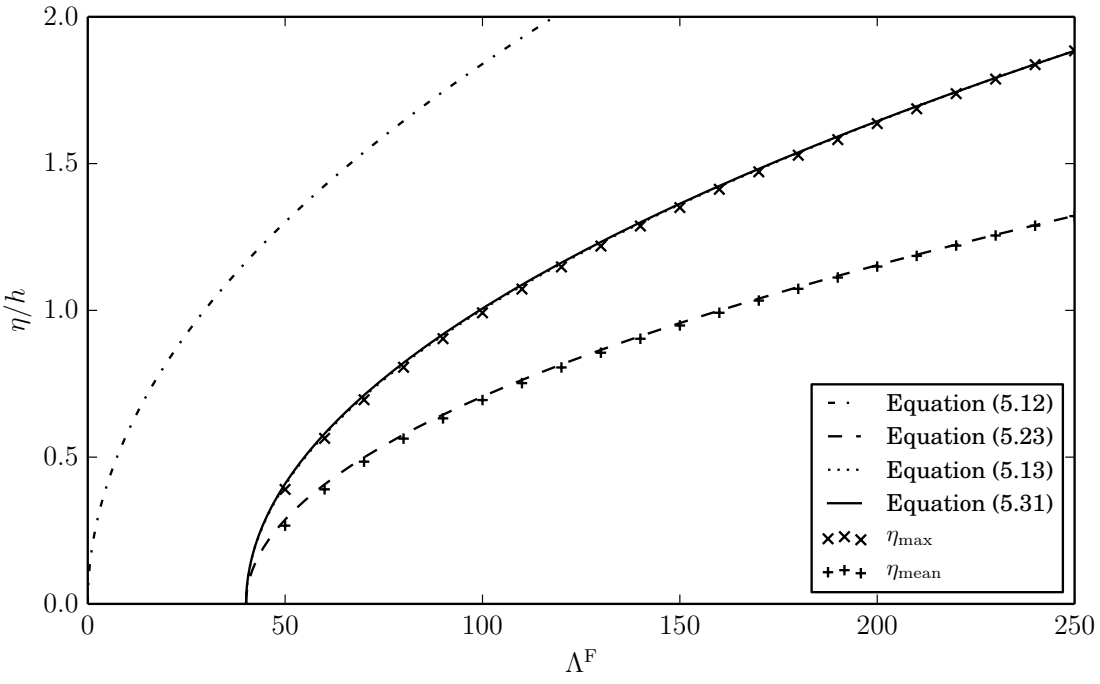

Figure 5.4: Equations (5.12) and (5.23) to predict η_{mean} (continuous data), compared with data from the steady-state solver (discrete data) and Equations (5.13) and (5.31) (continuous data) to predict η_{max}, compared with data from numerical simulations (discrete data). Note: Equations (5.13) and (5.31) are difficult to distinguish as they are almost exact.

use of the steady-state solver outlined in Section 5.1.4. At $\Lambda^{\mathrm{F}} = 61$ with $P_{\mathrm{f}} = 30$, the steady-state solver yields a value of $\eta_{\mathrm{mean}}/h = 0.401$ which agrees with the value shown in Figure 5.3. This value tends towards the theoretical result as the discretisation is increased.

Figure 5.4 shows Equations (5.12) and (5.13) from Knight et al. (2010) and Lucey et al. (1997) respectively, which predict the maximum amplitude of nonlinear oscillations, η_{max}. It can be seen that Equation (5.12) is notably different from Equation (5.13) in that the maximum deflection tends to zero as their aim was to show that the maximum amplitude is proportional to the flow velocity and so the flow speed at which divergence onset occurs is not considered. In contrast Equation (5.13) clearly shows that nonlinear oscillations only start to occur at a flow speed greater than that of divergence onset, $\Lambda^{\mathrm{F}}_{\mathrm{DO}} = 40$. Also plotted on Figure 5.4 is Equation (5.23) which predicts the mean-state amplitude of nonlinear oscillations.

Equation (5.13) can be compared with the discrete data found from numerical simulations and Equation (5.23) can be compared to the discrete data for η_{mean} found using the steady-state solver. Clearly the numerical simulations and steady-state solver agree well.

From Figure 5.4 it can be seen that $\eta_{\mathrm{max}} = C\eta_{\mathrm{mean}}$ for some C, and by comparing the discrete data for η_{mean} and η_{max} it is established that $C = 1.425$. Although this does vary slightly with flow velocity; for all Λ^{F} in the divergence range of flow speeds ($40 \leq \Lambda^{\mathrm{F}} \leq 270$) that are demonstrated in Figure 3.3, C is within less than 1% of 1.425.

An equation for η_{max}, based on Equation (5.23), can now be given as,

$$\frac{\eta_{\mathrm{max}}}{h} = C\left[\left(\frac{\pi^2}{6I\left(\eta''\right)}\right)\left(\frac{\Lambda^{\mathrm{F}}}{\Lambda_{\mathrm{DO}}} - 1\right)\right]^{\frac{1}{2}}. \tag{5.31}$$

Equation (5.31) has also been plotted on Figure 5.4 and it can be seen that this gives an excellent approximation to predicting η_{max} when compared with the Lucey et al. (1997) result of Equation (5.13).

By considering Equation (5.24), it is apparent that η_{mean} is not dependent on the mass ratio, $\mu = \rho_{\mathrm{f}}L/\rho_{\mathrm{m}}h = (\rho_{\mathrm{f}}/\rho_{\mathrm{m}})\,/\,(h/L)$. However when considering η_{max}, the first term of Equation (5.1) must be included, and therefore η_{max} could have a dependence on the mass ratio, in which case C would be a function of μ. By

using the steady-state solver to find η_{mean} and running numerical simulations to determine η_{max} at a range of different mass ratios, achieved by changing the fluid density, it is possible to show that neither result changes at any non-dimensional flow speed and hence C is a constant which is independent of mass ratio. This agrees with Lucey et al. (1997) who found that their η_{max} predictions did not vary with h/L. Equations (5.23) and (5.31) are therefore valid for any given mass ratio.

Tensioned Membrane

For completeness it is now demonstrated that a pre-tensioned membrane shows the same trend as Figure 5.4. The motion of the membrane is described by the nonlinear membrane equation,

$$\rho_{\text{m}} h \frac{\partial^2 \eta}{\partial t^2} - T_{\text{P}} \frac{\partial^2 \eta}{\partial x^2} - T_{\text{I}} \frac{\partial^2 \eta}{\partial x^2} = -\Delta p, \tag{5.32}$$

where T_{P} is a uniform pretension given by,

$$T_{\text{P}} = \sigma A = Eh\epsilon, \tag{5.33}$$

where σ is the tensile stress of the membrane, A is the cross sectional area ($A = 1 \times h$, i.e. per unit length), E is Young's modulus and ϵ is the extensional strain of the membrane; $\epsilon = e/L$ where e is the extension of the membrane. The strain, ϵ, may be considered to be the 'stretch parameter' that determines the pretension, T_{P}, for a given initial extension, e.

By following the same method as in Section 5.1.3, but this time re-normalising the insert deflection with $\eta'' = \eta' \left(L/\eta_{\text{mean}}\right)$ as a more appropriate scaling, the tensioned membrane equivalent of Equation (5.16) is,

$$\frac{T_{\text{P}}}{\rho_{\text{f}} U^2 L} \frac{\partial^2 \eta'}{\partial x'^2} + \frac{Eh}{2\rho_{\text{f}} U^2 L \left(1-\nu^2\right)} \left(\frac{\eta_{\text{mean}}}{L}\right)^2 \left[\int_0^1 \left(\frac{\partial \eta''}{\partial x'}\right)^2 dx'\right] \frac{\partial^2 \eta'}{\partial x'^2} = \Delta p'. \tag{5.34}$$

Assuming a single mode deflection (applying Equations (5.18), (5.19) and (5.20)) and writing in terms of the non-dimensional flow velocity for a membrane ($\Lambda^{\text{M}} = \rho_{\text{f}} U^2 L / T_{\text{P}}$ given by Equation (3.52) (b)) gives,

$$\frac{1}{\Lambda^{\text{M}}} + \frac{I\left(\eta''\right)}{2\epsilon\Lambda^{\text{M}}\left(1-\nu^2\right)} \left(\frac{\eta_{\text{mean}}}{L}\right)^2 = \frac{1}{\Lambda^{\text{M}}_{\text{DO}}}, \tag{5.35}$$

where $\Lambda^{\mathrm{M}}_{\mathrm{DO}}$ is the non-dimensional divergence-onset speed for a tensioned membrane in an open flow, $\Lambda^{\mathrm{M}}_{\mathrm{DO}} = 4.03$, as demonstrated in Figure 3.8. Rearranging Equation (5.35) gives,

$$\frac{\eta_{\mathrm{mean}}}{L} = \left[\left(\frac{2\epsilon\left(1-\nu^2\right)}{I\left(\eta''\right)}\right)\left(\frac{\Lambda^{\mathrm{M}}}{\Lambda^{\mathrm{M}}_{\mathrm{DO}}} - 1\right)\right]^{\frac{1}{2}}. \tag{5.36}$$

Although both sides of this equation are non-dimensional, ϵ is the stretch parameter that determines T_{P}, so the mean-state amplitude is dependent on initial strain as well as flow velocity.

Equation (5.36) is plotted in Figure 5.5 (a) and when compared with the open flow results for a simple elastic plate shown in Figure 5.4 the two clearly show the same trend. However, the tensioned membrane has the added strain parameter. This has been demonstrated by showing the results for three different levels of strain and it can be seen that increasing the pretension in the plate affects an increase in the mean, and therefore maximum deflections of the nonlinear oscillations. Also shown on Figure 5.5 are the discrete data from the iterative steady-state solver using the same illustrative parameters as developed for the simple elastic plate in Section 5.3.1.

Although the results show that an increase in pretension affects an increase in the magnitude of the nonlinear oscillations, the non-dimensional flow velocity is given in terms of the pretension, and so the dimensional divergence-onset speed is dependent on the pretension. If Figure 5.5 (a) was replotted in terms of the dimensional flow velocity, U, the magnitude of the oscillations for a fixed value of U would in fact decrease as the pretension is increased which is to be expected from a physical aspect.

To provide a result which is valid for all strain values; Equation (5.36) can be rewritten as,

$$\frac{\eta_{\mathrm{mean}}}{L\epsilon^{\frac{1}{2}}} = \left[\left(\frac{2\left(1-\nu^2\right)}{I\left(\eta''\right)}\right)\left(\frac{\Lambda^{\mathrm{M}}}{\Lambda^{\mathrm{F}}_{\mathrm{DO}}} - 1\right)\right]^{\frac{1}{2}}, \tag{5.37}$$

which is plotted in Figure 5.5 (b) alongside the discrete data from the steady-state solver. The results from Figure 5.5 (a) are shown here as having collapsed into a single result.

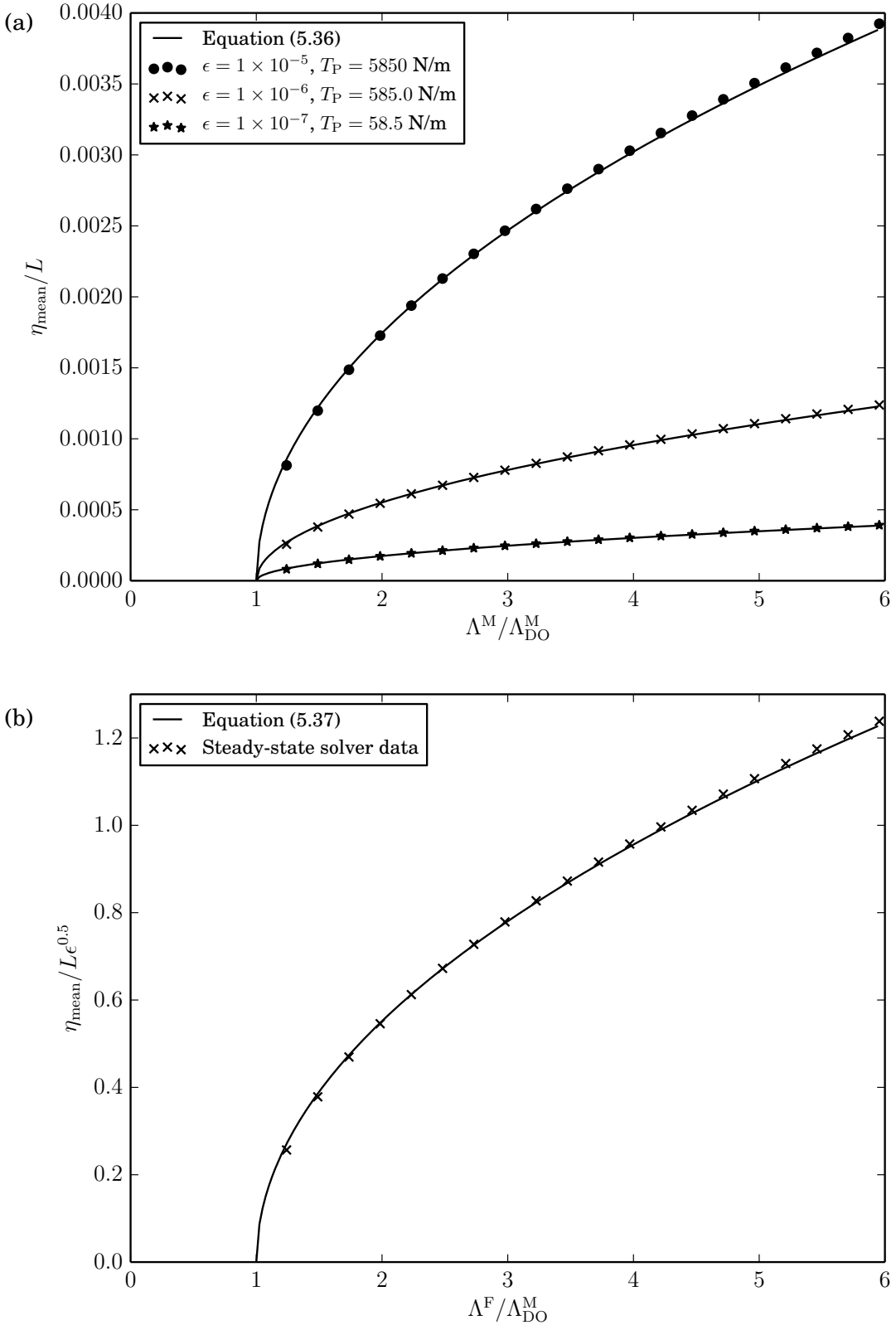

Figure 5.5: (a) Equation (5.36) with data from steady-state solver at three different strains and (b) Equation (5.37) with data from the steady-state solver.

External Pressure

The effect of an external pressure applied to the flexible surface is now considered. The beam equation is altered so that it reads,

$$\rho_{\mathrm{m}} h \frac{\partial^2 \eta}{\partial t^2} + d\frac{\partial \eta}{\partial t} + B\frac{\partial^4 \eta}{\partial x^4} + K\eta - T_{\mathrm{I}}\frac{\partial^2 \eta}{\partial x^2} = -\Delta p + p_{\mathrm{X}}, \tag{5.38}$$

where p_{X} is a constant external pressure applied at the underside of each of the mass points of the discretised plate. By removing the time dependence, the steady-state solver can be used to find the mean state of this modified system for different external pressures.

Applying an external pressure to a collapsible channel was studied by Pihler-Puzović and Pedley (2013). They used an inviscid-core boundary layer model to consider the steady state and found that self-excited oscillations do not occur.

Figure 5.38 (a) shows the mean-state amplitudes as they vary with Λ^{F} for a range of different external pressures. It can be seen that when an external pressure is present, the mean state of the system is increased. In addition, rather than a distinct point at which divergence occurs, there is now a gradual transition from a neutrally stable oscillatory motion to nonlinear oscillations. This transition is more gradual as p_{X} is increased. At zero flow speed, p_{X} is the only effect, which causes the η_{mean} amplitude to be displaced from $y = 0$. As the flow velocity increases, the pressure perturbation increases, creating a gradual increase in η_{mean} but with p_{X} still causing the dominant effect. Further increases to flow speed cause the pressure perturbation to become more significant than the constant external pressure, which results in the mean-state amplitude increasing at a faster rate. This in turn causes the induced tension term to take over as the dominant effect which is why at very high flow speeds, the results for all external pressures are seen to converge to the $p_{\mathrm{X}} = 0$ case.

The effect that external pressure has on the η_{mean} and η_{max} values is further demonstrated in Figure 5.6 (b) which shows the phase portrait of nonlinear oscillations for four different external pressures when $\Lambda^{\mathrm{F}} = 61$. When $p_{\mathrm{X}} = 0$, the phase portrait can be compared to Figure 5.3 (c). The value of the attractor of the oscillations at the mean amplitude for each pressure is shown in the figure by a larger marker and increases with p_{X}. A similar increase is seen for the η_{max}

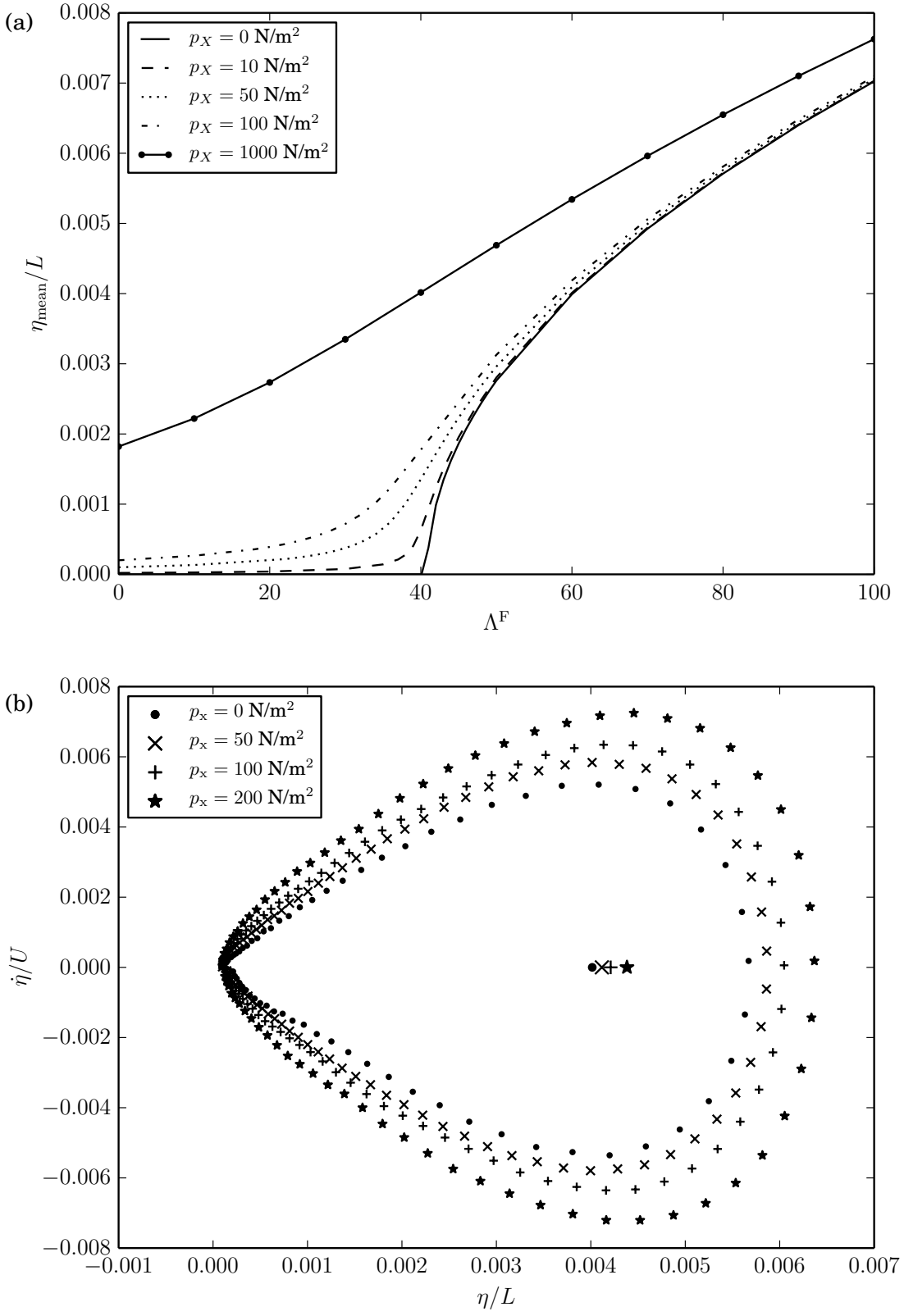

Figure 5.6: (a) The amplitude of the mean state with non-dimensional speed for different applied external pressures. (b) Phase portrait of the plate midpoint for different applied external pressures when $\Lambda^{\text{F}} = 61$. The larger data points denote the η_{mean} value for each external pressure value.

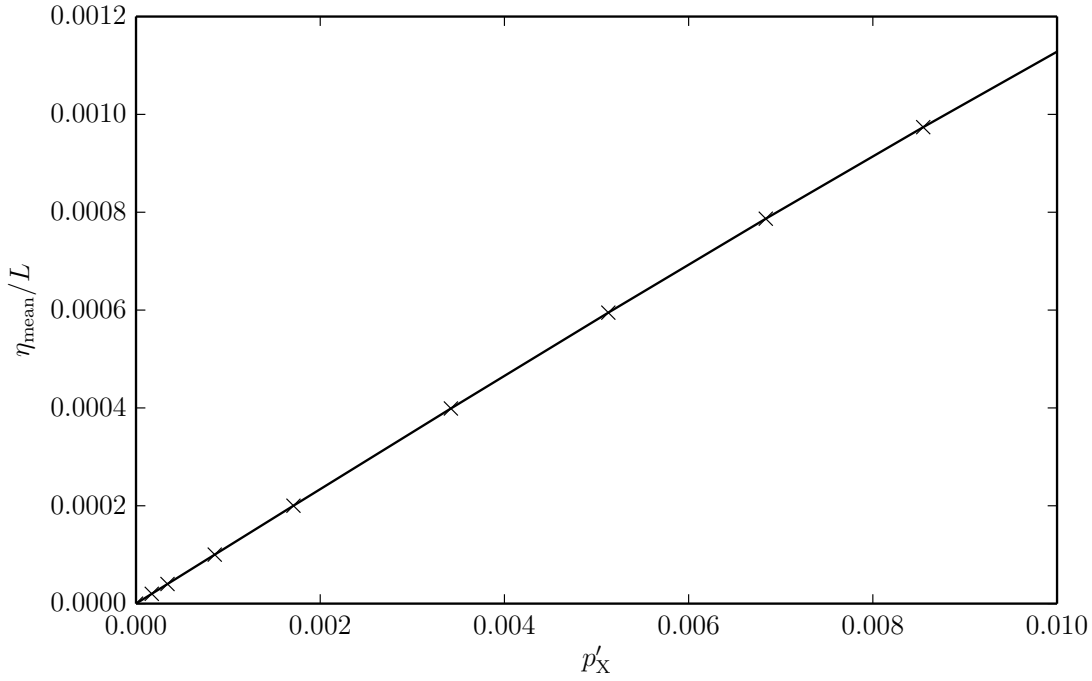

Figure 5.7: The amplitude of the mean state for insert oscillations with applied external pressure p'_{X} when $\Lambda^{\text{F}} = 0$.

values.

Non-dimensionalising pressure with $\Delta p' = \Delta p/(\rho_{\text{f}} U^2)$ is not appropriate at zero flow speeds so an alternative non-dimensional pressure is given as,

$$p'_{\text{X}} = \frac{p_{\text{X}} L^3}{E h^3}. \tag{5.39}$$

Figure 5.7 shows the amplitude of the mean state as it varies with external pressure for a flow velocity $\Lambda^{\text{F}} = 0$. It can be seen that there is a linear relationship between the two found to be,

$$\frac{\eta_{\text{mean}}}{L} = 0.117 p'_{\text{X}}. \tag{5.40}$$

Displaced double mode initial disturbances

Thus far, the results have all been generated by giving the plate an initial single mode disturbance of the form,

$$\frac{\eta}{L} = \frac{\eta_0}{L} \sin(\pi x), \tag{5.41}$$

where $\eta_0/L = 1 \times 10^{-4}$. These are now compared to a plate given an initial mode two disturbance that is displaced from $y = 0$. This disturbance takes the form,

$$\frac{\eta}{L} = \frac{\eta_1}{L} \sin(\pi x) + \frac{\eta_2}{L} \sin(2\pi). \tag{5.42}$$

Numerical simulations are run for initial disturbances given by both Equation (5.41) and Equation (5.42) when $p'_{\mathrm{X}} = 0.00171$ ($p_{\mathrm{X}} = 100\ \mathrm{N/m^2}$) at three different flow speeds.

Figure 5.8 (a) shows the displacement of the plate centre when the plate is given an initial single mode displacement (Equation (5.41)) with $\eta_0/L = 1 \times 10^{-4}$ and the non-dimensional flow velocity is $\Lambda^{\mathrm{F}} = 0$. The plate displays stable oscillations as in the case when there is no external pressure but where the mean position has been displaced to $\eta/L = 2 \times 10^4$ as predicted by Equation (5.40). The mean position of $\eta/L = 2 \times 10^4$ is shown in Figure 5.8 (a) as the dotted line. The corresponding insert deflections for the initial amplifying phase is shown in Figure 5.8 (b).

In Figures 5.8 (c) and (d) the plate has a displaced second mode initial deflection given by Equation (5.42) with η_1/L the same as in Figures 5.8 (a) and (b) at 1×10^{-4} and with $\eta_2/L = 5 \times 10^{-5}$. The displacement of the plate midpoint (centre panel) with time is plotted in Figure 5.8 (c) as the solid line and the plate deflections for the first growing phase is shown in Figure 5.8 (d). The deflections of the plate midpoint closely resemble that of the single mode deflection shown in Figure 5.8 (a) with a peak to peak amplitude of $A_1/L = 2 \times 10^{-4}$. Also plotted on Figure 5.8 (c) is the displacement of the panel such that $x/L = 0.25$ (given by the dashed line) and $x/L = 0.75$ (given by the dotted line). This demonstrates that the plate has the same large amplitude, single mode oscillations as for the case shown in Figure 5.8 (a) and (b), but that there is also a second mode flutter occurring simultaneously. This second mode vibration oscillation has a peak to peak amplitude of $A_2/L = 0.0001$ and this does not appear to vary with increasing time. The fraction of the double and single mode amplitudes is $A_2/A_1 = 0.5$.

Figure 5.9 shows the same initial single and double displacement results as in Figure 5.8 but for the case when $\Lambda^{\mathrm{F}} = 30$. The amplitude of the single mode oscillation has increased (to $A_1/L = 1.17 \times 10^{-3}$) and the frequency of the oscillations has decreased which is also found for the case without any external pressure as shown in Section 3.3.1. Comparing Figure 5.8 (c) with Figure 5.9 (c); the plate still displays the simultaneous single and double mode oscillations with

$A_2/L = 1 \times 10^4$ being the same as when $\Lambda^F = 0$. The fraction A_2/A_1 has now decreased to 8.58×10^{-2}.

In Figure 5.10 the same results as in Figures 5.8 and 5.9 are shown but where the flow speed has been increased to $\Lambda^F = 70$. The plate is now no longer stable but displaying full nonlinear oscillations where $A_1/L = 7.03 \times 10^{-3}$. Figure 5.10 (c) shows that for the second mode initial displacement the second mode flutter appears to have disappeared completely, however on close inspection a slight second mode flutter can still be seen when η/L is at its lowest point with the same peak to peak amplitude of $A_2/L = 1 \times 10^{-4}$. The fraction of first and second mode amplitudes is now $A_2/A_1 = 1.42 \times 10^{-2}$ which is why the second mode flutter is less noticeable as the plate behaviour is now dominated by the fundamental mode.

In Figures 5.8, 5.9, 5.10 (c) and (d) the second mode flutter amplitude has been constant at $A_2/L = 0.05$ regardless of the flow velocity. An investigation into varying η_2/L reveals that the second mode amplitude stays fixed at the initial amplitude given ($A_2/L = \eta_2/L$), for all Λ^F. In contrast, the amplitude of the single mode oscillations is only dependent on the applied flow speed and varying η_2/L does not change A_1.

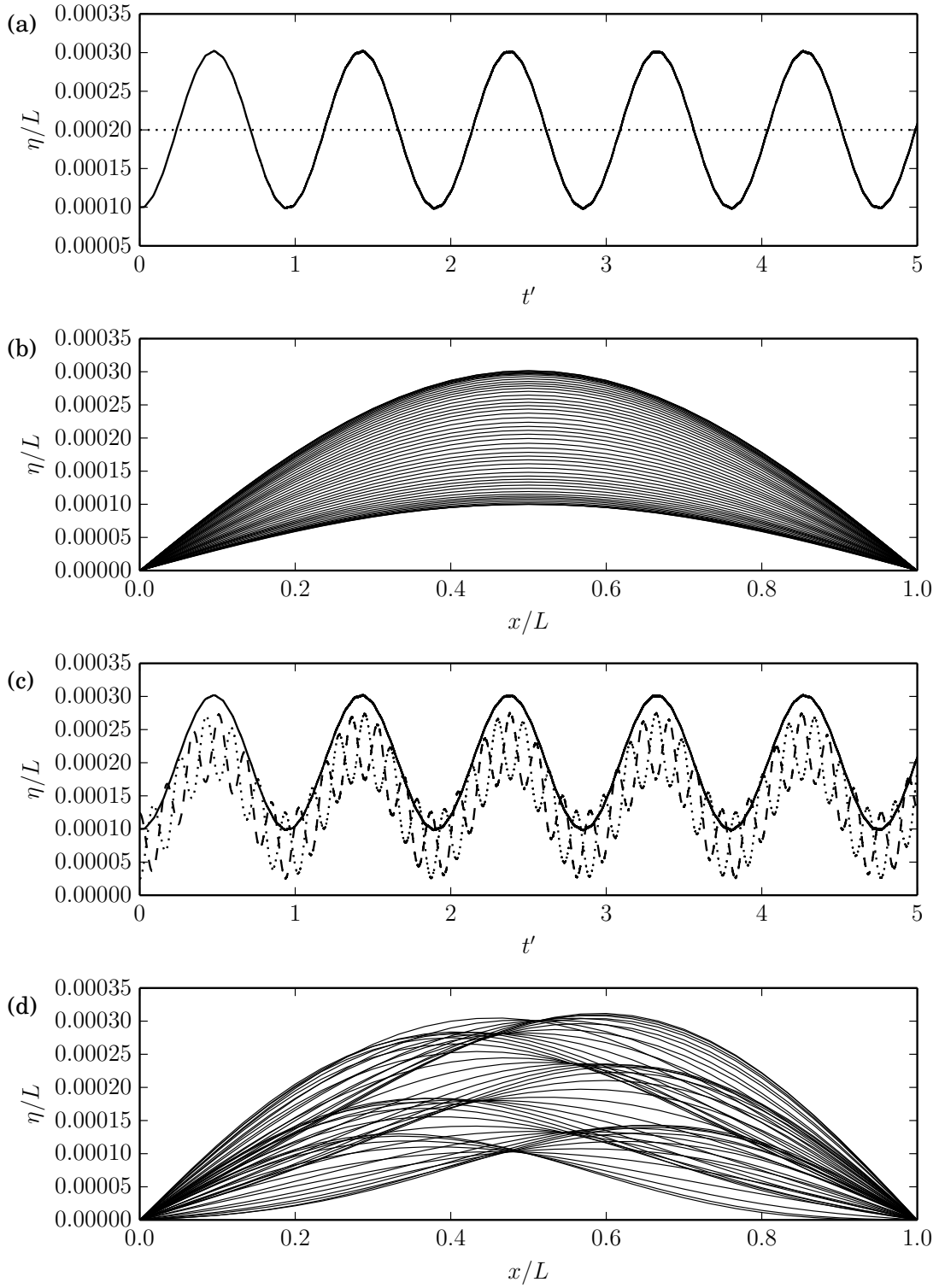

Figure 5.8: Plate deflections with an applied external pressure $p_{\mathrm{X}} = 100$ N/m^2 when $\Lambda^{\mathrm{F}} = 0$ for an initial single mode ((a) and (b)) and displaced double mode ((c) and (d)) disturbance. (a) and (c) Displacement of the plate at $x/L = 0.25$ (dashed line), 0.5 (solid line) and 0.75 (dotted line) with time, (b) and (d) Plate deflections for the first growing phase.

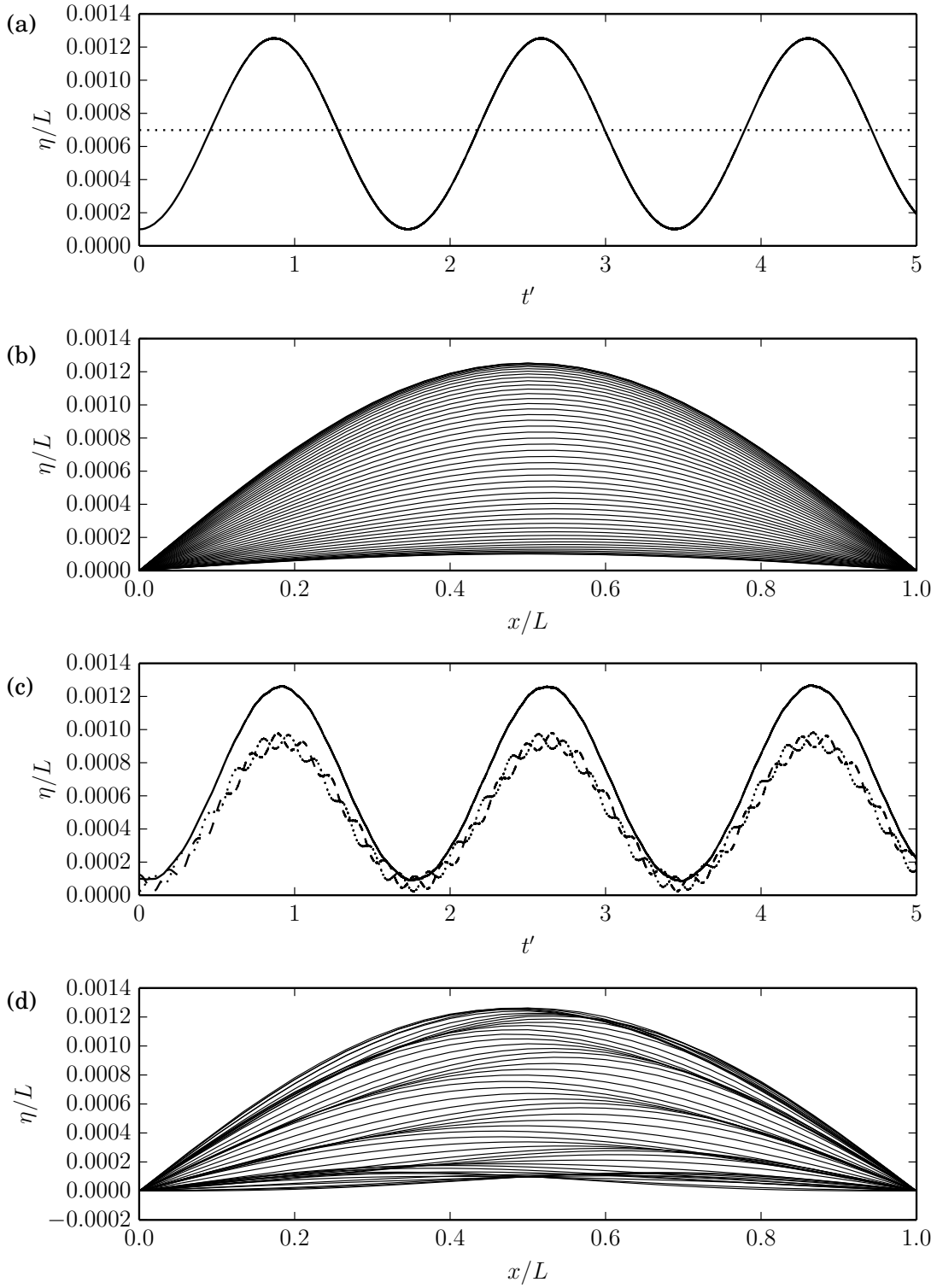

Figure 5.9: Plate deflections with an applied external pressure $p_{\mathrm{X}} = 100$ N/m^2 when $\Lambda^{\mathrm{F}} = 30$ for an initial single mode ((a) and (b)) and displaced double mode ((c) and (d)) disturbance. (a) and (c) Displacement of the plate at $x/L = 0.25$ (dashed line), 0.5 (solid line) and 0.75 (dotted line) with time, (b) and (d) Plate deflections for the first growing phase.

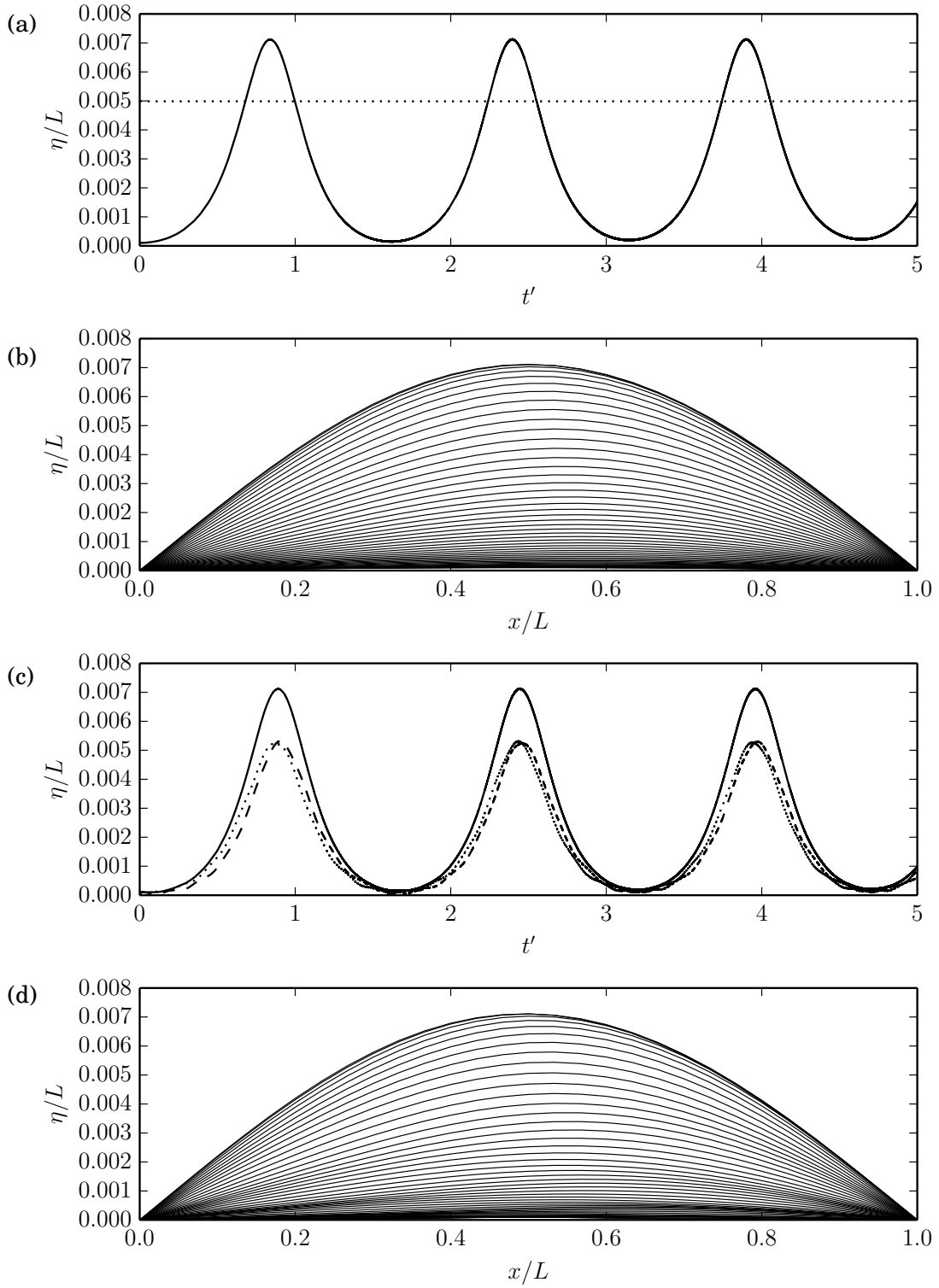

Figure 5.10: Plate deflections with an applied external pressure $p_{\mathrm{X}} = 100$ N/m^2 when $\Lambda^{\mathrm{F}} = 70$ for an initial single mode ((a) and (b)) and displaced double mode ((c) and (d)) disturbance. (a) and (c) Displacement of the plate at $x/L = 0.25$ (dashed line), 0.5 (solid line) and 0.75 (dotted line) with time, (b) and (d) Plate deflections for the first growing phase.

5.3.2 Channel Flow

This section considers the large plate deflections where the flexible surface now comprises part of an otherwise rigid channel. From Section 3.3.1 it is known that the plate undergoes the same stability transitions with increasing flow velocity as for the open flow but with reduced stability bounds dependent on the channel height, H/L. Numerical simulations reveal that the nonlinear oscillations demonstrated in the open flow are still present in the channel flow within the divergence range of flow speeds but that the channel height affects the amplitude and frequency of the nonlinear oscillations.

Given that nonlinear oscillations only occur at flow speeds higher than the critical flow speed for divergence, when considering a channel the non-dimensional flow speed is normalised by the onset flow speed of divergence for any given channel height, Λ_{D}, from Equation (5.30). Figure 5.11 shows the mean state and

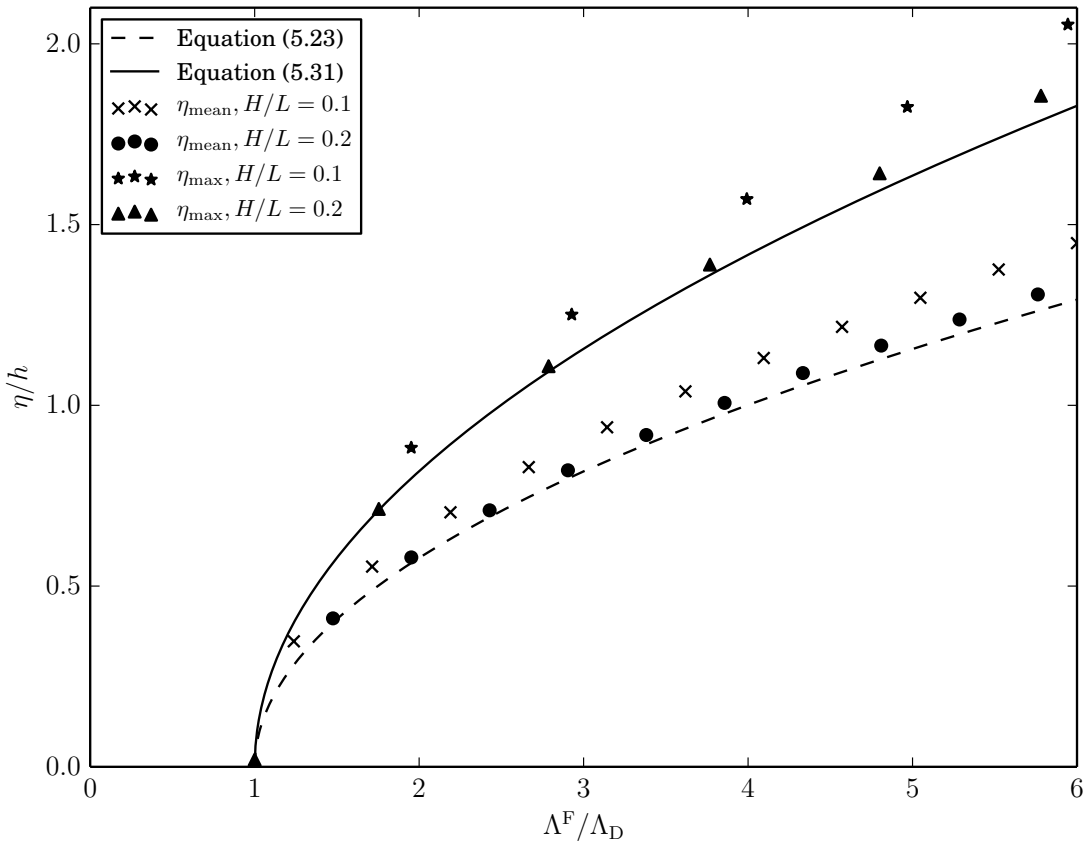

Figure 5.11: Mean state and maximum amplitudes for an open flow given by Equations (5.23) and (5.31) compared with values for two different channel heights generated respectively by the iterative solver and numerical simulations.

maximum amplitudes found from the steady-state solver and numerical simulations respectively for two different non-dimensional channel heights, $H/L = 0.1$ and $H/L = 0.2$, along with the open flow results of Equations (5.23) and (5.31).

These results, along with other simulations, reveal that the ratio, C, of maximum to mean-state amplitudes of the oscillatory motion is not dependent on channel height but is in fact the same as for the open flow for all values of H/L. However, Figure 5.11 shows that the values of η_{mean} and η_{max} are dependent upon channel height and that as the channel height is decreased the maximum and mean-state amplitudes increase for a given normalised non-dimensional flow velocity. This could be expected on physical grounds because mass conservation creates higher flow speeds, hence higher flow stiffness ($\rho_{\text{f}}U^2$) in the region where the deformed plate effectively causes a narrowing of the channel.

To develop a formula for plate-deformations in a channel flow, Equations

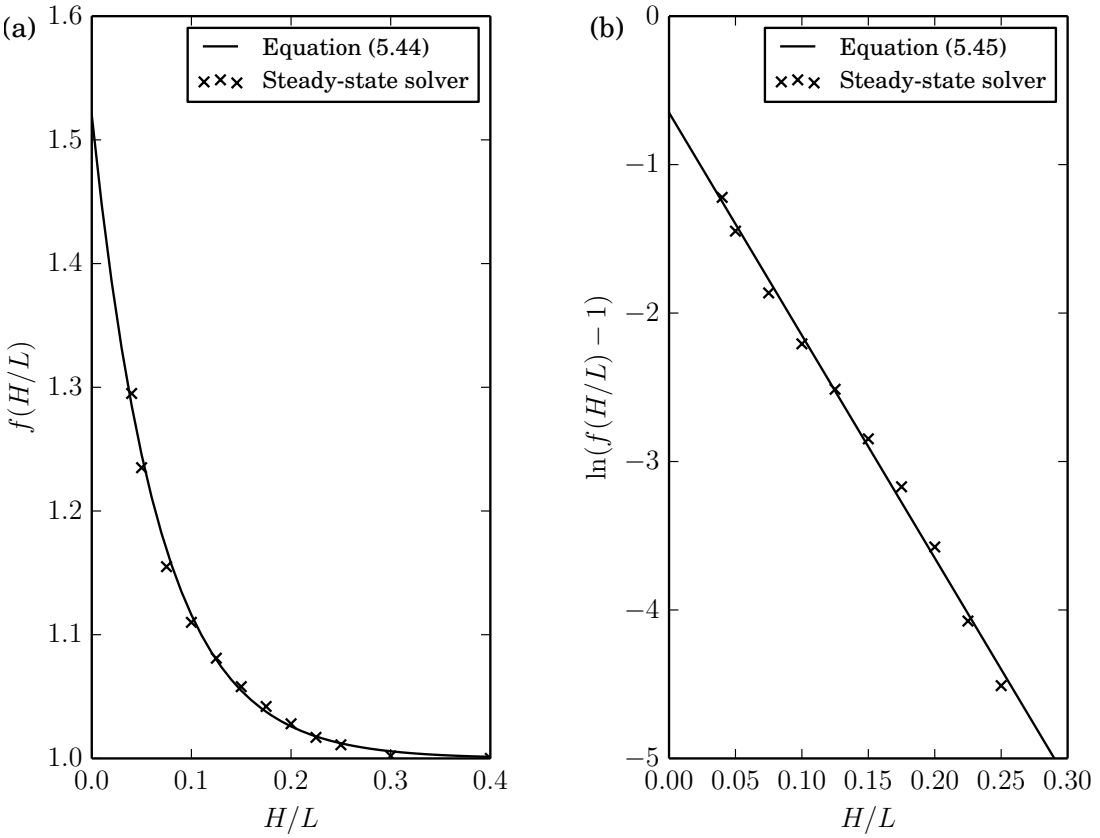

Figure 5.12: (a) Values of $f(H/L)$ found at different channel heights using the steady-state solver and (b) The natural logarithm of data shown in (a).

(5.23) and (5.31) are rewritten,

$$\frac{\eta_{\text{mean}}}{h} = f\left(H/L\right)\left[\left(\frac{\pi^2}{6I\left(\eta''\right)}\right)\left(\frac{\Lambda^{\text{F}}}{\Lambda_{\text{D}}}-1\right)\right]^{\frac{1}{2}}, \tag{5.43a}$$

$$\frac{\eta_{\text{max}}}{h} = Cf\left(H/L\right)\left[\left(\frac{\pi^2}{6I\left(\eta''\right)}\right)\left(\frac{\Lambda^{\text{F}}}{\Lambda_{\text{D}}}-1\right)\right]^{\frac{1}{2}}, \tag{5.43b}$$

where Λ_{D} is given by Equation (5.30) and $f\left(H/L\right)$ is a function such that $f\left(H/L\right) \to 1$ as $H \to \infty$. It is noted that for a nonlinear system, f is more likely to be a function of $\left(H-\eta_{\text{max}}\right)/L$ rather than H/L, as $\left(H-\eta_{\text{max}}\right)$ is a more accurate representation of the constriction in the channel, however for all the simulations considered here this effect is negligible and it is sufficient to assume f is a function of H/L; this gives an accurate approximation.

A value of f is found for a range of different channel heights by using the η_{mean} values found from the steady-state solver and this has been plotted in Figure 5.12 (a). In order to find an expression for f, Figure 5.12 (b) shows that by taking the natural logarithm of f, a linear relationship is found so that,

$$\ln(f(H/L)-1) = -15H/L - 0.65, \tag{5.44}$$

giving,

$$f(H/L) = 1 + 0.52\exp\left(-15H/L\right). \tag{5.45}$$

Equations (5.44) and (5.45) are also plotted in Figure 5.12 (a) and (b) respectively and can be shown to give a good approximation.

Equations (5.43) (a) and (b) can now be used to predict the maximum and mean-state amplitude for all channel heights within the range of nonlinear divergence flow speeds and for $H/L \geq 0.05$. The first constraint arises from the fact that at higher flow speeds significant levels of Mode-2 content appears in the deformation (Lucey et al., 1997) while the second approximately demarcates the threshold at which viscous effects in the flow can no longer be neglected.

Oscillation Frequency

The frequency of nonlinear oscillations and how they are affected by the proximity of an upper channel wall are considered here. Lucey et al. (1997) give an equation to predict this frequency for the open flow (Equation (21) of their paper) which

is,

$$\omega' = 0.93\,(h/L)^{1.5}\left(\Lambda^{\mathrm{F}} - \Lambda_{\mathrm{DO}}\right)^{0.380}. \tag{5.46}$$

This equation was found by curve fitting data found from numerical simulations. In Figure 5.3 (a) the non-dimensional time period of a flexible plate in an open flow is shown to be $T' = 2.2 \times 10^3$ at $\Lambda^{\mathrm{F}} = 61$, $(\Lambda^{\mathrm{F}}/\Lambda_{\mathrm{DO}} = 1.52)$, which gives a corresponding frequency of $\omega' = 2\pi/T' = 2.86 \times 10^{-}3$. This value agrees with the findings of Lucey et al. (1997) and can be compared with the value of $\omega' = 2.95 \times 10^{-}3$ which is found from Equation (5.46).

Figure 5.13 shows the frequency data from the numerical simulations performed at four different channel heights (including the open flow, $H/L = \infty$) as it varies with normalised non-dimensional flow speed. Also plotted (as the top dashed line) is Equation (5.46) and a line of best fit for each channel height (as

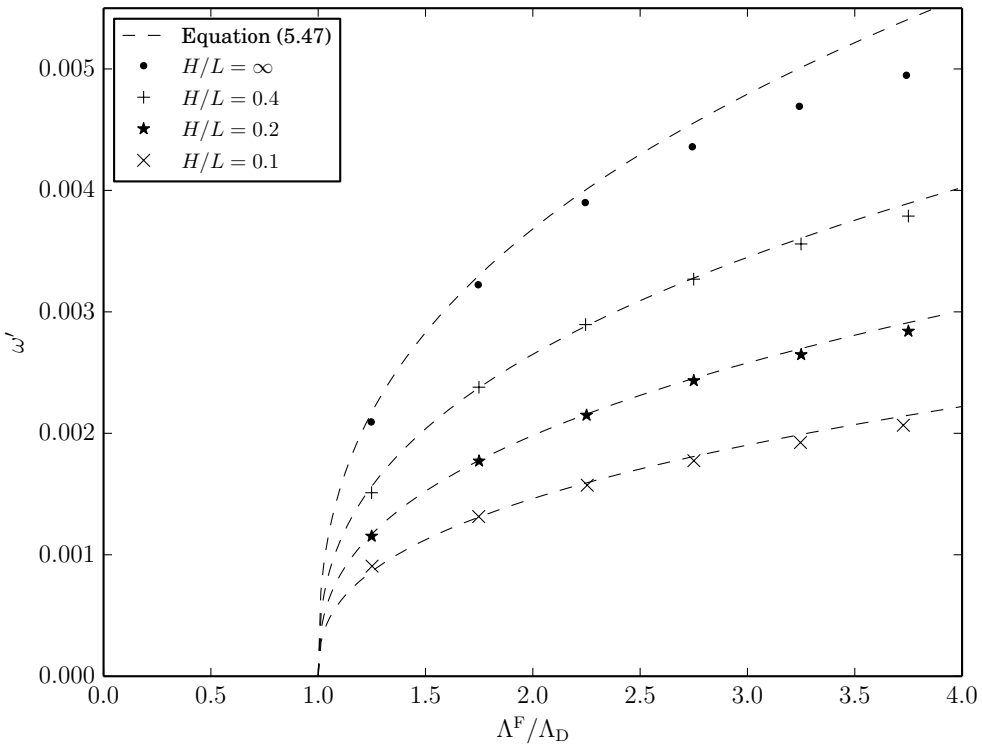

Figure 5.13: Variation of the nonlinear oscillation frequency with normalised non-dimensional flow speed for the open flow and three different channel heights. The dashed line respresents the line of best fit for each channel height in the form given by Equation (5.47).

the remaining dashed lines) given in the form,

$$\omega'\left(H/L\right) = A\left(H/L\right)\left(h/L\right)^{1.5}\left(\Lambda^{\mathrm{F}} - \Lambda_{\mathrm{D}}\right)^{B}, \tag{5.47}$$

where A is a function of non-dimensional channel height and $B = 0.380$ as in Equation (5.46).

The function A is found to be approximately,

$$A\left(H/L\right) = -0.42\exp\left(-1.9H/L\right) + 0.93. \tag{5.48}$$

For low flow velocities the results from numerical simulations agree closely with Equation (5.47), however at higher applied flow speeds the numerical simulation data starts to vary, which agrees with the findings of Lucey et al. (1997). This is caused by a greater influence from the higher order modes which are found only at higher applied flow velocities. These results were all presented using a fixed mass ratio, $h/L = 0.01$, $\mu = 38.46$. For a comprehensive investigation into the effect of changing mass ratio for the open flow see Lucey et al. (1997).

5.4 Summary

Using a finite-difference method to model the plate mechanics coupled with a boundary-element method to model the fluid mechanics, time stepping numerical simulations are performed to establish the behaviour of a finite flexible plate comprising an open flow and one wall of a channel flow. A potential flow model is used. This method is based on that of Lucey et al. (1997). The divergence-onset flow speeds, as they vary with non-dimensional channel height, were found and agree with the results from the linear methods used in Chapter 3.

The nonlinear oscillations of Lucey et al. (1997) for the open flow were also found here in both the open and channel flows within the divergence range of flows speeds. Particular attention is paid to the mean state and maximum amplitudes of these oscillations and how they vary with onset flow speed as this gives an indication of channel blockage. By removing the time-dependence from the system equations, the mean-state amplitude is found from an efficient iterative steady-state solver and this is compared with a theoretically developed equation to predict the mean-state amplitudes. The maximum amplitudes are then found by performing full numerical simulations and it is found that the ratio between the amplitudes does not vary with flow speed or with mass ratio. From this an equation is given to predict the maximum amplitudes for a given flow speed using the theoretical equation derived for the mean-state amplitudes.

The nonlinear oscillations of a tensioned membrane are then considered and it is shown that the mean state and maximum amplitudes depend upon the initial strain which determines the pretension. Some results are demonstrated and a non-dimensional equation is given to predict the amplitudes in terms of the initial strain.

The effect of a uniform external pressure applied to the flexible insert is considered. It is shown that an external pressure increases the mean-state amplitude and that when an external pressure is present there is no longer a distinct flow velocity at which divergence occurs but that the plate undergoes a gradual (more gradual for increasing external pressure) transition from neutrally stable oscillations to unstable divergence-induced oscillations. The plate is then given a displaced mode two initial disturbance and it is demonstrated that the amplitude

of the second mode flutter does not vary with flow speed as with the single mode oscillation amplitude but stays constant at the initial amplitude given. This results in the plate behaviour becoming more dominated by the fundamental mode with increasing flow velocity.

Finally, the case of a finite flexible insert comprising one wall of a channel is considered with attention paid to the proximity of the upper channel wall. Flow velocity is normalised with the divergence-onset speed (given by the linear predictions in Chapter 3) for a given channel height and it is found that the higher flow stiffness caused by channel constriction, increases the amplitude of the oscillations for a given normalised non-dimensional flow speed, but that the ratio between the mean state and maximum amplitudes does not vary with channel height and is the same as for the open flow. An equation for the amplitudes is given which is valid for all channel heights (with the exception of very narrow channels where the potential flow assumption may no longer be valid). It is also shown that reducing the channel height not only increases the amplitudes of nonlinear oscillations for a given normalised non-dimensional flow velocity but also reduces the oscillation frequency.

In the methods presented, potential flow gives an approximate model for flows at very high Reynolds numbers noting that this approximation precludes the effect of boundary-layer separation for high levels of boundary curvature that might occur due to the deformation of the insert. In a potential flow, separation only occurs at a stagnation point. Flow separation has not been accounted for as all the insert deformations that have been considered have very low curvature, $1/R$, that scales with $2\eta_{\max}/L^2$ for the deformations herein; for example, when $\eta_{\max}/h = 2.0$, then $1/R \approx 0.04$. These methods and results serve as a basis for more complete models that would incorporate viscous effects and boundary-layer separation. To give an indication of when flow separation would occur, the experimental investigation of Sturm et al. (2012), where the flow separation point of an air-foil for various flow speeds and angle of attacks is given. They show that as flow speed increases, a greater angle of attack is required for flow separation to occur. They use flow speeds of 5, 10 and 20 m/s. In addition the direct numerical simulation investigation of Lamballais et al. (2010) for high

Reynolds numbers shows that decreasing the curvature causes flow separation to occur further downstream. The range of curvature levels they consider however, are all considerably higher then those considered here.

Chapter 6

Concluding Remarks

By using a finite-difference method to model the structural mechanics and a boundary-element method to model the fluid mechanics, an investigation into the fluid-structure interactions of a flexible insert in an ideal open and channel flow has been presented.

This chapter includes; a brief overview of the main contributions of this thesis to the field, a more in depth analysis of the methods and results of each of the key chapters, a description of the limitations of the research presented and a list of future research directions that would improve and build upon the method and results described in this thesis.

6.1 Main Contributions

The main contributions of this work are:

- A set of stability bounds for a finite flexible insert within a channel, dependent on the channel width for a variety of different insert types.
- An analytically derived equation to predict divergence onset in an infinity long flexible channel in terms of the channel width.
- Stability bounds for a finite flexible insert separating two channels dependant on channel width.
- Characterisation of transient growth for both open and channel flows including consideration of mass ratio and channel height.

- Theoretical equations to predict the mean-state amplitude, maximum amplitude and oscillation frequency of nonlinear oscillations in an open and channel flow.

- Characterisation of nonlinear oscillations in open and channel flows including the effect of an external pressure gradient and changing the initial conditions.

- A basis for which future experimental research can be compared. The choice of physical parameters chosen throughout the thesis should enable comparison with experimental results.

6.2 Linear Stability of a Fluid-Loaded Flexible Insert

Using a potential flow, the finite-difference and boundary-element methods were coupled using a state-space method, which allowed direct extraction of the eigenvalues and eigenvectors of the system. In this way the onset flow speeds for the divergence and modal-coalescence flutter instabilities for a finite flexible insert in an open flow were identified and compared with previous studies. The new aspect of this work was to then extend this method to account for rigid walls above and up- and down-stream of the flexible insert so that it then comprises one section of an otherwise rigid channel. It has been discovered that narrower channels will become unstable at lower flow speeds. A full set of stability bounds has been presented for a variety of different plate types. The effect of varying the mass ratio was investigated and found not to change the effect of the proximity of the upper channel wall on the stability bounds.

In parallel, an analytically derived equation for the onset of divergence of an infinitely long channel with one rigid and one flexible wall is presented. This is compared to the finite insert analysis of a plate with a high order mode shape (spring-backed flexible plate) and the two are found to be in good agreement. There is a small discrepancy between the two methods which increases as the non-dimensional channel height increases and an investigation reveals that this is

due to an amplitude modulation present for a finite flexible insert, which becomes less significant for narrow channels.

Eigen-analysis was then performed for a finite flexible plate separating two otherwise rigid channels. A set of stability bounds is presented considering the proximity of the channel walls, and the fluid density and flow speed in each channel. It is found that when the flows in each channel are travelling in opposing directions, the morphology of the eigen solution changes and a second mode divergence occurs before modal-coalescence onset.

This linear investigation has provided accurate predictions for the stability bounds of a variety of systems.

6.3 Non-Modal Analysis

Using the eigen-analysis developed in the linear work, an energy growth function is defined to assess the transient growth that is possible in the range of flow speeds before instability onset as predicted by linear theory. It is shown that for both the open and channel flows, significant growth is possible for the whole range of neutrally stable flow speeds, and that as the flow speed approaches instability onset, the energy growth becomes infinitely large.

The energy growth function is oscillatory. Its beating period is related to the lowest frequency eigenvalue and its complex conjugate in the pre-divergence range of flow speeds, and the difference between the frequency of the lowest two eigenvalues in the divergence-recovery range of flow speeds. Reducing the mass ratio reduces the energy growth function because as the system approaches the in vacuo case, the non-normality reduces as the eigenmodes of the in vacuo case are orthogonal.

As the non-dimensional channel height is reduced, the magnitude of the energy growth function increases for a given non-dimensional flow speed. It is shown that this, along with the decrease in stability bounds predicted by the linear theory, is due to the increase in the gradient of the curvature of the streamlines which must have zero curvature at the upper channel wall.

The non-modal analysis demonstrates that even at low flow velocities, tran-

sient growth might occur. As such, nonlinear modelling is necessary at flow speeds before that of instability onset in order to accurately model the complete flexible insert behaviour, however, linear theory is still sufficient to predict the onset of divergence and modal-coalescence flutter.

6.4 Nonlinear Fluid-Structure Interactions of a Fluid-Loaded Flexible Insert

The finite-difference and boundary-element methods have been coupled to perform fully nonlinear time-stepping numerical simulations. In the divergence range of flow speeds, a limit-cycle flutter type behaviours occurs. Both the open and channel flows are considered and from the numerical simulations, the maximum amplitude and time period of the nonlinear oscillations can be found for a given non-dimensional flow speed, channel height and mass ratio. By including structural damping, the flexible plate will settle in time at a mean-state position, and so the mean-state deformation can also be found from numerical simulations. A more efficient method to find the mean-state deformation is to use an iterative steady-state solver by removing the time-dependence from the system equations. It is found that the ratio between the mean and maximum amplitudes is constant and does not depend upon mass ratio, flow speed or channel height.

A theoretical equation is derived to predict the mean-state maximum amplitude for the open flow, and from this an equation for the maximum amplitude can also be given. These theoretical equations compare well with the numerical simulation and steady-state solver data. The effect of applying an external pressure and changing the initial conditions of the flexible insert is considered.

Finally, an equation for the mean-state amplitude, maximum amplitude and oscillation frequency is determined which is valid for all channel heights. This allows the nonlinear behaviour of a flexible insert in an open and channel flow to be characterised and gives a simple way to assess the channel blockage that would occur for a given set of system parameters.

6.5 Limitations

Although the results presented are valid for a wide range of applications, the following limitations on the methods used are recognised:

- Potential flow modelling yields results that are valid for flows which are in the limit of infinite Reynolds number.
- The linear approximations used in Chapters 3 and 4 give accurate results for small insert deflections.
- The potential-flow assumption is no longer valid for very narrow channels, so as channel height tends to zero, alternative modelling techniques should be considered.
- The two-dimensional models do not take into account any three dimensional effects. However, Lucey and Carpenter (1993a) have shown that the phenomenology is largely unchanged (from the two-dimensional system) after a full three-dimensional investigation is undertaken for the open-flow case.
- Viscous effects such as boundary layers and fluid instabilities are not considered.
- Flow separation that might occur for very large insert deflections is not accounted for so the results presented in Chapter 5 are valid for insert deformations of low curvature where flow separation would not occur.

Taking into account these limitations, this thesis provides a range of results that might find application in engineered systems such as hydro-power plants and nuclear engineering, hull-panels of high-speed ships, underwater drilling, fluid-conveying pipelines and biomechanical applications such as airways and large blood vessels.

6.6 Future Research Directions

As considered in Section 6.5, although the modelling techniques used here give results that are valid for a wide range of system parameters, there are several

limitations which could be addressed in future work to develop a more complete model of the fluid-structure interactions of a flexible plate comprising an open and channel flow:

- It would be possible to include a relatively simple approximation for flow separation by considering the pressure gradient following the method of Cyr and Newman (1996). This approximation would still enable the use of potential flow. Alternatively a shear layer could be added as demonstrated by Knight et al. (2010) which would also allow continued use of the potential flow modelling.

- Following the methods of Pihler-Puzović and Pedley (2013), a viscous boundary layer could be included close to the open or channel flow walls while maintaining an inviscid core. This would capture some of the non-linear effects and still allow an eigen-analysis to predict the onset of instabilities but would only be valid for small-amplitude deflections. Alternatively a velocity-vorticity disturbance formulation, as used by Tsigklifis and Lucey (2013, 2014) could be extended to the geometry of a channel flow, which would allow the eigenmodes of Tollmien-Schlichting waves and travelling-wave flutter to be identified.

- It is possible to solve the full Navier-Stokes equations as demonstrated in a channel flow by Pitman and Lucey (2010). They perform an eigen-analysis making the results relevant for small insert deflections to predict instability onset. However, nonlinear numerical simulations could be performed to consider large amplitude insert deflections.

- The global stability of a three-dimensional compliant panel in a Blasius boundary-flow has been considered by Tsigklifis and Lucey (2014). Similarly, the methods used here could be extended to three dimensions for the potential flow case, to consider the stability bounds, the transient growth and the nonlinear behaviour of diverging plates in both the open and channel flow.

- An experimental study to observe the phenomena of a finite flexible insert

would be greatly beneficial to allow comparison with some of the results and conclusions presented here.

Bibliography

V. V. Alekseyev. The form of the loss of stability of a boundary layer on a flexible surface at high Reynolds numbers. *Journal of Applied Mathematics and Mechanics*, 66(5):775–786, 2002.

V. V. Babanko. Experimental investigation of the hydrodynamic stability of simple flat membrane surfaces. *Gidromekhanika*, 24:3–11, 1973. [In Russian].

V. V. Babanko, N. A. Gnitetskii, and L. F. Kozlov. Preliminary outcomes of research on the elastic properties of the skin of live dolphins. *Bionika*, 3:12–19, 1969. [In Russian].

K. Bach, H. Hetzler, and W. Seemann. Stability of a steady flow guided by flexible walls. *Proceedings in Applied Mathematics and Mechanics*, 10:353–354, 2010.

K. Bach, H. Hetzler, and W. Seemann. Dynamic stability of a steady flow in a planar channel. *Proceedings of the 10th International Conference on Vibration Problems (ICOVP)*, 139, 2011a.

K. Bach, H. Hetzler, and W. Seemann. On stability and self-excited vibrations in fluid-structure-interaction. *Proceedings in Applied Mathematics and Mechanics*, 11:309–310, 2011b.

K. Bach, H. Hetzler, and W. Seemann. Oscillations of a channel with a flexible wall conveying viscous flow. *Proceedings in Applied Mathematics and Mechanics*, 12:245–246, 2012.

T. B. Benjamin. Effects of a flexible boundary on hydrodynamic stability. *Journal of Fluid Mechanics*, 9:513–532, 1960.

C. D. Bertram and R. J. Castles. Flow limitation in uniform thick-walled collapsible tubes. *Journal of Fluids and Structures*, 13:399–418, 1999.

C. D. Bertram and N. S. J. Elliott. Flow-rate limitation in a uniform thin-walled collapsible tube, with comparison to a uniform thick-walled tube and a tube of tapering thickness. *Journal of Fluids and Structures*, 17:541–559, 2003.

C. D. Bertram, C. J. Raymond, and T. J. Pedley. Mapping of instabilities for flow through collapsed tubes of differing length. *Journal of Fluids and Structures*, 4:125–153, 1990.

R. L. Bisplinghoff, H. Ashley, and R. L. Halfman. *Aeroelasticity*. Addison-Wesley Publishing Company, 1955. Reprinted by Dover Publications in 1996.

F. J. Bourrières. Sur un phénomène d'oscillation auto-entretenue en mécanique des fluides réels. *Publications Scicntifiques et Techniques du Ministère de l'Air*, 147, 1939.

M. A. Burke and A. D. Lucey. The nonlinear oscillations of a flexible surface comprising one wall of an inviscid channel flow. *3rd Symposium on Fluid-Structure-Sound Interactions and Control. Perth, Western Australia.*, 2015.

M. A. Burke, A. D. Lucey, N. S. J. Elliott, and R. M. Howell. Stability of a flexible wall separating two inviscid channel flows. *American Society of Mechanical Engineers. Pressure Vessels and Piping Conference, Paris, France.*, PVP2013-97373, 2013.

M. A. Burke, A. D. Lucey, R. M. Howell, and N. S. J. Elliott. Stability of a flexible insert in one wall of an inviscid channel flow. *Journal of Fluids and Structures*, 48:435–450, 2014a.

M. A. Burke, A. D. Lucey, R. M. Howell, and N. S. J. Elliott. *Fluid-Structure-Sound Interactions and Control. Proceedings of the 2nd Symposium on Fluid-Structure-Sound Interactions and Control.*, chapter Eigen-Analysis of an Inviscid Channel Flow with a Finite Flexible Plate in One Wall, pages 331–335. Lecture Notes in Mechanical Engineering. Springer, 2014b.

P. W. Carpenter and S. B. Gajjar. *Theoretical Computational Fluid Dynamics*, volume 1, chapter A General Theory for Two- and Three-Dimensional Wall-Mode Instabilities in Boundary Layers over Isotropic and Anisotropic Compliant Walls, pages 349–378. Springer, 1990.

P. W. Carpenter and A. D. Garrad. The hydrodynamic stability of flow over Kramer-type compliant surfaces. Part 1. Tollmien-Schichting instabilities. *Journal of Fluid Mechanics*, 155:465–510, 1985.

P. W. Carpenter and A. D. Garrad. The hydrodynamic stability of flow over Kramer-type compliant surfaces. Part 2. Flow-induced surface instabilities. *Journal of Fluid Mechanics*, 170:199–232, 1986.

P. W. Carpenter, C. Davies, and A. D. Lucey. Hydrodynamics and compliant walls: Does the dolphin have a secret? *Current Science*, 79:758–765, 2000.

W. A. Conrad. Pressure-flow relationships in collapsible tubes. *IEEE Transactions in Bio-medical Engineering*, BME-16:284–295, 1969.

G. Coppola and L. de Luca. On transient growth in linear oscillations. *Physics of Fluids*, 18(078104), 2006.

G. Coppola and L. de Luca. Non-modal dynamics before flow-induced instability in fluid-structure interactions. *Journal of Sound and Vibration*, 329(7):848–865, 2010.

S. Cyr and B. G. Newman. Flow past two-dimensional membrane aerofoils with rear separation. *Journal of Wind Engineering and Industrial Aerodynamics*, 63:1–16, 1996.

C. Davies and P. W. Carpenter. Numerical simulation of the evolution of Tollmien-Schlichting waves over finite compliant panels. *Journal of Fluid Mechanics*, 335:361–392, 1997a.

C. Davies and P. W. Carpenter. Instabilities in a plane channel flow between compliant walls. *Journal of Fluid Mechanics*, 352:205–234, 1997b.

E. de Langre and A. E. Ouvrard. Absolute and convective bending instabilities in fluid-conveying pipes. *Journal of Fluids and Structures*, 13:663–680, 1999.

O. Doaré and E. de Langre. Local and global instability of fluid-conveying pipes on elastic foundations. *Journal of Fluids and Structures*, 16:1–14, 2002.

H. L. Dodds and H. L. Runyan. Effect of high-velocity fluid flow on the bending vibrations and static divergence of a simply supported pipe. *NASA Technical Note*, NASA TN D-2870, 1965.

E. Dowell, J. Edwards, and T. Strganac. Nonlinear aeroelasticity. *Journal of Aircraft*, 40(5):857–874, 2003.

J. Dugundji, E. Dowell, and B. Perkin. Subsonic flutter of panels on continuous elastic foundations - experiment and theory. *American Institute of Aeronautics and Astronautics Journal*, 1 (5):1146–1154, 1963.

U. Ehrenstein and F. Gallaire. On two-dimensional temporal modes in spatially evolving open flows: the flat-plate boundary layer. *Journal of Fluid Mechanics*, 536:209–218, 2005.

R. J. Epstein, R. Srinivasan, and E. H. Dowell. Flutter of an infinitely long panel in a duct. *American Institute of Aeronautics and Astronautics Journal*, 33: 109–115, 1995.

R. O. G. Evetts, R. M. Howell, and A. D. Lucey. A new model for wake effects upon a cantilevered flexible plate undergoing continuous oscillation due to a high Reynolds-number axial flow. *19th Australasian Fluid Mechanics Conference*, 2014.

F. E. Fish. The myth and reality of Gray's paradox: implication of dolphin drag reduction for technology. *Bioinspiration and Biomimetics*, 1:17–25, 2006.

F. E. Fish and C. A. Hui. Dolphin swimming - a review. *Mammal Review*, 21: 181–195, 1991.

M. Gad-el-Hak. Compliant coatings for drag reduction. *Progress in Aerospace Sciences*, 38:77–99, 2002.

M. Gaster. *Turbulence Management and Relaminarisation*, chapter Is the dolphin a red herring?, pages 285–204. International Union of Theoretical and Applied Mechanics. Springer, 1988.

N. D. Gavriely, T. R. Shee, D. W. Cugell, and J. B. Grotberg. Flutter in flow-limited collapsible tubes: a mechanism for generation of wheezes. *Journal of Applied Phsiology*, 66:2251–2261, 1989.

B. Geveci and J. D. A. Walker. Nonlinear resonance of rectangular plates. *Proceedings of the Royal Society of London*, 457:1215–1240, 2001.

J. Gray. Studies in animal locomotion VI. The propulsive powers of the dolphin. *The Journal of Experimental Biology*, 13:192–199, 1936.

J. B. Grotberg and O. E. Jensen. Biofluid mechanics in flexible tubes. *Annual Review of Fluid Mechanics*, 36:121–147, 2004.

J. C. Guneratne and T. J. Pedley. High-Reynolds-number steady flow in a collapsible channel. *Journal of Fluid Mechanics*, 569:151–184, 2006.

C. Q. Guo and M. P. Paidoussis. Stability of rectangular plates with free side-edges in two-dimensional inviscid channel flow. *Journal of Applied Mechanics*, 67:171–176, 2000.

M. Heil and A. L. Hazel. Fluid-structure interaction in internal physiological flows. *Annual Review of Fluid Mechanics*, 43:141–162, 2011.

P. Hémon, E. de Langre, and P. Schmid. Experimental evidence of transient growth of energy before airfoil flutter. *Journal of Fluids and Structures*, 22(3): 391–400, 2006.

E. L. Houghton and P. W. Carpenter. *Aerodynamics for Engineering Students*. Edward Arnold, 4th edition, 1993.

R. M. Howell. *Snoring: A Flow-Structure Interaction*. PhD thesis, University of Warwick, UK, 2006.

R. M. Howell, A. D. Lucey, P. W. Carpenter, and M. W. Pitman. Interaction between a cantilevered-free flexible plate and ideal flow. *Journal of Fluids and Structures*, 25:544–566, 2009.

L. Huang. Flutter of cantilevered plates in axial flow. *Journal of Fluids and Strcutures*, 9:127–147, 1995.

L. Huang. Reversal of the Bernoulli effect and channel flutter. *Journal of Fluids and Structures*, 12:131–151, 1998.

L. Huang. Viscous flutter of a finite elastic membrane in Poiseuille flow. *Journal of Fluids and Structures*, 15:1061–1088, 2001.

P. Huerre and P. A. Monkewitz. Local and global instabilities in spatially developing flows. *Annual Review of Fluid Mechanics*, 22:473–537, 1990.

O. E. Jensen and M. Heil. High-frequency self-excited oscillations in a collapsible-channel flow. *Journal of Fluid Mechanics*, 481:235–268, 2003.

R. B. Johansson. Hydraulic instability of reactor parallel-plate fuel assemblies. *Nuclear Engineering and Science Conference*, 1960.

J. S. Kapor. *Novel computational methods for the study of compliant-wall fluid-structure interaction.* PhD thesis, Curtin University, 2012.

J. J. Knight, A. D. Lucey, and C. T. Shaw. Fluid-structure interaction of a two-dimensional membrane in a flow with a pressure gradient with application to convertible car roofs. *Journal of Wind Engineering and Industrial Aerodynamics*, 98:65–72, 2010.

A. Kornecki, E. H. Dowell, and J. Brien. On the aerooelastic stability of two-dimensional panels in uniform incompressible flow. *Journal of Sound and Vibrations*, 47(2):163–178, 1976.

M. O. Kramer. Boundary layer stabilisation by distributed damping. *Journal of the Aeronautical Sciences*, 24:459–460, 1957.

M. O. Kramer. Boundary layer stabilization by distributed damping. *Journal of American Society of Naval Engineers*, 72:25–33, 1960.

M. O. Kramer. Boundary layer stabilisation by distributed damping. *Journal of American Society of Naval Engineers*, pages 341–348, 1962.

R. B. Kudenatti, N. M. Bujurke, and T. J. Pedley. Stability of two-dimensional collapsible-channel flow at high Reynolds number. *Journal of Fluid Mechanics*, 705:371–386, 2012.

E. Lamballais, J. Silvestrini, and S. Laizet. Direct numerical simulation of flow separation behind a rounded leading edge: Study of curvature effects. *International Journal of Heat and Fluid Flow*, 31(3):295–306, 2010.

M. T. Landahl. On the stability of a laminar incompressible boundary layer over a flexible surface. *Journal of Fluid Mechanics*, 13:609–632, 1962.

A. D. Lucey. *Hydroelastic Instability of Flexible Surfaces*. PhD thesis, University of Exeter, UK, 1989.

A. D. Lucey. The excitation of waves on a flexible panel in a uniform flow. *Philosophical Transactions of the Royal Society of London*, 356:2999–3039, 1998.

A. D. Lucey and P. W. Carpenter. A numerical simulation of the interaction of a compliant wall and inviscid flow. *Journal of Fluid Mechanics*, 234:121–146, 1992.

A. D. Lucey and P. W. Carpenter. The hydroelastic stability of three-dimensional disturbances of a finite compliant wall. *Journal of Sound and Vibration*, 165: 527–552, 1993a.

A. D. Lucey and P. W. Carpenter. On the difference between the hydroelastic instability of infinite and very long compliant panels. *Journal of Sound and Vibration*, 163 (1):176–181, 1993b.

A. D. Lucey and N. Peake. *Flow Past Highly Compliant Boundaries and in Collapsible Tubes*, volume 72 of *Fluid Mechanics and its Applications*, chapter Wave Excitation on Flexible Walls in The Presence of a Fluid Flow, pages 119–145. Springer, 2003.

A. D. Lucey, G. J. Cafolla, P. W. Carpenter, and M. Yang. The nonlinear hydroelastic behaviour of flexible walls. *Journal of Fluids and Structures*, 11:717–744, 1997.

X. Y. Luo and T. J. Pedley. A numerical simulation of unsteady flow in a two-dimensional collapsible channel. *Journal of Fluid Mechanics*, 314:191–225, 1996.

X. Y. Luo and T. J. Pedley. Multiple solutions and flow limitation in collapsible channel flows. *Journal of Fluid Mechanics*, 420:301–324, 2000.

S. Mandre and L. Mahadevan. A generalized theory of viscous and inviscid flutter. *Proceedings of the Royal Society*, 466:141–156, 2010.

D. R. Miller. Critical flow velocities for collapse of reactor parallel-plate fuel assemblies. *ASME Journal of Engineering for Gas Turbines and Power*, 82: 83–95, 1960.

M. P. Païdoussis. *Fluid-Structure Interaction Volume 1.* Elsevier, 1998.

M. P. Païdoussis. *Fluid-Structure Interactions Volume 2.* Elsevier, 2003.

M. P. Païdoussis and N. T. Issid. Dynamic stability of pipes conveying fluid. *Journal of Sound and Vibration*, 33:267–294, 1974.

N. Peake. Nonlinear stability of a fluid-loaded elastic plate with mean flow. *Journal of Fluid Mechanics*, 434:101–118, 2001.

N. Peake. On the unsteady motion of a long fluid-loaded elastic plate with mean flow. *Journal of Fluid Mechanics*, 507:335–366, 2004.

D. Pihler-Puzović and T. J. Pedley. Stability of high-Reynolds-number flow in a collapsible channel. *Journal of Fluid Mechanics*, 714:536–561, 2013.

M. W. Pitman. *An Investigation of Flow Structure Interactions on a Finite compliant Surface Using Computational Methods.* PhD thesis, Curtin University of Technology, WA, 2007.

M. W. Pitman and A. D. Lucey. On the direct determination of the eigenmodes of finite flow-structure system. *Proceedings of the Royal Society*, 465:257–281, 2009.

M. W. Pitman and A. D. Lucey. Spatio-temporal eigenmodes of plane-Poiseuille flow interacting with a finite compliant panel. *6th Australasian Congress on Applied Mechanics, ACAM 6, Dec 12-15 2010. Perth, WA: Engineers Australia*, 2010.

L Prandtl. Remarks on the origin of turbulence. *Zeitschrift für Angewandte Mathematik and Mechanik*, 1:431–436, 1921. [In German].

E. Åkervik, U. Ehrenstein, F. Gallaire, and D. S. Henningson. Global two-dimensional stability measures of the flat plate boundary-layer flow. *European Journal of Mechanics - B/Fluids*, 27:501–513, 2008.

R. R. Reynolds and E. H. Dowell. Nonlinear aeroelastic response of panels. *34th Structures Structural Dynamics and Materials Conference, American Institute of Aeronautics and Astronautics*, pages 2566–2576, 1993.

H Schlichting. Zur enstehung der turbulenz bei der plattenströmung. *Nachrichten von der Gesellschaft der Wissenschaften zu Göttingen, Mathematisch-Physikalische Klasse*, pages 181–208, 1933.

P. J. Schmid and E. de Langre. Transient growth before coupled-mode flutter. *ASME Journal of Applied Mechanics*, 70:894–901, 2003.

P. J. Schmid and D. S. Henningson. *Stability and Transition in Shear Flows*. Springer Science and Business Media New York, 2001.

M. Schwartz, S. Manzoor, P. Hémon, and E. de Langre. By-pass transition to airfoil flutter by transient growth due to gust impulse. *Journal of Fluids and Structures*, 25(8):1272–1281, 2009.

G. D. Smith. *Numerical Solution of Partial Differential Equations: Finite Difference Methods*. Oxford Applied Mathematics & Computing Science Series. Oxford University Press, 3rd edition, 1986.

H. Sturm, G. Dumstorff, P. Busche, D. Westermann, and W. Lang. Boundary layer separation and reattachment detection on airfoils by thermal flow sensors. *Sensors*, 12(11):14292–14306, 2012.

B. H. Tan, A. D. Lucey, and M. W. Pitman. Hydroelastic stability of flexible a panel: Eigen-analysis and time-domain response. *Proceedings of ASME 2010 3rd Joint US-European Fluids Engineering Summer Meeting and 8th International Conference on Nanochannels, Microchannels, and Minichannels*, 2010.

B. H. Tan, A. D. Lucey, and R. M. Howell. Aero-/hydro-elastic stability of flexible panels: Prediction and control using localised spring support. *Journal of Sound and Vibration*, 322:7033–7054, 2013.

W Tollmien. Über die entsehung der turbulenz. 1. Mitteilung. *Nachrichten von der Gesellschaft der Wissenschaften zu Göttingen, Mathematisch-Physikalische Klasse*, pages 21–44, 1929.

L. N. Trefethen and M. Embree. *Spectra and Pseudospectra: The behaviour of Nonnormal Matrices and Operators*. Princeton University Press, 2005.

K. Tsigklifis and A. D. Lucey. Modelling and analysis of the global stability of Blasius boundary-layer flow interacting with a compliant wall. *20th International Congress on Modelling and Simulation, Adelaide, Australia*, pages 775–781, 2013.

K. Tsigklifis and A. D. Lucey. Global stability of three-dimensional disturbances in blasius boundary-layer flow over a compliant panel. *19th Australian Fluid Mechanics Conference, Melbourne, Australia*, 2014.

M. R. Visbal and R. E. Gordinier. Numerical simulation of the interaction of a transitional boundary layer with a 2-d flexible panel in the subsonic regime. *Journal of Fluids and Structures*, 19:881–903, 2004.

D. S. Weaver and B. Myklatun. On the stability of thin pipes with an internal flow. *Journal of Sound and Vibration*, 31:399–410, 1973.

D. S. Weaver and M. P. Païdoussis. On collapse and flutter phenomena in thin tubes conveying fluid. *Journal of Sound and Vibration*, 50:117–132, 1977.

D. S. Weaver and T. E. Unny. The hydroelastic stability of a flat plate. *ASME: Journal of Applied Mechanics*, 37:823–827, 1970.

D. S. Weaver and T. E. Unny. On the dynamic stability of fluid conveying pipes. *Journal of Applied Mechanics*, 40:48–52, 1973.

O. Wiplier and U. Ehrenstein. Numerical simulation of linear and nonlinear disturbance evolution in a boundary layer with complaint walls. *Journal of Fluids and Structures*, 14:157–182, 2000.

O. Wiplier and U. Ehrenstein. On the absolute instability in a boundary-layer flow with complaint coatings. *European Journal of Mechanics B/Fluids*, 20: 127–144, 2001.

Nomenclature

α	Angle of panels with horizontal
$\ddot{\eta}$	Insert vertical acceleration
Δp	Unsteady pressure perturbation
δt	Size of time step
$\dot{\eta}$	Insert vertical velocity
$\eta\left(x,t\right)$	Insert vertical displacement
η_0	Amplitude of initial perturbation
$\eta_{\max}$	Peak amplitude of maximum displacement of insert
η_{mean}	Peak amplitude of mean displacement of insert
κ	Coupling variable
Λ^{F}	Non-dimensional stiffness ratio (flow speed)
$\Lambda^{\mathrm{F}}_{DO}$	Divergence onset for the open flow
Λ^{I}	Non-dimensional flow velocity for a spring-backed wall
Λ^{M}	Non-dimensional stiffness ratio (flow speed) for tensioned membranes
λ_{s}	Critical wavelength
λ'_{s}	Non-dimensional critical wavelength
$[B]$	Nonlinear acceleration matrix
$[D^{+}]$	Spatially averaging matrix

$[D_n]$ n^{th} order differentiation matrix

$\left[I^{\Phi}\right]$ Perturbation influence coefficient matrix

$\left[I^{N}\right]$ Normal influence coefficient matrix

$\left[I^{T}\right]$ Tangential influence coefficient matrix

$[\Lambda]$ Diagonal matrix of eigenvalues

$[A]$ State space formulation acceleration matrix

$[E]$ State-space formulation velocity matrix

$[F]$ State-space formulation displacement matrix

$[H]$ State-space formulation matrix

$[I]$ Identity matrix

$[M]$ Grammian matrix

μ Non-dimensional mass ratio

ν Poisson's ratio

ϕ Velocity perturbation

ρ_{f} Fluid density

ρ_{m} Insert density

σ Source strengths

ζ Theoretical function to account for channel height, H

$\{F\}$ Nonlinear displacement and velocity vector

$\{X\,(x, y, t,)\}$ Transient growth disturbance

$_n$ Denoting the upper and lower channel for $n = 1, 2$ respectively

a Nonlinear approximation

B Flexural rigidity

c	Complex wave speed
d	Insert structural damping
E	Elastic modulus
$E(t)$	Energy Norm
$G(t)$	Energy growth function
H	Channel height
h	Insert thickness
H'	Non-dimensional channel height
K	Spring stiffness
k	Wavenumber
K'	Non-dimensional spring stiffness
k_{d}	Critical wavenumber for divergence-onset
k_{m}	Critical wavenumber for modal-coalescence onset
L	Length of flexible insert
L'	Non-dimensional insert length
L_{r}	Length of rigid wall up- and down-stream of insert
N	Total number of panels
n	Mode number
N_{f}	Number of panels comprising insert
p_{H}	Hydrodynamic stiffness
S'	Non-dimensional frequency (flow speed)
S_0	Theoretical angular frequency
S_{I}	Oscillation frequency

S_{R}	Growth/decay rate
T	Uniform tension
T_{I}	Induced tension
U	Applied flow velocity
U'	Non-dimensional flow velocity
U_{d}	Critical flow speed for divergence-onset
U_{m}	Critical flow speed for modal-coalescence onset
u_N	Disturbance normal velocity
u_T	Disturbance tangential velocity
u_x	Velocity Perturbation, x direction
u_y	Velocity Perturbation, y direction